University of Alberta

An experimental study on a minette and its associated mica-clinopyroxenite xenolith from the Milk River area, southern Alberta, Canada

by

Sean Philip Funk

A thesis submitted to the Faculty of Graduate Studies and Research
in partial fulfillment of the requirements for the degree of

Master of Science

Earth and Atmospheric Sciences

Fall 2012
Edmonton, Alberta

To my parents, Paul and Doris

Abstract

Buhlmann et al. (2000) studied the minettes and xenoliths from southern Alberta, Canada. They hypothesized that the minettes were derived from a source containing phlogopite + clinopyroxene at pressures ≥ 1.7 GPa. To test this hypothesis, we investigated 1) the liquidus mineralogy of a primitive minette; and 2) the melting reactions of a mica + clinopyroxene assemblage. For the minette, we found a multiple saturation point at 1.77 GPa and 1350°C, where liquid coexists with orthopyroxene and olivine. Neither phlogopite nor clinopyroxene were found to be liquidus phases. We suggest that our minette is not primary, but had re-equilibrated with harzburgitic mantle subsequent to formation. For our mica-clinopyroxenite assemblage, we found the solidus is at temperatures above a cratonic geotherm, implying that this mica-clinopyroxenite is stable in a craton. The composition of the melts from our experiments are similar to madupitic lamproites from Leucite Hills, Wyoming, studied by Carmichael (1967).

Acknowledgements

I would like to thank Dr. Robert Luth, my supervisor, for his guidance, insight and the funding he provided my through his Natural Sciences and Engineering Research Council of Canada (NSERC) Discovery Grant. It is through this experience that I have grown to understand the requirements demanded on those who pursue a career in academia. Without Bob, I would not have been given this valuable experience that I will carry throughout my life. Much appreciation and gratitude to my fellow graduate students, Danny Hnatyshin, Andreas Enggist, and Jason Hong, for listening to my endless discussions (and sometimes rants) about my experimental results. Some of those discussions actually ended up being useful. I would also like to acknowledge Sergei Matveev for his valuable and extensive aid during my microprobe analyses. His expertise and guidance made this research possible. To Dr. Thomas Chacko, I thank him for his overall support and guidance over the years, as well as his aid on the microprobe during the last months of my thesis. I would also like to thank Dr. Claire Currie for her help in some of the more geophysical side of this research.

I am grateful for the additional financial support was provided through the NSERC Postgraduate Scholarship granted to me, the numerous Teaching and Research Assistantships I held at the University of Alberta (UofA), the Walter H. Johns Graduate Fellowship (UofA), and the Alberta Advanced Education and Technology Graduate Student Scholarship (Provincial). I am especially appreciative of the Hibb's Student Conference Travel Award (through the Institute for Geophysical Research at the UofA), The Profiling Alberta's Graduate Students Award (through the Faculty of Graduate and Research Studies), and the Graduate Student Association Professional Development Grant for allowing me to travel to Prague, Czech Republic and present my research at the 2011 Goldschmidt conference.

I would like to thank my family for their support over the course of my academic career. A special thanks goes to my best friend and beloved girlfriend, Christine Card, who kept me going and sane during the most stressful times of this research. When things seemed at their darkest, she was my light to keep me going. To my friends, Rob Renz, Benjamin Packianayagam, Branawan Gowrishankar, Vithuran Gowrishankar, Chrse Tham, Charlene Ahorro, Karson Styles, Clair Tolton, Mark Cheung, Jerry Lo, Justine Brilliant, Liz Martin, and Omar Manji, your support was invaluable. Although my scholarly pursuits demanded much of my free time, what little time we did get together was much needed and appreciated.

Table of Contents:

List of Tables

List of Figures

List of Symbols and Abbreviations

Al_2O_3	Alumina (aluminum oxide)
Al	Aluminum
ap	Apatite
~	Approximately
→ or ↔	Arrow (means "goes into")
Ba	Barium
<d.l.	Below detection limits
B	Boron
Ca	Calcium
CaO	Calcium oxide
CO_2	Carbon dioxide
C-O-H	Carbon-Oxygen-Hydrogen fluid
Cs	Cesium
Cl	Chlorine
Cr	Chromium
Cr_2O_3	Chromium (III) oxide
ca.	Circa (approximately)
cpx	Clinopyroxene
Co	Cobalt
nA μm^{-2}	Current Density (nanoamperes per square micrometers)
°C	Degrees Celsius
°C/min	Degrees Celsius per minute
emf	Electromotive force (V)
ε_{Nd}	Epsilon Neodymium

Eu	Europium
$K_D(Fe\text{-}Mg)^{min\text{-}liq}$	Exchange Coefficient for Fe-Mg between mineral and liquid
F	Fluorine
GPa	Gigapascal
>	Greater than
≥	Greater than or equal to
Hf	Hafnium
hrs	Hours
HFSE	High Field Strength Elements
ID	Inner Diameter
Fe	Iron
Fe^{2+}	Iron (ferrous)
FeO*	Iron (total) normalized to Fe^{2+} (ferrous)
JDF	Juan de Fuca plate
km	Kilometer
kV	Kilovolts
KC	Kimberlite Corridor
LILE	Large Ion Lithophile Elements
<	Less than
≤	Less than or equal to
LREE	Light Rare Earth Elements
liq	Liquid (melt)
LOI	Loss On Ignition
Lu	Lutetium
Mg	Magnesium

Mg#	Magnesium number
MgO	Magnesia (magnesium oxide)
Mn	Manganese
MnO	Manganese oxide
ms.	Manuscript
MARID	Mica-amphibole-rutile-ilmenite-diopside
µm	Micrometers
mg	Milligrams
mm	Millimeters
Ma	Million years
mW m^{-2}	Milliwatts per square meter
min	Mineral (or "minutes" depending on context)
-	Minus (or "to" depending on context)
X_i	Modal abundance of phase i
X_{oxide}^{phase}	Molar Fraction of oxide in phase
nA	Nanoamperes
Nd	Neodymium
Ni	Nickel
Nb	Niobium
n	Number of analyses
ol	Olivine
opx	Orthopyroxene
Os	Osmium
OD	Outer Diameter
O	Oxygen

$D_{oxide}^{min/melt}$	Partitioning coefficient between mineral and melt for oxide
ppm	Parts per million
%	Percent
K	Potassium
K_2O	Potassium oxide
PRZ	Phi Rho Zed correction
phl	Phlogopite
P	Phosphorous
P_2O_5	Phosphorous pentaoxide
Pt	Platinum
+	Plus (or "and" depending on context)
±	Plus or minus ("with or without" or "error" depending on context)
PT-space	Pressure-Temperature space
REE	Rare Earth Elements
Re	Rhenium
Rb	Rubidium
Sm	Samarium
Sc	Scandium
sec	Seconds
SiO_2	Silica (silicon dioxide)
Si	Silicon
Na	Sodium
Na_2O	Sodium oxide
σ	Standard Deviation
Sr	Strontium

$\sum$	Sum (addition of terms)
$\sum R^2$	Sum of residual squares
Th	Thorium
TiO_2	Titania (titanium (IV) oxide)
Ti	Titanium
W	Tungsten
□	Vacancy
var.	Variable composition
H_2O	Water
H_2O^+	Water added to system
wt%	Weight Percent
KCMAS-H_2O	6 component system containing K_2O-CaO-MgO-Al_2O_3-SiO_2-H_2O

Chapter 1. Introduction:

1.1. Overview:

Lamprophyres, a term first coined by von Gumbel (1874) from the Greek roots *lampros* and *porphyros* (which means "glistening porphyry"), are a heterogeneous group of igneous rocks that are volumetrically small, exotic and rare. Since then, the study of these rocks has produced a plethora of uninformative names (see Rock 1991 for a detailed review). There have been some attempts to rein in the nomenclature (Dawson 1987; Rock 1987, 1991; Foley et al. 1987; Mitchell and Bergman 1991; Mitchell 1994b; Woolley et al. 1996), but they have been generally unsuccessful. These rocks have been the subject of many academic studies, both geochemical (Lloyd and Bailey 1975; Van Kooten 1980; Macdonald et al. 1992; Conticelli and Peccerillo 1992; Carlson and Nowell 2001; Orejana et al. 2008; Rosenthal et al. 2009) and experimental (Edgar et al. 1976, 1980; Edgar and Condliffe 1978; Barton and Hamilton 1978, 1979; Lloyd et al. 1985; Esperanca and Holloway 1987; Righter and Carmichael 1996; Elkins-Tanton and Grove 2003; Parat et al. 2010). Lamprophyres, and other related mafic alkali-rich rocks, have paradoxical compositions, enriched in both compatible (e.g. MgO) and incompatible elements (e.g. Cr, Ni, Co, Sc, large ion lithophile elements (LILE)) but depleted in high field strength elements (HFSE). They are not easily explained by partial melting of a typical refractory mantle peridotitic source. The high Mg# (65-80%), Sc (15-30 ppm), Cr (200-500 ppm), Ni (90-700 ppm) and Co (25-80 ppm) content are consistent with lamprophyres being primary magmas derived from the mantle (Frey et al. 1978; Rhodes 1981), but the mineralogy of their source region is largely unknown. In an attempt to better define the term, Rock (1977) classifies a lamprophyre as: "an alkali-rich porphyritic dyke-rock (more rarely a plug or lava) showing intermediate to very low SiO_2 content with moderate to high colour index, carrying essential

primary amphibole and/or mica, and typified by lack of felsic phenocrysts and groundmass olivine, by characteristic alteration and by panidiomorphic texture."

In North America, a large number of alkaline rocks, including lamprophyres, lamproites and kimberlites, are restricted to continental interiors, usually within Archean cratons. Some of these rocks are located in the "kimberlite corridor" (KC) (**Figure 1.1**), as defined by Heaman et al. (2003; 2004) and Currie and Beaumont (2011), which is a stretch of land located on the western portion of North America (~1000-1500 km inland). Its northern most extent is located in the Slave craton, Northwest Territories, Canada and it extends down south to include the Wyoming craton and the Colorado Plateau, United States. The main emplacement phase of alkali magmatism in western North America began ca. 110 Ma and lasted to ca. 45 Ma, with a few occurring as late as ca. 25 Ma. The locations of these alkaline rocks in North America do not match with known mantle plume tracks (Heaman et al. 2003), and are located outside regions of known mantle upwellings (Torsvik et al. 2010). Many authors have studied the Montana and Wyoming high-potassium magmas (Fraser et al. 1985; Dudas et al. 1987; Eggler et al. 1987; Meen and Eggler 1987; Mitchell et al. 1987; Hyndman et al. 1988; Scambos and Farmer 1988; Irving 1990; Dudas 1991; O'Brien et al. 1991, 1995; Macdonald et al. 1992; Buhlmann et al. 2000; Carlson and Nowell 2001; Downes et al. 2004; Facer et al. 2009; Smith 2010) and have suggested that the subduction and dehydration of the Farallon plate during the late Cretaceous was the trigger for alkali magmatism. Macdonald et al. (1992), Buhlmann et al. (2000) and Carlson and Nowell (2001) argue that the North American potassic magmas were derived from partial melting of a veined source containing mica and pyroxene at depths approaching the base of the craton. Numerical models (e.g. Currie and Beaumont 2011) have since shown these hypotheses to be plausible.

Dawson (1884), Weed and Pirsson (1895), Kemp and Billingsley (1921), Williams and Dyre (1930) and Russell and Landes (1940) were among the first to study the alkaline rocks from southern Alberta, and classified them as minettes. We have retained their terminology in this study. The minettes in southern Alberta are the northern outliers of the Eocene-aged Sweet Grass Hills igneous complex. Carried in the minettes are coarse-grained xenoliths composed of phlogopite, clinopyroxene and apatite. Kjarsgaard (1994) conducted an extensive study, including whole-rock major- and trace-element analyses, mineralogy and mineral analyses, on these minettes. Kjarsgaard (1994) noted that the southern Alberta minettes are compositionally similar to other alkaline rocks from Montana, United States.

Much of the foundation for this investigation was based on Buhlmann (1996; MSc thesis) and Buhlmann et al. (2000), who studied both the minettes and the mica-clinopyroxenite xenoliths from the Milk River area, southern Alberta, Canada. The minettes are hydrous, potassic and Mg-rich and, according to these authors, are likely derived from the lithospheric mantle. The most primitive minettes usually have porphyritic textures, with olivine pseudomorphs, phlogopite, and diopside as phenocrysts, and a matrix consisting of clinopyroxene, sanidine, mica, spinel, apatite and sometimes carbonates and analcime. They are light rare earth element (LREE)-enriched with no Eu anomaly, and have strong negative Th and Nb anomalies (Buhlmann et al. 2000). Buhlmann et al. argued that the trace-element and isotopic characteristics of the minettes requires at least three components in the source region: 1) a LREE-enriched, HFSE-depleted, low ε_{Nd} source, likely ancient lithospheric mantle (O'Brien et al. 1991, 1995); 2) an asthenospheric mantle source with near bulk-Earth Sr and Nd isotopic values; and 3) a source with high $^{87}Sr/^{86}Sr$, Rb-Sr, and Sm-Nd (sometimes enriched in Ba and

depleted in Nb and Ti), inferred to be a young component (possibly a subduction-related component).

Based on the work of Esperanca and Holloway (1987) and extrapolating phase boundaries inferred by Wallace and Carmichael (1989), Buhlmann et al. (2000) suggested that the parental melt of the Milk River minettes could have come from a source containing phlogopite + clinopyroxene ± olivine at pressures ≥ 1.7 GPa. The high concentrations of TiO_2 (~1.0 wt%), K_2O (>4.44 wt%), Rb (~200 ppm), Cs (~3 ppm), and Nb (~13 ppm) in the minettes are consistent with the melting of phlogopite (Ionov et al. 1997; Pearson et al. 2004). The high CaO (>5.96 wt%) content and enrichments in the rare earth elements (REE) (Menzies 1983) are best explained with clinopyroxene in the source. The concentration of P_2O_5 (~1.0 wt%) indicate that apatite is likely a component of the source as well. The high Sr (~900-2000 ppm) content could be due to either clinopyroxene or apatite in the source, whereas the high Ba (~1500-4000 ppm) concentrations are consistent with phlogopite or apatite in the source (Ionov et al. 1997; Pearson et al. 2004). This source region mineralogy of phlogopite + clinopyroxene + apatite agrees with many previous studies, both experimental (Edgar et al. 1976, 1980; Barton and Hamilton 1978, 1979; Edgar and Condliffe 1978; Nicholls and Whitford 1983; Lloyd et al. 1985; Esperanca and Holloway 1987; Mitchell 1995; Righter and Carmichael 1996; Sato 1997; Elkins-Tanton and Grove 2003) and geochemical (Lloyd and Bailey 1975; Van Kooten 1980; Wallace and Carmichael 1989; Conticelli and Peccerillo 1992; Foley 1992a, 1992b; Macdonald et al. 1992; Carlson and Nowell 2001), on related mafic alkali-rich rocks.

In the cratonic mantle, it is generally accepted that phlogopite-rich clinopyroxenite lithologies are volumetrically small, and one popular model is that these lithologies are present as veins. Foley (1992b) investigated the partial melting behaviour of veined peridotite, and

concluded that the initial melting is dominated by the vein because it is volatile-rich, and therefore has a lower solidus temperature relative to its surroundings. The melts derived from the vein, which are in disequilibrium with the surrounding wall-rock, would infiltrate into the peridotite wall-rock and dissolve some of the minerals. Foley et al. (1999) investigated the melting behaviour on several amphibole + phlogopite + clinopyroxene ± accessory minerals vein assemblages at 1.5 and 5.0 GPa. They found that relative to a mica-clinopyroxenite, the addition of amphibole lowered the solidus by ~50°C, and that amphibole was the main factor controlling the composition of the melt. Foley et al. also found that the solidi for the hydrous vein assemblages had a steeper P-T slope relative to a cratonic mantle geotherm, and concluded that at greater depths, minimal heating would be required to induce partial melting. Pilet et al. (2008) conducted sandwich experiments on a hornblendite to study the melting behaviour of the vein assemblage and reactions between the alkali-rich, silica-undersaturated partial melts and the surrounding peridotite. Pilet et al.'s observations are consistent with the dissolution model proposed by Foley (1992b).

A number of workers have invoked a vein-plus-wall-rock melting model to explain magmas in various locales (e.g. Italy: Conticelli et al. 2009; Boari et al. 2009; Nikogosian and van Bergen 2010; Tibet: Jiang et al. 2006). One example that illustrates wall-rock reactions is from Maria and Luhr (2008), who studied the alkaline and mafic rocks from the Western Mexican Volcanic belt. They argued that the lamprophyres found in the region were the result of partial melting of a phlogopite-rich vein assemblage, and that the lamprophyres evolved into basanites, and later basalts, with increasing wall-rock dissolution. Other workers (e.g. Carlson and Irving 1994; Mitchell 1995) have also proposed that the alkaline magmas from the Wyoming

craton were produced by the model proposed by Foley (1992b). Such a model may be applicable to the petrogenesis of the Milk River minettes.

1.2. Goals of the study:

The study of alkali-rich mafic magmas provides a unique insight into the chemical and lithological heterogeneities in the mantle. It is generally accepted that many alkaline magmas are derived from unusual vein lithologies, usually containing large quantities of amphibole and/or mica, and therefore they can be used to constrain the distribution and cycling of alkalis, incompatible elements and hydrous fluids in the mantle. Some of these alkaline rocks, kimberlites and lamproites in particular, are carriers of important economic resources such as diamonds. It was suggested by Wyman and Kerrich (1988) and Rock and Groves (1988) that lamprophyres as well may be a source of gold, silver and diamonds (if their source region is >150 km).

The goal of our study is to 1) determine the conditions (temperature and pressure) at which the minettes formed; and 2) ascertain the mineralogy of the residue in the source region. We conducted two separate sets of experiments to do so. The first series of experiments was to characterize the liquidus mineralogy of the minette. Liquidus experiments are challenging because they must fulfil two criteria: 1) the melt must be in equilibrium with the residue of the source region; and 2) during the melt's ascent, it must remain compositionally unmodified. If this is the case, the multiple saturation point, a single point in PT-space where multiple minerals crystallize at the liquidus, sheds light on two pieces of information: 1) the pressure and temperature of formation; and 2) the mineralogy and composition of the residue.

The second series of experiments involved melting a representative mica-clinopyroxenite lithology and characterizing the melts produced. With these experiments, we are simulating the physical processes that occur in the mantle during melt formation. In these experiments, the location of the solidus in PT-space is of interest. The solidus tells us at what temperatures and pressures this lithology begins to melt. With increasing temperature, we can infer the melting reactions that take place above the solidus.

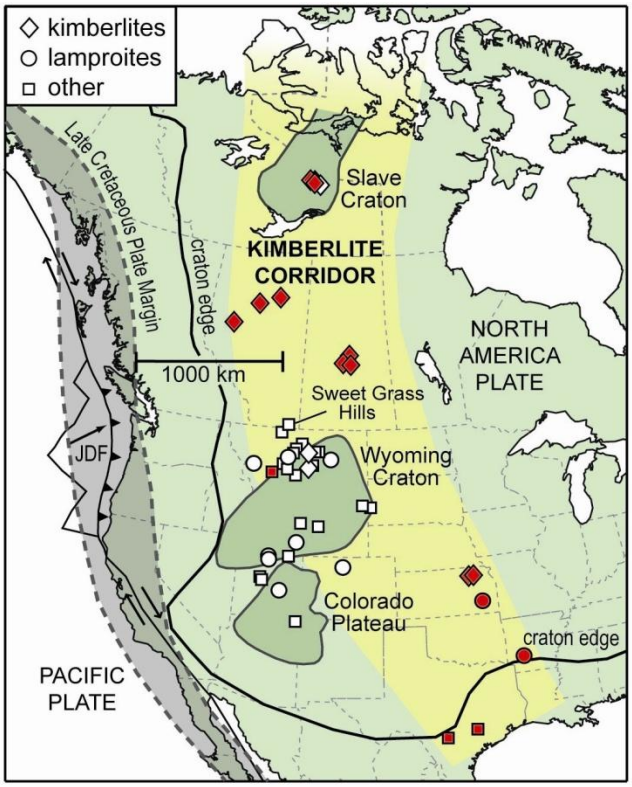

Figure 1.1: The distribution of mafic alkali-rich rocks in North America within the "kimberlite corridor" (modified from Currie and Beaumont 2011). The modern Juan de Fuca plate is shown off the west coast of North America, and is the last remnant of the Farallon plate. Along the Alberta-Montana boundary, the Sweet Grass Hills minettes (Milk River area) is labelled. Symbols: red = Cretaceous emplacement ages; white = Cenozoic ages.

References:

Barton M, Hamilton DL (1978) Water-saturated melting relationships to 5 kbars of three Leucite Hills lavas. Contrib Mineral Petrol **66:** 41 - 49

Barton M, Hamilton DL (1979) The melting relationships of a madupite from the Leucite Hills, Wyoming, to 30 Kb. Contrib Mineral Petrol **69:** 133 - 142

Boari E, Tommasini S, Laurenzi MA, Conticelli S (2009) Transition from ultrapotassic kamafugitic to sub-alkaline magmas: Sr, Nd and Pb isotope, trace element and 40Ar/39Ar age data from the Middle latin Valley volcanic field, Roman Magmatic Province, Central Italy. J Petrol **50:** 1327 - 1357

Buhlmann AL (1996) Eocene Minettes and their Mica-clinopyroxenite inclusions in the Milk River area, southern Alberta: Nature and Origin. University of Alberta, MSc Thesis

Buhlmann AL, Cavell P, Burwash RA, Creaser RA, Luth RW (2000) Minette bodies and cognate mica-clinopyroxenite xenoliths from the Milk River area, southern Alberta: records of a complex history of the northernmost part of the Archean Wyoming craton. Can J Earth Sci **37:** 1629 - 1650

Carlson RW, Irving AJ (1994) Depletion and enrichment history of subcontinental lithospheric mantle: An Os, Sr, Nd and Pb isotopic study of ultramafic xenoliths from the northwestern Wyoming Craton. Earth Planet Sci Lett **126:** 457 - 472

Carlson RW, Nowell GM (2001) Olivine-poor sources for mantle-derived magmas: Os and Hf isotopic evidence from potassic magmas of the Colorado Plateau. Geochem Geophys Geosyst **2:** 2000GC000128

Conticelli S, Marchionni S, Rosa D, Giordano G, Boari E, Avanzinelli R (2009) Shoshonite and sub-alkaline magmas from an ultrapotassic volcano: Sr-Nd-Pb isotope data on the Roccamonfina volcanic rocks, Roman Magmatic Province, Southern Italy. Contrib Mineral Petrol **157:** 41 - 63

Conticelli S, Peccerillo A (1992) Petrology and geochemistry of potassic and ultrapotassic volcanism in central Italy: Petrogenesis and inferences on the evolution of mantle sources. Lithos, **28:** 221 - 240

Currie CA, Beaumont C (2011) Are diamond-bearing Cretaceous kimberlites related to low-angle subduction beneath western North America? Earth Planet Sci Let **303:** 59 – 70

Dawson GM (1884) 1882-83-84, Part C Report of Progress. Geological Survey of Canada, pp 16-17 and 45-47

Dawson JB (1987) The kimberlite clan: Relationship with olivine and leucite lamproites, and inferences for upper mantle metasomatism. In JG Fitton and BGJ Upton (eds), Alkaline Igneous Rocks. Blackwell Scientific. Oxford: pp 95 - 102

Downes H, MacDonald R, Upton BGJ, Cox KG, Bodinier J-L, Mason PRD, James D, Hill PG, Hearn, Jr BC (2004) Ultramafic xenoliths from the Bearpaw Mountains, Montana, USA: Evidence formultiple metasomatic events in the lithospheric mantle beneath the Wyoming craton. J Petrol **45:** 1631 - 1662

Dudas FO (1991) Geochemistry of igneous rocks of the Crazy Mountains, Montana, and tectonic models for the Montana alkalic province. J Geophys Res **96:** 13261 - 13277

Dudas FO, Carlson RW, Eggler DH (1987) Regional Middle Proterozoic enrichment of the subcontinental mantle source of igneous rocks from central Montana. Geology, **15:** 22 - 25

Edgar AD, Condliffe E (1978) Derivation of K-rich ultramafic magmas from a peridotitic mantle source. Nature, **275:** 639 - 640

Edgar AD, Condliffe E, Barnett RL, Shirran GJ (1980) An experimental study of an olivine ugandite magma and mechanisms for the formation of its K-enriched derivatives. J Petrol **21:** 475 - 497

Edgar AD, Green DH, Hibberson WO (1976) Experimental petrology of a highly potassic magma. J Petrol **17:** 339 - 356

Eggler DH, McCallum ME, Kirkley MB (1987) Kimberlite-transported nodules from Colorado-Wyoming; a record of enrichment of shallow portions of an infertile lithosphere. Geological Society of America, Special Papers, **215:** 77 - 90

Elkins-Tanton LT, Grove TL (2003) Evidence for deep melting of hydrous metasomatized mantle: Pliocene high-potassium magmas from the Sierra Nevadas. J Geophys Res **108:** 1 - 19

Esperanca S, Holloway JR (1987) On the origin of some mica-lamprophyres: experimental evidence from a mafic minette. Contrib Mineral Petrol **95:** 207 - 216

Facer J, Downes H, Beard A (2009) *In situ* serpentinization and hydrous fluid metasomatism in spinel dunite xenoliths from the Bearpaw Mountains, Montana, USA. J Petrol **50:** 1443 - 1475

Foley SF (1992a) Petrological characterization of the source components of potassic magmas: Geochemical and experimental constraints. Lithos, **28:** 187 - 204

Foley SF (1992b) Vein-plus-wall-rock melting mechanisms in the lithosphere and the origin of potassic alkaline magmas. Lithos, **28:** 435 - 453

Foley SF, Musselwhite DS, Van Der Laan SR (1999) Melt compositions from ultramafic vein assemblages in the lithospheric mantle: a comparison of cratonic and non-cratonic settings. In: The JB Dawson volume, Proceedings of the VIIth International Kimberlite Conference **1:** 238 - 246

Foley SF, Venturelli G, Green DH, Toscani L (1987) The ultrapotassic rocks: Characteristics, classification, and constraints for petrogenetic models. Earth Sci Rev **24:** 81 - 134

Fraser KJ, Hawkenworth CJ, Erlank AJ, Mitchell RH, Scott-Smith BH (1985) Sr, Nd, and Pb isotope and minor-element geochemistry of lamproites and kimberlites. Earth Planet Sci Lett **76:** 57 - 70

Frey FA, Green DH, Roy SD (1978) Integrated models of basalt petrogenesis: a study of quartz tholeiites to olivine melilitites from south eastern Australia utilizing geochemical and experimental petrological data. J Petrol **19:** 463 - 513

Heaman LM, Kjarsgaard BA, Creaser RA (2003) The timing of kimberlite magmatism in North America: implications for global kimberlite genesis and diamond exploration. Lithos **71:** 153 – 184

Heaman LM, Kjarsgaard BA, Creaser RA (2004) The temporal evolution of North American kimberlites. Lithos **76:** 377 - 397

Hyndman DW, Tureck-Schwartz K, Foland KA (1988) Chemical and isotopic evidence for potassic mafic magmas from an old K-enriched mantle source and for Eocene crustal melting in the central Montana alkalic province. Geological Society of America, Abstracts with Programs, **20:** A195

Ionov DA, Griffin WL, O'Reilly SY (1997) Volatile-bearing minerals and lithophile trace elements in the upper mantle. Chem Geol **141:** 153 - 184

Irving AJ (1990) Montana Archean lithospheric mantle: chemical constraints from Eu-anomalous ultramafic xenoliths in minette. EOS Transactions, American Geophysical Union, **71:** 1712

Jiang YH, Jiang SY, Ling HF, Dai BZ (2006) Low-degree melting of a metasomatized lithospheric mantle for the origin of Cenozoic Yulong monzogranite-porphyry, east Tibet: Geochemical and Sr-Nd-Pb-Hf isotopic constraints. Earth Planet Sci Lett **241:** 617 - 633

Kemp JF, Billingsley P (1921) Sweet Grass Hills, Montana. Geological Society of America Bulletin, **32:** 437 - 478

Kjarsgaard BA (1994) Potassic magmatism in the Milk River area, southern Alberta: petrology and economic potential. Current Research 1994-B, Geological Survey of Canada: 59 – 68

Lloyd FE, Arima M, Edgar AD (1985) Partial melting of a phlogopite-clinopyroxenite nodule from south-west Uganda: an experimental study bearing on the origin of highly potassic continental rift volcanics. Contrib Mineral Petrol **91:** 321 - 329

Lloyd FE, Bailey DK (1975) Light element metasomatism of the continental mantle: evidence and the consequences. Phys Chem Earth **9:** 389 - 415

Macdonald R, Upton BGJ, Collerson KD, Hearn Jr BC, James D (1992) Potassic mafic lavas of the Bearpaw Mountains, Montana: mineralogy, chemistry, and origin. J Petrol **33:** 305 - 346

Maria AH, Luhr JF (2008) Lamprophyres, basanites, and basalts of the Western Mexican Volcanic belt: Volatile contents and a vein-wallrock melting relationship. J Petrol **49:** 2123 - 2156

Meen JK, Eggler DH (1987) Petrology and geochemistry of the Cretaceous Independence volcanic suite, Absoroka Mountains, Montana: clues to the composition of the Archean sub-Montana mantle. Geological Society of America Bulletin, **98:** 238 - 247

Menzies MA (1983) Mantle ultramafic xenoliths in alkaline magmas: evidence for mantle heterogeneity modified by magmatic activity. In: CJ Hawkesworth and MJ Norry (eds) Continental Basalts and Mantle Xenoliths. Shiva, Mantwich, pp. 92 - 110

Mitchell RH (1994b) Suggestions for revisions to the terminology of kimberlites and lamprophyres from a genetic viewpoint. In HOA Meyer and OH Leonardos (eds), Kimberlites, Related Rocks and Mantle Xenoliths. Proceedings of the Fifth International Kimberlite Conference V. I. CPRM. Rio de Janeiro: pp 15 - 26

Mitchell RH (1995) Melting experiments on a sanidine phlogopite lamproite at 4 - 7 GPa and their bearing on the sources of lamproite magma. J Petrol **36:** 1455 - 1474

Mitchell RH, Bergman SC (1991) Petrology of Lamproites. Plenum. New York

Mitchell RH, Platt RG, Downey M (1987) Petrology of lamproites from Smoky Butte, Montana. J Petrol **28:** 645 - 677

Nicholls IA, Whitford DJ (1983) Potassium-rich volcanic rocks of the Muriah complex, Java, Indonesia: Products of multiple magma sources? J Volcanol Geotherm Res **18:** 337 - 359

Nikogosian IK, van Bergen MJ (2010) Heterogeneous mantle sources of potassium-rich magmas in central-southern Italy: Melt inclusion evidence from Roccamonfina and Ernici (Mid Latina Valley). J Volcano Geothermal Res **197:** 279 - 302

O'Brien HE, Irving AJ, McCallum IS (1991) Eocene potassic magmatism in the Highwood Mountains, Montana: petrology, geochemistry and tectonic implications. J Geophys Res **96:** 13237 - 13260

O'Brien HE, Irving AJ, McCallum IS, Thirlwall MF (1995) Strontium, neodymium, and lead isotopic evidence for the interaction of post-subduction asthenospheric potassic mafic magmas of the Highwood Mountains,

Montana, USA, with ancient Wyoming craton lithospheric mantle. Geochim Cosmochim Acta **59:** 4539 - 4556

Orejana D, Villaseca C, Billstrom K, Paterson BA (2008) Petrogenesis of Permian alkaline lamprophyres and diabases from the Spanish Central System and their geodynamic context within western Europe. Contrib Mineral Petrol **156:** 477 - 500

Parat F, Holtz F, Rene M, Almeev R (2010) Experimental constraints on ultrapotassic magmatism from the Bohemian Massif (durbachite series, Czech Republic) Contrib Mineral Petrol **159:** 331 - 347

Pearson DG, Canil D, Shirey SB (2004) Mantle samples included in volcanic rocks: xenoliths and diamonds. In: Carlson RW (ed) Treatise on Geochemistry. Volume 2: The Mantle and Core, Elsevier-Pergamon, Oxford, pp 171 - 275

Pilet S, Baker MB, Stolper EM (2008) Metasomatized lithosphere and the origin of alkaline lavas. Science **320:** 916 - 919

Rhodes JM (1981) Characteristics of primary basaltic magmas. *In:* Basaltic Volcanism on the Terrestrial Planets. Pergamon, New York, 409 - 432

Righter K, Carmichael ISE (1996) Phase equilibria of phlogopite lamprophyres from western Mexico: Biotite-liquid equilibria and P-T estimates for biotite-bearing igneous rocks. Contrib Mineral Petrol **123:** 1 - 21

Rock NMS (1977) The nature and origin of lamprophyres: Some definitions, distinctions, and derivations. Earth Sci Rev **13:** 123 - 169

Rock NMS (1987) The nature and origin of lamprophyres: An overview. In JG Fitton and BGJ Upton (eds), Alkaline Igneous Rocks. Blackwell Scientific. Oxford: pp 191 - 226

Rock NMS (1991) Lamprophyres. Blackie. Glasgow.

Rock NMS, Grove DI (1988). Do lamprophyres carry gold as well as diamonds? Nature **332:** 253 - 255

Rosenthal A, Foley SF, Pearson DG, Nowell GM, Tappe S (2009) Petrogenesis of strongly alkaline primitive volcanic rocks at the propagating tip of the western branch of the East African Rift. Earth Planet Sci Lett **284:** 236 - 248

Russel LS, Landes RW (1940) Geology of the southern Alberta plains. Geological Survey of Canada, Memoir **221:** 223

Sato K (1997) Melting experiments on a synthetic olivine lamproite composition up to 8 GPa: Implications to its petrogenesis. J Geophys Res **102:** 14,751 - 14,764

Scambos TA, Farmer GL (1988) Multiple source components for alkalic igneous rocks in the Wyoming Province: isotopic and trace element evidence from central Montana. EOS Transactions, American Geophysical Union, **69:** 1510

Smith D (2010) Antigorite Peridotite, Metaserpentinite, and other Inclusions within Diatremes on the Colorado Plateau, SW USA: Implications for the Mantle Wedge during Low-angle Subduction. J Petrol **51:** 1355 - 1379

Torsvik TH, Burke K, Steinberger B, Webb SJ, Ashwal LD (2010) Diamonds sampled by plumes from the core-mantle boundary. Nature **466:** 352 - 355

Van Kooten GK (1980) Mineralogy, petrology, and geochemistry of an ultra-potassic basaltic suite, central Sierra Nevada, California, USA. J Petrol **21:** 651 - 684

von Gumbel CW (1874) *Die Paleolithischen Eruptivgesteine des Fichtelgebirges*: Munich, Verlag Franz.

Wallace P, Carmichael ISE (1989) Minette lavas and associated leucitites from the Western Front of the Mexican Volcanic Belt: petrology, chemistry and origin. Contrib Mineral Petrol **103:** 470 – 492

Weed WH, Pirsson LV (1895) On the igneous rocks of the Sweetgrass Hills, Montana. Am J Sci, Vol L, No. 298: 309 - 313

Williams MY, Dyer WS (1930) Geology of southern Alberta and southwestern Saskatchewan. Geological Survey of Canada, Memoir **163:** 160

Woolley AR, Bergman SC, Edgar AD, Le Bas MJ, Mitchell RH, Rock NMS, Smith BS (1996) Classification of Lamprophyres, lamproites, kimberlites, and the kalsilitic, melilitic, and leucitic rocks. Can Mineral **34:** 175 - 196

Wyman D, Kerrich R (1988) Lamprophyres a source of gold. Nature **332:** 209 - 210

Chapter 2: Liquidus phase relations of a minette from the Milk River Area, southern Alberta, Canada[1]

2.1. Introduction:

The study of the liquidus mineralogy of a melt composition sheds light on the phases with which the melt equilibrated. The basic premise of a liquidus study, such as this one, is that the starting material represents a primary melt composition. That is, the melt composition that formed by partial melting has not been modified subsequently. This approach also assumes that equilibrium is achieved between the melt phase and the residue at a specific pressure. Therefore, this method assumes that the magma is derived via isobaric melting and does not react subsequently with its surroundings during ascent. If found, the multiple saturation point, the point at which several mineral phases crystallize at a single point along the liquidus, represents the pressure (P) and temperature (T) of melting, and the mineral assemblage is the residue of the source region from which the magma was derived.

Most mafic alkaline magmas, including lamprophyres, have paradoxical chemical compositions. They are hydrous, alkali-rich, and enriched in both major compatible (MgO) and incompatible elements (Cr, Ni, Co, Sc, large ion lithophile elements (LILE)), but are depleted in high field strength elements (HFSE), relative to basaltic mantle-derived melts. The mineralogy and composition of the source region for these magmas remains poorly constrained. Because of their unusual composition, they have been the subject of a number of previous petrologic and geochemical (Lloyd and Bailey 1975; Macdonald et al. 1992; Conticelli and Peccerillo 1992; Carlson and Nowell 2001; Orejana et al. 2008; Rosenthal et al. 2009) and experimental studies

[1] A version of this chapter was submitted for publication in *Contributions to Mineralogy and Petrology* as Funk S, Luth R, An experimental study of a minette from the Milk River area, southern Alberta, Canada.

(Lloyd et al. 1985; Esperanca and Holloway 1987; Righter and Carmichael 1996; Barton and Hamilton 1978, 1979; Edgar and Condliffe 1978; Edgar et al. 1976, 1980; Elkins-Tanton and Grove 2003; Parat et al. 2010). By and large, these authors converge on the conclusion that many mafic alkali magmas form by partial melting of a source containing clinopyroxene and phlogopite.

We conducted this study to shed light on the origin and physical conditions required to generate the minettes located in southern Alberta, near the Milk River area. Buhlmann et al. (2000) had previously studied the geochemistry and petrography of these minettes and their associated mica-clinopyroxenite xenoliths. They proposed, based on the experimental work of Esperanca and Holloway (1987), and extrapolating phase boundaries from Wallace and Carmichael (1989), that these minettes were derived from a source containing phlogopite + clinopyroxene ± olivine at pressures ≥ 1.7 GPa, probably closer to 3.0 GPa. The concentrations of Rb (~200 ppm), Cs (~3 ppm), and Nb (~13 ppm) in the minettes are consistent with the melting of phlogopite (Ionov et al. 1997; Pearson et al. 2004), whereas the high concentrations of Sr (~900-2000 ppm) and rare earth elements (REE) (Menzies 1983) are best explained with clinopyroxene in the source. The goal of this study was to test Buhlmann et al.'s hypothesis experimentally. Based on their hypothesis, we expected to find a multiple saturation point along the liquidus where clinopyroxene, mica, and possibly olivine, coexisted with liquid.

2.2. Starting Material:

Buhlmann et al. (2000) concluded that the sample RAB90 Au24-1 minette was the most primitive sample in the suite, based on Mg# (~73), MgO content (13.63 wt%), Cr (960 ppm) and Ni (664 ppm) concentrations (see Buhlmann et al. 2000 for details). As the most primitive of the

suite, we selected this sample as a possible candidate for a parental magma to study. The RAB90 Au24-1 minette is a fine-grained dyke with phenocrysts of phlogopite, diopside and altered olivine in a groundmass of clinopyroxene, sanidine, mica, oxides, apatite and in some cases carbonates. For our experiments, we used an aliquot of the natural rock powder prepared by Buhlmann in his original study (major element composition is given in **Table 2.1**).

2.3. Methodology:

Approximately 3 mg of powdered sample was packed tightly in a graphite inner capsule with dimensions ~4 mm tall, ~2.65 mm outer diameter (OD), and ~1.2 mm inner diameter (ID); the packed graphite capsule was loaded into a 3 mm OD Pt capsule. No additional water was added to these charges. The samples were placed in a 120°C oven overnight to dry prior to sealing by arc-welding. The capsules were run vertically in 12.7 mm talc-pyrex assemblies in solid-media, piston-cylinder apparatus (Boyd and England 1960) at the C.M. Scarfe Laboratory of Experimental Petrology, University of Alberta. The pressures were calibrated on the quartz-coesite transition at 1000°C, and on the jadeite-albite-quartz transition at 600 and 1000°C. It was determined that a -13% correction was required to correct the nominal pressures. Temperatures were monitored with W95Re5-W74Re26 thermocouples with no corrections made for the effect of pressure on the emf of the thermocouple.

Experiments to locate the liquidus and characterize its mineralogy were conducted between 1.33 GPa to 2.21 GPa and between 1300°C to 1400°C (**Table 2.2**). Each experiment was brought up to ~80% pressure. The sample was then heated to the desired temperature, and finally the pressure was brought up to its final value. The duration of experiments ranged from one to two days, depending on temperature.

The compositions of the phases in the run products were determined using the JEOL 8900R electron microprobe at the Department of Earth and Atmospheric Sciences, University of Alberta. All experiments were analyzed at 15 kV acceleration potential. For the mineral grains, a beam current of 15 nA was used with a beam diameter of 1-3 μm. The beam current was reduced to 10 nA and the beam diameter widened to 10 μm on the glasses. To mitigate the effect of alkali migration during glass analyses, K and Na were analysed first. For all analyses, counting times were 20 seconds on peak, and 10 seconds on the background. Natural mineral standards were used (**Table 2.3**). The data acquired from the electron microprobe was corrected using the phi-rho-zed (PRZ) program provided by JEOL. Standard deviations were calculated to assess compositional variability.

2.4. Results:

2.4.1. Liquidus Temperature and Mineralogy:

The P-T location of the liquidus and its mineralogy for our Milk River minette is well constrained within the investigated pressure range of this study. **Figure 2.1** shows the phase relationships along the liquidus, and **Tables 2.4-2.6** provides the average compositions of the liquidus phases. At 1.33 GPa and 1.77 GPa, the liquidus is bracketed between 1350°C and 1375°C, whereas at 2.0 GPa and 2.21 GPa it is between 1375°C and 1400°C. At 1.55 GPa, the liquidus is bracketed between 1325°C and 1375°C. At 1.33 GPa and 1350°C, olivine with an average Mg# = 90.9 coexists with a melt with Mg# = 75.8. At 1.55 GPa and 1325°C, olivine with an average Mg# = 90.5 coexists with a melt with Mg# = 75.9. At 2.0 GPa and 1375°C, orthopyroxene with an average Mg# = 90.9 coexists with a melt with Mg# = 76.8. At 2.21 GPa and 1375°C, orthopyroxene with an average Mg# = 89.4 coexists with a melt with Mg# = 71.0.

At 1.77 GPa, both olivine (Mg# = 88.6), and orthopyroxene (Mg# = 89.2) coexist with a liquid (Mg# = 72.4), forming a multiple saturation point at 1350°C.

2.4.2. Melt Composition:

Below the liquidus, the composition of the liquid (**Table 2.4**) changes with temperature and pressure depending on the mineral phase or phases crystallizing. At 1.33 GPa, where olivine crystallizes, the SiO_2, Al_2O_3, CaO and TiO_2 content in the glass increases with decreasing MgO content (**Figures 2.2a-d**). The compositions of Na_2O, K_2O, and P_2O_5 in the glass also increase with decreasing MgO content. Above 1.77 GPa, SiO_2 decreases with decreasing MgO content, a reflection of crystallizing the silica-rich orthopyroxene (**Figure 2.2a**). The behaviour of TiO_2, Al_2O_3, CaO, Na_2O, K_2O, and P_2O_5 remains unchanged as a function of pressure.

2.4.3. Olivine Composition:

Olivine grains are typically prismatic and are subhedral to euhedral. They are small, ranging from ~10-50 μm in diameter, and are chemically homogeneous. Olivine is stoichiometric, with Mn and Ca substituting for Mg and Fe (**Table 2.5**). Manganese decreases with increasing temperatures (**Figure 2.3**), consistent with the experimental study of Snyder and Carmichael (1992) of olivine-melt equilibrium. In our experiments, olivine incorporates ~0.2-0.3 wt% CaO (**Table 2.5**), independent of temperature and pressure. As temperatures approach the liquidus, the Mg# in olivine increases (**Figure 2.4**). This is expected because magnesium stabilizes olivine to higher temperatures.

2.4.4. Orthopyroxene Composition:

Orthopyroxene is prismatic and euhedral, growing up to ~50 μm in diameter. All orthopyroxene grains are homogenous and unzoned. All our orthopyroxene incorporates ~2 wt% Al_2O_3 (**Table 2.6**), and at 2.21 GPa, the Al_2O_3 content decreases as temperature approaches the liquidus. The CaO content in orthopyroxene is ~2 wt% (**Table 2.6**), and does not vary systematically with respect to temperature or pressure.

2.4.5. Iron Loss:

Loss of iron by alloying with the outer Pt capsule was an issue during our experiments. The loss of iron makes the bulk composition more Mg-rich, which would shift the liquidus to higher temperatures. Ascertaining the exact percentage of iron loss is difficult. Modal abundances were calculated without FeO* to remove any bias due to iron loss. The calculated modes were used to reconstruct the bulk composition of our experiments. Comparing the reconstructed composition with the original starting material yields an estimate of the percentage of iron loss (general expression given in **Table 2.2**). We also estimated the percentage of iron loss in other experimental papers (Barton & Hamilton 1979; Lloyd et al. 1985; Esperanca and Holloway 1987; Sweeney et al. 1993) with similar compositions and similar capsule designs using our expression. We obtain a range for iron loss that is similar to those estimated by the previous authors (1-20%), lending credence to our calculations.

Our results show that our experiments had ~3-25% iron loss, although many are within ~10-25% (**Table 2.2**). We estimate a similar range for the other studies. Sweeney et al. (1993) argued that ~14-18% iron loss was not significant enough to affect the phase relations or the relative appearance of phases. To see how much the phase boundaries would shift with 25% loss

in FeO, we used pMELTS (Ghiorso et al. 2002) to calculate ideal phase diagrams (one diagram had the mineralogy constrained to only allow olivine, orthopyroxene and liquid; the other was left unconstrained) for RAB90 Au24-1. The results from pMELTS show that a 25% loss in FeO shifts phase boundaries up by ~20-30°C, but the relative order of appearance of phases remains unchanged. We also compared the phase diagrams for RAB90 Au24-1 with 10% and 25% loss in FeO. We found that within the investigated pressures of this study and with a 25°C uncertainty, the liquidus temperatures for both phase diagrams were indistinguishable. We conclude that the iron loss experienced in our experiments will not affect the mineralogy of the crystalline phases, and that the range of iron loss between each experiment will not noticeably change the liquidus location in P-T space.

2.4.6. Mineral-liquid Equilibria:

To ascertain whether our experiments were at equilibrium we used mineral-liquid exchange coefficients. Roeder and Emslie (1970) found that the Fe-Mg exchange coefficient between olivine and liquid, $K_D(Fe\text{-}Mg)^{ol\text{-}liq}$, varied between 0.26 and 0.36. They concluded that equilibrium, with respect to Fe-Mg exchange, can be assured if $K_D(Fe\text{-}Mg)^{ol\text{-}liq}$ are within this range. Within the resolution of their study, they found that the exchange coefficient was independent of melt composition and temperature. However, subsequent studies on alkaline magmas have found that this is not the case (Sack et al. 1987; Gee and Sack 1988). Gee and Sack (1988) found that $K_D(Fe\text{-}Mg)^{ol\text{-}liq}$ decreases with decreasing silica content, or conversely, increasing alkalis. Tholeiites to alkali basalts have exchange coefficients ranging from 0.33 to 0.27; at lower silica activities, olivine melilitites to nephelinites have exchange coefficients ranging from 0.25 to 0.17. Our calculated $K_D(Fe\text{-}Mg)^{ol\text{-}liq}$ values (0.31-0.36; **Table 2.7**) are

higher than the range given by Gee and Sack (1988), but are within the range given by Roeder and Emslie (1970).

As with olivine-liquid, orthopyroxene and melt have an analogous Fe-Mg exchange reaction. In this case, equilibrium values of $K_D(Fe\text{-}Mg)^{opx\text{-}liq}$ are 0.29±0.06 (Putirka 2008). This value is independent of pressure and temperature (Putirka 2008). All of our values are in this range (**Table 2.7**). Based on these calculations, we believe that our experiments, with respect to Fe-Mg exchange, are in equilibrium and can be used to construct phase relations.

2.4.7. Geothermometry:

As a second independent test for equilibrium, we calculated temperatures for our experiments using different geothermometers. Detailed explanations of the empirical fitting, statistics, sample calculations and review of the various glass-only and mineral-liquid geothermometers that are used in this study, are in Putirka et al. (2007) and Putirka (2008). **Table 2.8** provides the temperatures calculated from the glass-only, olivine-liquid, and the orthopyroxene-liquid thermometers.

The glass-only thermometer (equation 14 of Putirka 2008) was chosen because the range of pressures, temperatures, and compositions of glasses against which it was calibrated makes it appropriate for our system. This thermometer assumes saturation of hydrous mafic melts with olivine (Putirka 2008), and is applicable therefore only for our low-pressure experiments. The uncertainty of equation 14 is reported to be ±51°C (Putirka 2008). Of the experiments containing olivine, the calculated temperatures differ from the measured ones by ~25°C.

In conjunction with the glass-only thermometers, an olivine-liquid thermometer from Putirka et al. (2007), their equations 2 (distribution coefficient) and 4 (the olivine-liquid

thermometer), were used to calculate temperature for our low-pressure experiments. Putirka et al. (2007) used a non-linear regression to produce new olivine-liquid thermometer equations, based on work by Beattie (1993) and building upon the pressure sensitivity noted by Herzberg and O'Hara (2002). Putirka et al. reported an uncertainty of ±52°C for their expression. When the two equations are coupled, the calculated temperatures for our system are systematically lower by ~20-50°C than the measured temperature of the experiment (**Table 2.8**). They do agree, however, within the stated uncertainty.

At higher pressures, where olivine is no longer stable, an orthopyroxene-liquid thermometer, equation 28a from Putirka (2008), was used. Equation 28a was based on previous work from Beattie (1993). With the exception of experiment SPF40 (and with other experiments not used in this study due to extensive Fe loss; see Appendix E), the thermometer recovers temperatures to within the uncertainty of ±41°C (Putirka 2008). The larger deviation in SPF40 could be due to the significant (~20%) iron loss experienced during the experiment.

Although calibrated on more mafic and less alkaline compositions than ours, these geothermometers reproduce run temperatures well. Of the thermometers utilized in this study, the orthopyroxene-liquid thermometer may be the best test for equilibrium and may be used to flag potential problems with iron loss. We conclude equilibrium is best evaluated using multiple geothermometers. Coupled together, along with textural observations and mineral-liquid exchange coefficients, consistent calculated values argue for equilibrium.

2.5. Discussion:

2.5.1. Implications for vein-melting and wall-rock re-equilibration:

Buhlmann et al. (2000) suggested that the Milk River minettes were derived from a mantle source containing phlogopite, clinopyroxene, and possibly olivine, at ~3.0 GPa (~100 km). This hypothesis is supported by many previous studies. Lloyd and Bailey (1975) studied high-potassium rocks from Uganda, and suggested derivation by partial melting of a phlogopite clinopyroxenite. This was proven plausible by the subsequent forward experimental study of Lloyd et al. (1985). Macdonald et al. (1992) concluded that the potassic mafic lavas from the Bearpaw Mountains in Montana most likely originated via melting of a source containing olivine, phlogopite and clinopyroxene at pressures ~3.0 GPa. Conticelli and Peccerillo (1992) suggested that the potassium-rich magmas from central Italy were produced by melting a phlogopite pyroxenite. Carlson and Nowell (2001) conducted an isotopic study of alkaline igneous rocks from the Colorado Plateau. Using the Re-Os and Lu-Hf isotopic systems, they concluded that the least silica-saturated magmas, known as katungites, were probably derived by partial melting of mica-clinopyroxenites. Based on the isotopic characteristics and geochemistry of alkaline lamprophyres from the Spanish Central System in Western Europe, Orejana et al. (2008) suggested a metasomatized peridotitic source rich in phlogopite. In the study of ultramafic lamprophyres that erupted in northern Labrador and Quebec in eastern Canada, Tappe et al. (2008) suggested these magmas formed by fusion of a mica-amphibole-rutile-ilmenite-diopside (MARID)-type metasome assemblage induced by fluxing of a carbonate-rich fluid. Rosenthal et al. (2009) used Sr-Nd-Hf-Os isotopic systematics to characterize the source region of kamafugites from the western branch of the East African Rift. They found that the

kamafugites were derived from mixing between a phlogopite-rich MARID-like component, and a carbonate- and phlogopite-rich metasome at depths > 100 km.

In addition to petrographic and geochemical studies noted above, most of the experimental studies on mafic alkaline magmas (**Table 2.9**), not confined only to lamprophyres, have nearly all converged on the same conclusion. They mostly found olivine + clinopyroxene + phlogopite as liquidus phases at a multiple saturation point (Esperanca and Holloway 1987; Righter and Carmichael 1996; Barton and Hamilton 1978, 1979; Edgar and Condliffe 1978; Edgar et al. 1976, 1980; Elkins-Tanton and Grove 2003; Parat et al. 2010). At higher pressures, usually ≥ 3.0 GPa, garnet was an additional stable liquidus phase (Nicholls and Whitford 1983; Mitchell 1995). In most studies, with the exception of Edgar et al. (1976, 1980) and Sato (1997), orthopyroxene is absent as a stable liquidus phase. Foley (1992a) suggested that orthopyroxene in alkaline magmas is stabilized by higher CO_2 contents in the coexisting C-O-H fluid. From these studies on alkaline magmas, it has generally been concluded that a phlogopite clinopyroxenite may be the source lithology of many mafic alkaline magmas, and therefore a crucially important lithology in the lithospheric mantle.

Finding orthopyroxene and olivine, rather than clinopyroxene and phlogopite, as major liquidus mineral phases for a composition such as ours is unusual. These findings are inconsistent with the hypothesis proposed by Buhlmann et al. (2000) and does not fit with the overall consensus from geochemical, petrological and experimental studies on magmas of similar compositions. Our experiments are not the first to find multiple saturation of orthopyroxene and olivine. Arima and Edgar (1983) studied the liquidus phase relationships of a leucite lamproite (wolgidite) from the West Kimberly area, Australia between 1.0 to 4.0 GPa and with 3.22 and 13.0 wt% H_2O added. They found that in experiments with 13.0 wt% H_2O, olivine was the

liquidus phase up to 2.4 GPa; orthopyroxene was the liquidus phase above 2.4 GPa. Phlogopite and rutile crystallized close to the liquidus in experiments above 1.6 GPa. They concluded that the wolgidite magma could come from a source containing phlogopite, rutile, olivine and orthopyroxene. Foley (1993) conducted liquidus experiments from 4.5 to 5.5 GPa on an olivine lamproite from the West Kimberly region, in the presence of reduced fluids. He found that olivine was the liquidus phase up to 5.0 GPa, above which orthopyroxene and phlogopite co-crystallize along the liquidus. Foley concluded that these rocks were derived from partial melting of a phlogopite harzburgite.

However, features of our minette whole-rock composition, such as the high TiO_2 (1.02 wt%), CaO (8.02 wt%) and K_2O (4.44 wt%), are most reasonably explained by melting of a source containing phlogopite and clinopyroxene. This inference is also consistent with the trace element concentrations, such as high Rb (146 ppm), Cs (1.2 ppm), Nb (12 ppm) and Ba (3239 ppm) indicating phlogopite was in the source, whereas high Sr (993 ppm) could indicate clinopyroxene was in the source (Buhlmann et al. 2000). To reconcile this with the observed liquidus mineralogy, we turn to another model.

Navon and Stolper (1987) suggested the upper mantle may act as a chromatographic column. They noted that a magma rising through wall-rock is most likely in disequilibrium with it, thus reactions between the magma and wall-rock are bound to occur. Therefore, when the "primary minette magma" rises through the upper mantle, the melt would re-equilibrate with the wall-rock lithology. Foley (1992b) further refined this idea and proposed a mechanism for vein plus wall-rock assimilation and re-equilibration with potassic magmas: the dissolution of wall-rock minerals. In Foley's model, melts derived from partial melting of veins dissolve the wall-rock minerals to establish equilibrium between the melt and the wall-rock. Foley noted that

olivine and/or orthopyroxene dissolves preferentially through this method as these are the minerals farthest from equilibrium with strongly alkaline magmas. The composition of the liquidus olivine and orthopyroxene at the multiple saturation point falls within the accepted range of mantle values (noteably the Mg#), and therefore it is reasonable to conclude that our "primary minette magma" re-equilibrated with mantle harzburgite during its ascent.

Our results demonstrate that this minette was last in equilibrium with a residue containing orthopyroxene and olivine at ~1.77 GPa (~58 km) at 1350°C. At a depth of ~58 km (which is below the modern-day crustal thickness; Lemieux et al. 2000; Gorman et al. 2002), the temperature of the surrounding wall-rock in the craton is ~600-700°C, based on a 40 mW m^{-2} geotherm (Chapman and Pollack 1977). We argue that it is unlikely that the vein-imbedded wall-rock at ~58 km rose by ~600°C to induce partial melting, as the location of the Milk River minettes (ca. 50 Ma; Buhlmann et al. 2000) do not correlate with any known mantle plume tracks (Heaman et al. 2003) or sites of mantle upwelling (Torsvik et al. 2010). Instead, we believe that partial melting likely occurred at the base of the Wyoming craton (~150-220 km; Gorman et al. 2002; Yuan and Romanowicz 2010; Schmandt and Humphreys 2010). At greater depths, the solidus of a mica-clinopyroxenite vein assemblage is closer to the normal cratonic geotherm (~1400°C at 200 km), and therefore minimal heating is required to induce partial melting (Foley et at 1999). It is generally excepted that the presence of xenoliths in volatile- and alkali-rich magmas (such as minettes) supports the hypothesis that they were transported to the surface rapidly through fractures in the lithosphere (Sparks et al. 1977; Spera 1984). A consequence of rapid ascent rates, coupled with slow cooling rates, is that the "primary minette magma" would preserve the high (near-liquidus) temperatures of melting (Sparks et al. 1977; Spera 1984).

Therefore, we propose that the source region for these minettes consists mainly of a harzburgite wall-rock lithology imbedded with metasomatic veins of mica and clinopyroxene located at or near the base of the Wyoming craton. Either some thermal perturbation (e.g. friction from the shallow-angled Farallon plate; Humphreys 2009) or the introduction of hydrous fluids (possibly derived from the Farallon plate; O'Brien et al 1991, 1995; Currie and Beaumont 2011), induced partial melting ca. 50 Ma (Buhlmann et al. 2000). Melting occured in the veins because of their high abundance of volatiles, and therefore lower solidus temperature. Then, the "primary minette magma" ascends through the lithospheric mantle rapidly, preserving a near-liquidus temperature, where it stalled at ~58 km. Because the "primary minette magma" is in disequilibrium with its surroundings, dissolution of orthopyroxene and olivine into the melt occurs. This process brought the minette melt into equilibrium with olivine and orthopyroxene and imparted a strong refractory harzburgite signal onto the minette.

2.6. Conclusions:

The liquidus mineralogy of this minette composition consists of olivine and orthopyroxene. Multiple saturation of these minerals was found at ~1.77 GPa and ~1350°C. This result is inconsistent with many previous studies on similar rocks. Based on the composition of the minette magma (e.g. high CaO and K_2O contents), we propose that these minettes were likely derived from a source containing mica and clinopyroxene, and later re-equilibrated with a harzburgite. The unusually high temperature of multiple saturation cannot be explained by simple melting models. We argue that partial melting likely occurred at the base of the Wyoming craton (located ~150-220 km depth), where either a slight thermal perturbation or the introduction of hydrous fluids could easily induce partial melting. Rapid ascent rates (coupled with slow cooling rates) of the "primary minette magma" preserved the high temperature of

fusion. We interpret the pressure of multiple saturation (~58 km) as the depth where the "primary minette magma" stalled in the subsurface, where it experienced very near to total re-equilibration with a surrounding mantle harzburgite wall-rock. Therefore, we conclude that the minette studied is not primary, but may still be parental to the other minettes found in the same location.

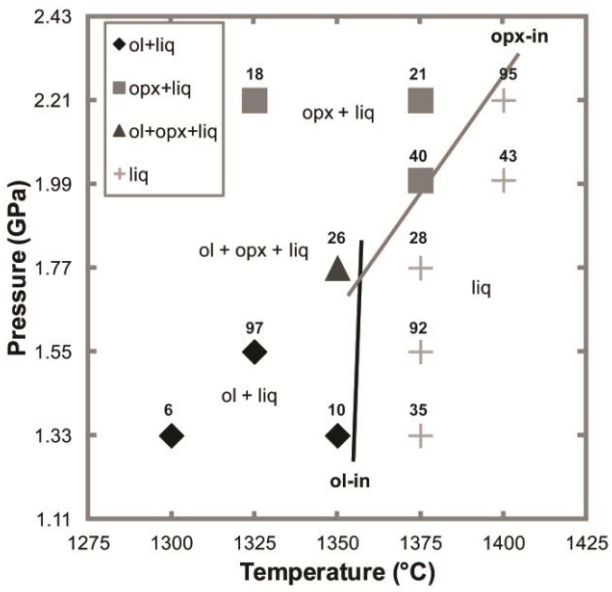

Figure 2.1 Liquidus phase relationships in PT-space. The number above each symbol denotes the experiment number. The black solid line shows the constrained olivine (ol)-in reaction boundary, whereas the dark grey solid line shows the constrained orthopyroxene (opx)-in reaction boundary

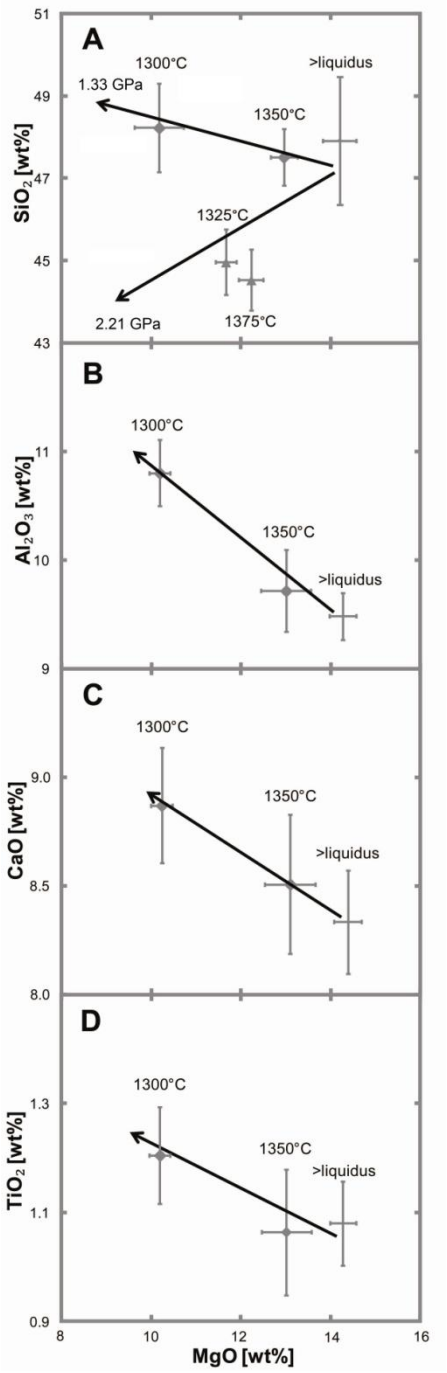

Figures 2.2a-d Variation in chemical composition of glasses. **b-d** are at 1.33 GPa. Errors are plotted to 2σ. Symbols: diamond = ol + L; triangle = opx + L; no symbol = L. Arrows are best-fit trends

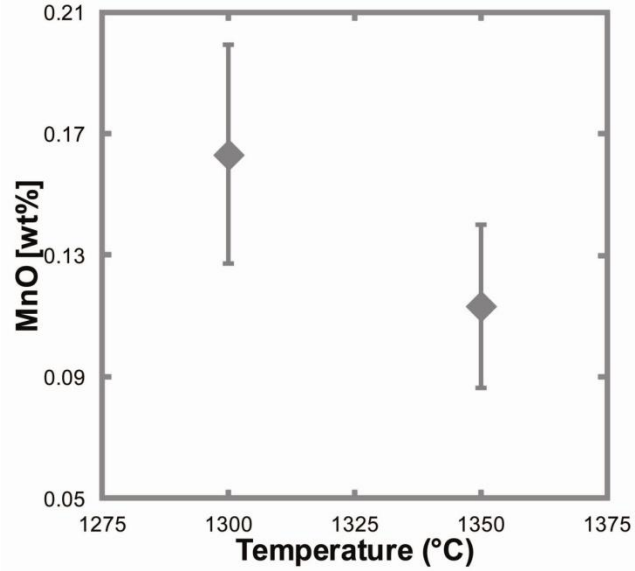

Figure 2.3 MnO (wt%) in olivine versus temperature for experiments at P = 1.33 GPa. Errors plotted are 2σ

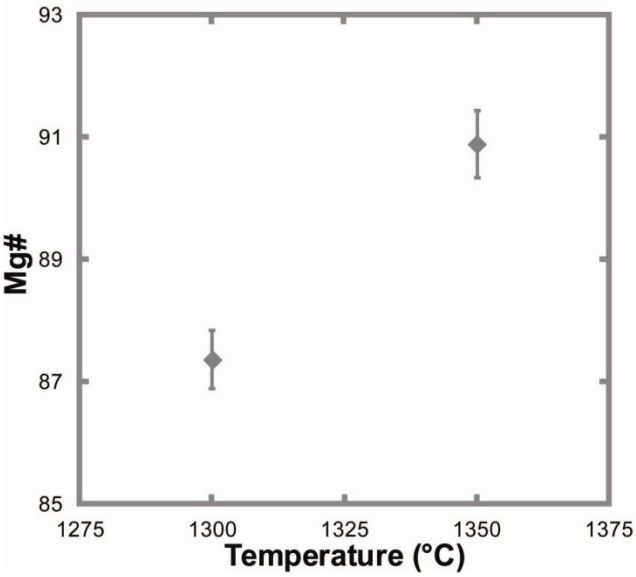

Figure 2.4 Mg# of olivine versus temperature for experiments at P = 1.33 GPa. Errors plotted are 2σ

Table 2.1 Composition of starting material

[wt%]	RAB90 Au24-1	Volatile Free
SiO_2	45.34	48.68
TiO_2	1.02	1.10
Al_2O_3	9.22	9.90
FeO^*	9.00	9.66
MnO	0.14	0.15
MgO	13.63	14.64
CaO	8.02	8.61
Na_2O	1.30	1.40
K_2O	4.44	4.77
P_2O_5	1.02	1.10
H_2O	4.64	---
Total	97.77	100.00

Major element compositions were acquired by XRF analysis (fusion) (Buhlmann et al. 2000).

FeO* = total iron

Table 2.2 List of run conditions

Run Name	Pressure (GPa)	Temperature (°C)	Time (hrs)	% Fe loss	Phase Assemblage
SPF6	1.33	1300	26.5	6.3	(10.7)ol, (89.3)liq; $\sum R^2 = 0.227$
SPF10	1.33	1350	23	17.5	(3.1)ol, (96.9)liq; $\sum R^2 = 0.065$
SPF35	1.33	1375	48	22.9	liq; $\sum R^2 = 0.322$
SPF97	1.55	1325	22.5	16.9	(3.0)ol, (97.0)liq; $\sum R^2 = 0.699$
SPF92	1.55	1375	25	24.4	liq; $\sum R^2 = 0.125$
SPF26	1.77	1350	48	7.5	(2.6)ol, (3.2)opx, (94.2)liq; $\sum R^2 = 0.094$
SPF28	1.77	1375	23	11.6	liq; $\sum R^2 = 0.165$
SPF40	2.0	1375	24	20.8	(2.0)opx, (98.0)liq; $\sum R^2 = 0.032$
SPF43	2.0	1400	24	19.5	liq; $\sum R^2 = 0.299$
SPF18	2.21	1325	25	10.9	(11.7)opx, (88.3)liq; $\sum R^2$ 0.045
SPF21	2.21	1375	24	3.5	(7.8)opx, (92.2)liq; $\sum R^2 = 0.022$
SPF95	2.21	1400	22.5	24.4	liq; $\sum R^2 = 0.641$

Pressures are accurate to ±0.1 GPa. Temperatures are accurate to ±25°C. Values in parentheses indicate calculated modal abundances for mineral phases; sum of residual squares ($\sum R^2$) given to the right. Modal percentages were calculated using mass balance equations excluding FeO*. % Fe Loss = $(FeO_{RAB90\ Au24\text{-}1} - \sum X_P\, FeO_P)/FeO_{RAB90\ Au24\text{-}1}$, where $FeO_{RAB90\ Au24\text{-}1} = 9.00$, X_P = modal abundance for phase P in the run products, and FeO_P = FeO for phase P in the run products. Abbreviations: ol = olivine, opx = orthopyroxene, liq = liquid

Table 2.3 List of standards

Standard	Element
Albite	Na
Apatite	P, F
Diopside	Ca, Si
Hematite	Fe
Pyrope	Al
Rutile	Ti
Willemite	Mn
Fo93	Mg
Orthoclase	K
Tugtupite	Cl

Table 2.4 Average glass analyses

Sample	SPF6	SPF10	SPF35	SPF97	SPF92	SPF26	SPF28	SPF40	SPF43	SPF18	SPF21	SPF95
P (GPa)	1.33	1.33	1.33	1.55	1.55	1.77	1.77	2.0	2.0	2.21	2.21	2.21
T (°C)	1300	1350	1375	1325	1375	1350	1375	1375	1400	1325	1375	1400
Time (hrs)	26.5	23	48	24	25	48	23	24	24	25	24	22.5
n	40	68	79	68	194	64	112	100	79	33	20	102
SiO_2	48.2(11)	47.5(7)	48.9(11)	47.1(5)	47.5(5)	46.1(3)	46.8(4)	45.2(22)	47.9(9)	45.0(8)	44.5(7)	46.8(6)
TiO_2	1.2(1)	1.1(1)	1.1(1)	1.1(1)	1.1(1)	1.10(9)	1.06(9)	1.01(9)	1.08(9)	1.14(8)	1.09(6)	1.08(9)
Al_2O_3	10.8(4)	9.7(2)	9.7(2)	9.7(2)	9.7(2)	10.2(2)	9.3(2)	9.5(4)	9.5(2)	10.4(2)	9.8(3)	9.4(2)
FeO*	8.0(3)	7.4(2)	6.9(2)	7.4(2)	6.8(2)	8.3(2)	8.0(2)	7.2(4)	7.2(2)	8.2(2)	8.9(2)	6.8(2)
MnO	0.14(5)	0.15(4)	0.14(6)	0.14(5)	0.14(5)	0.14(4)	0.13(6)	0.14(7)	0.13(6)	0.14(3)	0.15(5)	0.14(6)
MgO	10.2(6)	13.0(3)	14.3(3)	13.1(2)	14.4(3)	12.2(3)	14.1(3)	13.4(7)	14.1(3)	11.7(2)	12.2(3)	14.3(3)
CaO	8.9(3)	8.5(2)	8.3(2)	8.5(1)	8.2(1)	8.4(1)	8.6(2)	8.2(5)	8.0(1)	8.8(2)	8.4(2)	8.3(2)
Na_2O	1.5(4)	1.3(2)	1.2(2)	1.3(1)	1.25(8)	1.4(1)	1.30(9)	1.4(5)	1.3(5)	1.3(3)	1.4(4)	1.26(9)
K_2O	5.2(3)	4.7(1)	4.6(1)	4.78(9)	4.5(1)	4.89(7)	4.4(2)	4.6(2)	4.6(2)	5.1(2)	4.9(2)	4.5(1)
P_2O_5	1.3(1)	1.1(1)	1.18(9)	1.1(1)	1.1(1)	1.1(2)	1.1(1)	1.1(1)	1.13(9)	1.2(1)	1.15(9)	1.1(1)
F	0.43(6)	0.43(6)	0.41(7)	0.41(7)	0.41(7)	0.39(7)	0.42(9)	0.38(8)	0.36(7)	0.40(6)	0.42(10)	0.39(6)
Cl	0.02(2)	0.02(2)	<d.l.	<d.l.	<d.l.	<d.l.	<d.l.	<d.l.	<d.l.	<d.l.	<d.l.	0.02(2)
Total	95.89	94.90	96.73	94.63	95.10	95.02	95.21	92.13	95.30	93.38	92.91	94.09
Mg#	69.4	75.8	78.7	75.9	79.1	72.4	75.9	76.8	77.7	71.8	71.0	78.9

Errors are given in parentheses as 2σ in the last decimal place. n = number of analyses. FeO* = total iron. <d.l. = below detection limits. Detection limits for all elements are ≤ 150 ppm, except for Ti (~250 ppm), Fe (~200 ppm), F (~300 ppm). Mg# = Mg/(Mg+Fe*)

Table 2.5 Average olivine analyses

Run	**SPF6**	**SPF10**	**SPF97**	**SPF26**
P (GPa)	1.33	1.33	1.55	1.77
T(°C)	1300	1350	1325	1350
time (hrs)	26.5	23	24	48
n	18	2	24	5
SiO_2	41.0(17)	39.8(3)	40.0(8)	40.1(10)
TiO_2	<d.l.	<d.l.	<d.l.	<d.l.
Al_2O_3	<d.l.	<d.l.	<d.l.	<d.l.
FeO*	11.9(13)	9.1(1)	9.4(2)	11.0(3)
MnO	0.16(3)	0.10(1)	0.13(4)	0.11(2)
MgO	46.5(18)	51.3(39)	49.1(14)	47.9(8)
CaO	0.27(5)	0.23(4)	0.29(10)	0.24(1)
Na_2O	<d.l.	<d.l.	<d.l.	<d.l.
K_2O	<d.l.	<d.l.	<d.l.	<d.l.
Total	99.83	100.53	98.92	99.34
On the basis of 4 oxygens				
Si	1.01(2)	0.97(3)	0.99(2)	0.99(1)
Fe*	0.25(1)	0.186(9)	0.19(2)	0.23(1)
Mn	0.0034(5)	0.0021(2)	0.0028(3)	0.0023(1)
Mg	1.71(5)	1.87(8)	1.81(14)	1.77(1)
Ca	0.007(1)	0.006(1)	0.008(2)	0.006(1)
Mg#	87.6	90.9	90.5	88.6

Errors are given in parentheses as 2σ in the last decimal place. n = number of analyses. <d.l. = below detection limits. FeO* = total iron. Detection limits for all elements are ≤100 ppm, except for Ti (~150 ppm) and Fe (~150 ppm). Mg# = Mg/(Mg+Fe*)

Table 2.6 Average orthopyroxene analyses

Sample	**SPF26**	**SPF40**	**SPF18**	**SPF21**
P (GPa)	1.77	2.0	2.21	2.21
T (°C)	1350	1375	1325	1375
Time (hrs)	48	24	25	24
n	1	6	26	1
SiO_2	56.4(2)	57.2(14)	56.1(4)	56.4(1)
TiO_2	0.14(3)	0.10(5)	0.10(3)	0.09(3)
Al_2O_3	2.1(1)	1.9(1)	2.0(2)	1.7(1)
FeO*	6.8(1)	5.7(3)	6.7(2)	6.7(1)
MnO	0.12(2)	0.12(2)	0.13(2)	0.12(7)
MgO	31.6(10)	32.1(10)	31.6(7)	32.0(7)
CaO	2.05(5)	1.7(2)	2.3(3)	1.9(1)
Na_2O	0.07(4)	0.1(1)	0.1(1)	0.05(10)
K_2O	<d.l.	<d.l.	<d.l.	<d.l.
P_2O_5	<d.l.	<d.l.	<d.l.	<d.l.
Total	99.28	98.92	99.03	98.96
On the basis of 6 oxygens				
Si	1.95(4)	1.97(5)	1.96(2)	1.974(2)
Ti	0.004(1)	0.003(4)	0.0026(7)	0.0022(9)
Al	0.87(4)	0.089(6)	0.084(2)	0.068(1)
Fe*	0.199(2)	0.17(2)	0.196(7)	0.197(5)
Mn	0.004(1)	0.004(1)	0.0040(7)	0.004(2)
Mg	1.67(8)	1.7(1)	1.65(3)	1.67(2)
Ca	0.077(2)	0.07(5)	0.09(2)	0.074(1)
Na	0.005(3)	0.008(8)	0.008(8)	0.003(7)
Mg#	89.2	90.9	89.4	89.4

Errors are given in parentheses as 2σ in the last decimal place. n = number of analyses. <d.l. = below detection limit. FeO* = total iron. Detection limits for all elements are ≤100 ppm, except for Ti (~180 ppm) and Fe (~150 ppm). Mg# = Mg/(Mg+Fe*)

Table 2.7 Fe-Mg exchange coefficients for olivine-liquid and orthopyroxene-liquid

Sample	T (°C)	P (GPa)	$K_D(Fe\text{-}Mg)^{ol\text{-}liq}$	$K_D(Fe\text{-}Mg)^{opx\text{-}liq}$
SPF 6	1300	1.33	0.36	-
SPF 10	1350	1.33	0.31	-
SPF 97	1325	1.55	0.34	-
SPF 26	1350	1.77	0.34	0.32
SPF 40	1375	2.0	-	0.33
SPF 18	1325	2.21	-	0.30
SPF 21	1375	2.21	-	0.29

Calculations for the exchange coefficient are based on the reaction Mg (mineral) + Fe^{2+} (melt) ↔ Mg (melt) + Fe^{2+} (mineral). General formula: $K_D(Fe-Mg)^{\min-melt} = (X_{FeO}^{\min} X_{MgO}^{melt})/(X_{FeO}^{melt} X_{MgO}^{\min})$, where X_z^y = mole fraction of oxide z in phase y

Table 2.8 Calculated temperatures using geothermometers from Putirka et al. (2007) and Putirka (2008)

	Run Conditions		glass-only	ol-liq	opx-liq
Sample	**T (°C)**	**P (GPa)**	**T (°C)**	**T (°C)**	**T (°C)**
SPF6	1300	1.33	1275	1277	-
SPF10	1350	1.33	1340	1299	-
SPF35	1375	1.33	1390	-	-
SPF97	1325	1.55	1340	1290	-
SPF92	1375	1.55	1377	-	-
SPF26	1350	1.77	1333	1315	1331
SPF40	1375	2.0	-	-	1313
SPF18	1325	2.21	-	-	1332
SPF21	1375	2.21	-	-	1335

Run conditions are provided for comparison with the calculated values for the temperature

Table 2.9 Composition of various mafic alkaline magma starting materials used in other experimental studies

	Esperanca and Holloway (1987)	Righter and Carmichael (1996)	Barton and Hamilton (1979)	Edgar et al. (1976)	Edgar et al. (1978, 1980)	Elkins-Tanton and Grove (2003)	Nicholls and Whitford (1983)	Mitchell (1995)	Sato (1997)	Parat et al. (2010)
SiO_2	51.02	50.42	43.56	43.13	44.16	44.40	45.17	56.3	46.08	52.70
TiO_2	2.10	1.79	2.31	5.37	1.86	1.19	1.26	2.49	3.49	1.27
Al_2O_3	10.91	13.00	7.85	8.40	9.95	12.91	13.62	10.5	4.34	13.53
FeO^*	8.00	7.50	5.86	8.08	10.87	8.73	9.39	3.55	8.79	6.89
MnO	0.12	0.14	0.15	0	0.17	0.16	0.17	0.88	0	0.11
MgO	10.25	9.74	11.03	16.00	20.38	14.23	10.39	6.34	27.54	8.51
CaO	9.41	7.84	11.89	10.83	8.78	11.61	13.27	3.11	5.30	4.92
Na_2O	2.14	2.96	0.74	0.81	1.56	2.39	2.60	1.25	0.43	1.63
K_2O	5.05	5.29	7.19	7.19	1.75	3.15	3.10	11.25	4.02	6.67
P_2O_5	1.01	1.31	1.50	0	0.37	1.10	1.02	1.35	0	1.25
H_2O^+	4.37	0.99	2.89	Var.	Var.	Var.	Var.	0.9	Var.	Var.
Total	100.01	100.98	94.97	99.81	99.85	99.87	99.99	97.93	99.99	97.48

Details of chemical analyses can be found for each respective paper. FeO* = total iron. Var. = variable composition

References:

Arima M, Edgar AD (1983) A high pressure experimental study on a magnesium-rich leucite-lamproite from the West Kimberly area, Australia: petrogenetic implications. Contrib Mineral Petrol **84:** 228 - 234

Barton M, Hamilton DL (1978) Water-saturated melting relationships to 5 kbars of three Leucite Hills lavas. Contrib Mineral Petrol **66:** 41 - 49

Barton M, Hamilton DL (1979) The melting relationships of a madupite from the Leucite Hills, Wyoming, to 30 Kb. Contrib Mineral Petrol **69:** 133 - 142

Beattie P (1993) Olivine-melt and orthopyroxene-melt equilibria. Contrib Mineral Petrol **115:** 103 - 111

Boyd FR, England JL (1960) Apparatus for phase equilibrium measurements at pressures up to 50 kbars and temperatures to 1750°C. J Geophys Res **65:** 741 - 748.

Buhlmann AL, Cavell P, Burwash RA, Creaser RA, Luth RW (2000) Minette bodies and cognate mica-clinopyroxenite xenoliths from the Milk River area, southern Alberta: records of a complex history of the northernmost part of the Archean Wyoming craton. Can J Earth Sci **37:** 1629 - 1650

Carlson RW, Nowell GM (2001) Olivine-poor sources for mantle-derived magmas: Os and Hf isotopic evidence from potassic magmas of the Colorado Plateau. Geochem Geophys Geosyst **2:** 2000GC000128

Chapman DS, Pollack HN (1977) Regional geotherms and lithospheric thickness. Geology **5:** 265 - 268

Conticelli S, Peccerillo A (1992) Petrology and geochemistry of potassic and ultrapotassic volcanism in central Italy: Petrogenesis and inferences on the evolution of mantle sources. Lithos, **28:** 221 - 240

Currie CA, Beaumont C (2011) Are diamond-bearing Cretaceous kimberlites related to low-angle subduction beneath western North America? Earth Planet Sci Lett **303:** 59 - 70

Edgar AD, Condliffe E (1978) Derivation of K-rich ultramafic magmas from a peridotitic mantle source. Nature, **275:** 639 - 640

Edgar AD, Green DH, Hibberson WO (1976) Experimental petrology of a highly potassic magma. J Petrol **17:** 339 - 356

Edgar AD, Condliffe E, Barnett RL, Shirran GJ (1980) An experimental study of an olivine ugandite magma and mechanisms for the formation of its K-enriched derivatives. J Petrol **21:** 475 - 497

Elkins-Tanton LT, Grove TL (2003) Evidence for deep melting of hydrous metasomatized mantle: Pliocene high-potassium magmas from the Sierra Nevadas. J Geophys Res **108:** 1 - 19

Esperanca S, Holloway JR (1987) On the origin of some mica-lamprophyres: experimental evidence from a mafic minette. Contrib Mineral Petrol **95:** 207 - 216

Foley SF (1992a) Petrological characterization of the source components of potassic magmas: Geochemical and experimental constraints. Lithos, **28:** 187 - 204

Foley SF (1992b) Vein-plus-wall-rock melting mechanisms in the lithosphere and the origin of potassic alkaline magmas. Lithos, **28:** 435 - 453

Foley SF (1993) An experimental study of olivine lamproite: First results from the diamond stability field. Geochim Cosmochim Acta **57:** 483 - 489

Foley SF, Musselwhite DS, Van Der Laan SR (1999) Melt compositions from ultramafic vein assemblages in the lithospheric mantle: a comparison of cratonic and non-cratonic settings. In: The JB Dawson volume, Proceedings of the VIIth International Kimberlite Conference **1:** 238 - 246

Gee LL, Sack RO (1988) Experimental petrology of Melilite Nephelinites. J Petrol **29:** 1233 - 1255

Ghiorso MS, Hirschmann MM, Reiners PW, Kress VC III (2002) The pMELTS: A revision of MELTS for improved calculation of phase relations and major element partitioning related to partial melting of the mantle to 3 GPa. Geochem Geophys Geosyst **3**: 10.1029/2001GC000217

Gorman AR, Clowes RM, Ellis RM, Henstock TJ, Spence GD, Randy Keller G, Levander A, Snelson CM, Burianyk MJA, Kanasewich ER, Asudeh I, Hajnal Z, Miller KC (2002) Deep Probe: imaging the roots of western North America. Can J Earth Sci **39:** 375 - 398

Herzberg C, O'Hara MJ (2002) Plume-associated ultramafic magmas off Phanerozoic age. J Petrol **43:** 1857 - 1883

Humphreys E (2009) Relation of flat subduction to magmatism and deformation in the western United States. The Geological Society of America, memoir 204

Ionov DA, Griffin WL, O'Reilly SY (1997) Volatile-bearing minerals and lithophile trace elements in the upper mantle. Chem Geol **141:** 153 - 184

Lemieux S, Ross GM, Cook FA (2000) Crustal geometry and tectonic evolution of the Archean crystalline basement beneath the southern Alberta Plains, from new seismic reflection and potential-field studies. Can J Earth Sci **37:** 1473 - 1491

Lloyd FE, Bailey DK (1975) Light element metasomatism of the continental mantle: evidence and the consequences. Phys Chem Earth **9:** 389 - 415

Lloyd FE, Arima M, Edgar AD (1985) Partial melting of a phlogopite-clinopyroxenite nodule from south-west Uganda: an experimental study bearing on the origin of highly potassic continental rift volcanics. Contrib Mineral Petrol **91:** 321 - 329

Macdonald R, Upton BGJ, Collerson KD, Hearn Jr BC, James D (1992) Potassic mafic lavas of the Bearpaw Mountains, Montana: mineralogy, chemistry, and origin. J Petrol **33:** 305 - 346

Menzies MA (1983) Mantle ultramafic xenoliths in alkaline magmas: evidence for mantle heterogeneity modified by magmatic activity. In: CJ Hawkesworth and MJ Norry (eds) Continental Basalts and Mantle Xenoliths. Shiva, Mantwich, pp. 92 - 110

Mitchell RH (1995) Melting experiments on a sanidine phlogopite lamproite at 4 - 7 GPa and their bearing on the sources of lamproite magma. J Petrol **36:** 1455 - 1474

Navon O, Stolper E (1987) Geochemical consequences of melt percolation: the upper mantle as a chromatographic column. J Geol **95:** 285 - 307

Nicholls IA, Whitford DJ (1983) Potassium-rich volcanic rocks of the Muriah complex, Java, Indonesia: Products of multiple magma sources? J Volcanol Geotherm Res **18:** 337 - 359

O'Brien HE, Irving AJ, McCallum IS (1991) Eocene potassic magmatism in the Highwood Mountains, Montana: petrology, geochemistry and tectonic implications. J Geophys Res **96:** 13237 - 13260

O'Brien HE, Irving AJ, McCallum IS, Thirlwall MF (1995) Strontium, neodymium, and lead isotopic evidence for the interaction of post-subduction asthenospheric potassic mafic magmas of the Highwood Mountains, Montana, USA, with ancient Wyoming craton lithospheric mantle. Geochim Cosmochim Acta **59:** 4539 - 4556

Orejana D, Villaseca C, Billstrom K, Paterson BA (2008) Petrogenesis of Permian alkaline lamprophyres and diabases from the Spanish Central System and their geodynamic context within western Europe. Contrib Mineral Petrol **156:** 477 - 500

Parat F, Holtz F, Rene M, Almeev R (2010) Experimental constraints on ultrapotassic magmatism from the Bohemian Massif (durbachite series, Czech Republic) Contrib Mineral Petrol **159:** 331 - 347

Pearson DG, Canil D, Shirey SB (2004) Mantle samples included in volcanic rocks: xenoliths and diamonds. In: Carlson RW (ed) Treatise on Geochemistry. Volume 2: The Mantle and Core, Elsevier-Pergamon, Oxford, pp 171 - 275

Putirka K (2008) Thermometers and Barometers for Volcanic Systems. In: Putirka K and Tepley F (eds) Rev Mineral Geochem, vol 69, pp 61 - 120

Putirka K, Perfit M, Ryerson FJ, Jackson MG (2007) Ambient and excess mantle temperatures, olivine thermometry, and active vs. passive upwelling. Chem Geol **241:** 177 - 206

Righter K, Carmichael ISE (1996) Phase equilibria of phlogopite lamprophyres from western Mexico: Biotite-liquid equilibria and P-T estimates for biotite-bearing igneous rocks. Contrib Mineral Petrol **123:** 1 - 21

Roeder PL, Emslie RF (1970) Olivine-liquid equilibrium. Contrib Mineral Petrol **29:** 275 - 289

Rosenthal A, Foley SF, Pearson DG, Nowell GM, Tappe S (2009) Petrogenesis of strongly alkaline primitive volcanic rocks at the propagating tip of the western branch of the East African Rift. Earth Planet Sci Lett **284:** 236 - 248

Sack RO, Walker D, Carmichael ISE (1987) Experimental petrology of alkalic lavas: constrains on cotectics of multiple saturation in natural basic liquids. Contrib Mineral Petrol **96:** 1 - 23

Sato K (1997) Melting experiments on a synthetic olivine lamproite composition up to 8 GPa: Implications to its petrogenesis. J Geophys Res **102:** 14,751 - 14,764

Schmandt B, Humphyreys E (2010) Complex subduction and small-scale convection revealed by body-wave tomography of the western United States upper mantle. Earth Planet Sci Lett **297:** 435 - 445

Snyder DA, Carmichael ISE (1992) Olivine-liquid equilibria and the chemical activities of FeO, NiO, Fe_2O_3 and MgO in natural basic melts. Geochim Cosmochim Acta **56:** 303 - 318

Sparks RSJ, Pinkerton H, MacDonald R (1977) The transport of xenoliths in magmas. Earth Planet Sci Lett **35:** 234 - 238

Spera FJ (1984) Carbon dioxide in petrogenesis III: role of volatiles in the ascent of alkaline magma with special reference to xenolith-bearing mafic lavas. Contrib Mineral Petrol **88:** 217 - 232

Tappe S, Foley SF, Kjarsgaard BA, Romer RL, Heaman LM, Stracke A, Jenner GA (2008) Between carbonatite and lamproite - Diamondiferous Torngat ultramafic lamprophyres formed by carbonate-fluxed melting of cratonic MARID-type metasomes. Geochim Cosmochim Acta **72:** 3258 - 3286

Wallace P, Carmichael ISE (1989) Minette lavas and associated leucitites from the Western Front of the Mexican Volcanic Belt: petrology, chemistry and origin. Contrib Mineral Petrol **103:** 470 - 492

Yuan H, Romanowicz B (2010) Lithospheric layering in the North American craton. Nature **466:** 1063 - 1068

Chapter 3: Melting phase relations of a mica-clinopyroxenite from the Milk River area, southern Alberta, Canada

3.1. Introduction:

In southern Alberta, Canada, minettes crop out as dykes near the Milk River. Carried in these dykes are coarse-grained xenoliths composed of clinopyroxene, phlogopite, and apatite. Both the minettes and xenoliths were studied by Buhlmann et al. (2000). Based on the experimental study of Esperanca and Holloway (1987) and an extrapolation of phase boundaries inferred by Wallace and Carmichael (1989), Buhlmann et al. postulated that the minettes formed by partial melting of a source containing clinopyroxene, phlogopite and possibly olivine, at pressures $\geq$ 1.7 GPa. Funk and Luth (ms. submitted) conducted liquidus experiments on the most primitive minette from Buhlmann et al.'s study, and found that olivine and orthopyroxene coexisted with a liquid at 1.77 GPa and 1350°C. Neither clinopyroxene nor phlogopite were found to be liquidus phases, so the multiple saturation point found by Funk and Luth is not consistent with Buhlmann et al.'s hypothesis. Funk and Luth suggested that the primary minette magma re-equilibrated with harzburgite during ascent rather than harzburgite representing the source region, given that a harzburgite would lack sufficient K and Ca to be a realistic lithology to form the minette by partial melting.

The purposes of investigating the melting behaviour of the mica-clinopyroxenite xenolith were: first, to ascertain the phase relations of this mica-clinopyroxenite; second, to characterize the compositions of the hydrous, mafic, alkali-rich melts produced; and third, to assess the viability of such lithologies as sources for the minettes found at Milk River, and similar mafic alkali-rich magmas.

3.2. Starting Material:

Several mica-clinopyroxenite xenoliths were analyzed by Buhlmann et al. (2000). To select one to study for our experiments, we chose a xenolith with pyroxene Mg#'s (molar Mg/(Mg + Fe*)) that overlap those thought to be realistic for the subcontinental lithospheric mantle. This criterion led us to select the xenolith with the highest MgO content, which should have the highest solidus temperatures, and hence provide one endmember of possible behaviours. Based on this, sample DAT4-5 was selected. For our experiments, we used an aliquot of the natural rock powder prepared by Buhlmann for his original study (major-element composition is given in **Table 3.1**).

3.3. Methodology:

Approximately 3 mg of powdered sample was packed tightly in a graphite capsule with dimensions ~4 mm tall, ~2.65 mm outer diameter (OD), and ~1.2 mm inner diameter (ID). The graphite capsule was loaded into a 3 mm OD Pt capsule. No additional water was added to the sample. The capsule was placed in a 120°C oven overnight to dry prior to sealing by arc-welding. The capsules were run vertically in 12.7 mm talc-pyrex assemblies in solid-media, piston-cylinder apparatus (Boyd and England 1960) at the C.M. Scarfe Laboratory of Experimental Petrology, University of Alberta. The pressures were calibrated on the quartz-coesite transition at 1000°C, and on the jadeite-albite-quartz transition at 600 and 1000°C. It was determined that a -13% correction was required to correct the nominal pressures. Temperatures were monitored with W95Re5-W74Re26 thermocouples with no corrections made for the effect of pressure on the emf of the thermocouple.

Experiments were run at 1.33, 1.77, and 2.21 GPa, at temperatures between 900 and 1350°C (**Table 3.2**). Each experiment was brought up to ~80% pressure, heated to the desired temperature, and then the pressure was increased to the appropriate value. The duration of experiments was 1-6 days, depending on temperature. Due to the difficulty of establishing equilibrium at 1.33 GPa and 1200°C, it was run in a two-step approach. The sample was heated to 1600°C for 5 hrs, then brought down at a rate of ~400°C/min to 1200°C and allowed to equilibrate for several days.

The compositions of the run products were measured with the JEOL 8900R electron microprobe at the Department of Earth and Atmospheric Sciences, University of Alberta. All experiments were analyzed at a 15 kV accelerating voltage. For mineral grains, a beam current of 15 nA was used with a beam diameter of 1-3 μm. For glasses, the beam current was reduced to 10 nA and the beam diameter widened to 10 μm to lessen damage on the hydrous glasses. To lessen the effect of alkali migration during glass analyses, potassium and sodium were analysed first. For all analyses, counting times were 20 seconds on peak, and 10 seconds on the background. Natural mineral standards were used (**Table 3.3**). The compositions of the phases were used to calculate the modal percentages by mass balance (**Table 3.2**).

3.4. Results:

3.4.1. Phase Relationships and Melting Reactions:

The sub-solidus mineralogy is clinopyroxene, phlogopite and trace amounts of apatite (**Figure 3.1**). It was difficult to determine the location of the solidus precisely because small volumes of melt were difficult to observe in back-scatter electron images on the electron microprobe. With increasing temperature, however, olivine appears and apatite disappears, and

no other phosphorous-bearing mineral is observed. We infer this disappearance marks the position of the solidus, with a solidus reaction of:

$$\text{phl} + \text{cpx} + \text{ap} \rightarrow \text{ol} + \text{melt} \qquad (1)$$

Apatite present in trace amounts would be consumed rapidly in melting reaction (1), allowing us to define the location of the solidus by the disappearance of apatite. The solidus is relatively steep in PT-space (**Figure 3.1**). At 1.33 GPa, the solidus is bracketed between 1050°C and 1100°C, and it is bracketed at both 1.77 and 2.21 GPa between 1100°C and 1150°C. Just above the inferred solidus, a few experiments contain only clinopyroxene and phlogopite. We were unable to analyze or image the melt, and did not observe olivine in these capsules. At higher temperatures, olivine and liquid were found to coexist with clinopyroxene and phlogopite, but we were unable to determine the composition of the melt in these experiments. Olivine has been observed as the product of melting phlogopite (Yoder and Kushiro 1969) and phlogopite + diopside (Modreski and Boettcher 1973). Therefore, the observed olivine-in reaction boundary may be taken as an upper bound of the solidus.

Phlogopite disappears by ~50°C above the solidus at 1.33 GPa, and ~100°C above the solidus at 2.21 GPa by reaction (1), leaving only clinopyroxene, olivine and liquid. The modal abundances of both olivine and clinopyroxene decreases with increasing temperature (**Table 3.2**). Therefore, once phlogopite disappears, the melting reaction becomes:

$$\text{cpx} + \text{ol} \rightarrow \text{melt} \qquad (2)$$

3.4.2. Melt Composition:

Liquids quenched to glass with little or no quench phlogopite present. Where quench phlogopite is present, it is restricted to needle-like crystals at mineral-melt interfaces. Low-degree partial melts (<30%) were challenging because they do not form melt pockets large enough to analyze with the electron microprobe. Therefore, we have few constraints on the composition of our near-solidus melts.

Where the melt pockets were of sufficient size to analyze, the coexisting mineral assemblage is clinopyroxene and olivine. The melt compositions are silica-undersaturated, mafic, alkali- and volatile-rich (**Table 3.4**). Glasses are metaluminous (molar $Al_2O_3 < (Na_2O + K_2O + CaO)$) and near the metaluminous-peralkaline boundary ($Al_2O_3 \approx (Na_2O + K_2O)$). The Mg# of our glasses range from 68.0 to 81.6 (**Table 3.4**). Fluorine and chlorine concentrations are between 0.67-1.08 wt% and ~0.04 wt%, respectively (**Table 3.4**). Based on the low totals, we infer that our glasses have ~4-9 wt% dissolved H_2O (**Table 3.4**).

Liquids in equilibrium with clinopyroxene and olivine show systematic trends with respect to temperature (**Table 3.4** and **Figures 3.2a-h**) and pressure (**Table 3.4**). With increasing temperature, SiO_2, MgO and CaO concentrations increase in the melt (**Table 3.4** and **Figures 3.2a, b**). Elements found almost exclusively in phlogopite and apatite, such as TiO_2, Al_2O_3, Na_2O, K_2O, P_2O_5 and F, decrease with increasing temperature due to dilution (**Figures 3.2c-h**). With increasing pressure, the concentrations of SiO_2, MgO and CaO decrease in the melt, whereas the concentrations of the other oxides increase (**Table 3.4**).

At lower temperatures, the scatter in the glass compositions tend to be larger than those at higher temperatures. This scatter may result from either compositional heterogeneities in the

glass itself, or overlap of the beam with adjacent minerals, which would be more problematic at low melt fractions.

3.4.3. Clinopyroxene Composition:

Clinopyroxene grains are typically subhedral to anhedral, and are ~30 μm in diameter in sub- and near-solidus experiments, but are >100 μm in experiments with large volumes of melt. The modal abundance of clinopyroxene is constant below the solidus (~60%), and progressively decreases with increasing temperature above the solidus.

With increasing temperature, Mg content in clinopyroxene increases and Ca decreases (**Table 3.5**). We saw no significant pressure dependence on the Mg-Ca exchange reaction within the investigated pressure range. Mg# increases with increasing temperature, and decreases with increasing pressure. Some Ti and Al are incorporated into the clinopyroxene crystal structure (**Table 3.5**). At 1.33 GPa, we observed that Ti and Al contents remain constant below the solidus, but once phlogopite disappears, the concentrations peak and then progressively decrease with increasing temperature (**Table 3.5**). We interpret this trend to result from dissolution of phlogopite into melt, which would increase the TiO_2 and Al_2O_3 activity in the melt, thereby increasing Ti and Al in clinopyroxene. As melting continues beyond phlogopite stability, these elements become more dilute in the liquid (**Table 3.4**), thereby decreasing their activity in the melt. At temperatures above the phlogopite stability field, TiO_2 and Al_2O_3 become less compatible in clinopyroxene with increasing temperature (**Figures 3.3a, b**). This effect is subdued at higher pressures. The concentrations of MnO and Na_2O in clinopyroxene decrease as temperature increases, and increase as pressure increases (**Table 3.5**). At lower temperatures,

MnO is compatible in clinopyroxene, and progressively becomes less compatible with increasing temperature (**Figure 3.3c**).

3.4.4. Phlogopite Composition:

Phlogopite crystals are typically elongate and are ~100 μm in length. In sub-solidus experiments, the modal abundance of phlogopite remains constant (~40%), but decreases sharply with increasing temperature above the solidus.

Relative to the endmember phlogopite chemical formula [$K_2Mg_6(Al_2Si_6O_{20})(OH)_4$], these micas are silica-deficient and alumina-rich, with Si between ~5.73-5.83 and Al between ~2.25-2.52 cations per 22 oxygens (**Table 3.6**). The Mg# of phlogopite increases with temperature, and decreases with increasing pressure. A small amount of sodium substitutes for potassium in the interlayer cation sites, but there are vacancies (Na + K < 2; **Table 3.6**). With increasing temperature, sodium content decreases, consistent with sodium behaving incompatibly in phlogopite (Carman 1974). At temperatures above the solidus, the concentrations of Ti and F in phlogopite are higher than those in sub-solidus experiments (**Table 3.6**). This observation is consistent with many studies that have shown that F (Foley et al. 1986a; Edgar and Charbonneau 1991; Vukadinovic and Edgar 1993; Edgar and Pizzolato 1995; Melzer and Foley 2000) and Ti (Tronnes et al. 1985; Patino Douce 1993) increase the stability of phlogopite to higher temperatures. At higher pressures, the increase in Ti in phlogopite is subdued. Chlorine is present in trace amounts in sub-solidus phlogopite, but drops below the detection limits above the solidus (**Table 3.6**).

3.4.5. Apatite Composition:

Apatite appears only in sub-solidus experiments. They are generally angular and anhedral. The apatite grains are small, typically <10 μm in length. The modal abundances are low, usually ~1% of the sample.

The apatite in our system is fluorine-rich (~1.70 wt% F; **Table 3.7**). Small concentrations of chlorine were observed as well. Relative to the idealized apatite chemical formula [$Ca_5P_3O_{12}$(OH, Cl, F)] our apatites are deficient in Ca (~4.7) and P (~2.85) (**Table 3.7**). All of our apatites contain measureable amounts of SiO_2 (~0.4 wt%), FeO* (~0.5 wt%) and MgO (~0.5 wt%) (**Table 3.7**). It is possible that Fe, Mn, Mg, Na or K could substitute for Ca, whereas P is exchanged for Si. However, due to the difficulty of analyzing small grains, the presence of these oxides may be the result of overlap of the beam with adjacent minerals.

3.4.6. Olivine Composition:

Olivine forms during melting, and is not present in sub-solidus experiments. Olivine grains are generally rounded and are anhedral to subhedral. At lower temperatures, olivine grains are only ~10 μm in diameter, increasing to >200 μm in high-temperature experiments. The modal abundance of olivine initially increases with increasing temperature (maximum olivine modal percentage ~17%), but it decreases with increasing temperature after phlogopite disappears.

Olivine is stoichiometric, and does not contain measureable amounts of Ti, Al, Na, or K (**Table 3.8**). The Mg# of olivine increases with increasing temperature and decreases with increasing pressure. The CaO content in olivine is consistently between 0.3-0.5 wt%, and has no obvious temperature or pressure dependence (**Table 3.8**). Manganese behaves compatibly at

lower temperatures, but becomes less compatible with increasing temperature (**Figure 3.4**), as found previously by Snyder and Carmichael (1992).

3.4.7. Mineral-liquid Equilibria:

Determining if our experiments were in equilibrium is crucial for the interpretation of our results. Roeder and Emslie (1970) found that the exchange coefficient for Fe-Mg between olivine and liquid, $K_D(Fe\text{-}Mg)^{ol\text{-}liq}$, is 0.30±0.03, independent of melt composition and temperature. Subsequent studies on alkali-rich magmas found that the olivine-liquid exchange coefficient depends on the liquid composition (Sack et al. 1987; Gee and Sack 1988). Gee and Sack (1988) found that $K_D(Fe\text{-}Mg)^{ol\text{-}liq}$ decreases with decreasing silica and increasing alkali contents. Tholeiitic to alkali basalts have exchange coefficients ranging from 0.33 to 0.27; at lower silica activities, olivine melilitites to nephelinites have exchange coefficients ranging from 0.25 to 0.17.

An analogous mineral-melt Fe-Mg exchange coefficient can be calculated for clinopyroxene. Putirka (2008) noted that there is a shortcoming in using only Fe-Mg exchange reactions to evaluate equilibrium because they do not measure the extent of Na-Al and Ca-Na exchange. However, Putirka noted that deviations in calculated exchange coefficients are correlated to differences in diopside-hedenbergite, so a simple Fe-Mg exchange may be sufficient to test for equilibrium. A $K_D(Fe\text{-}Mg)^{cpx\text{-}liq}$ of 0.28±0.08 was found to indicate equilibrium (Putirka 2008).

The mineral-liquid Fe-Mg exchange coefficients (**Table 3.9**) calculated for our experiments are in the same range as those reported by Roeder and Emslie (1970), Gee and Sack

(1988) and Putirka (2008), which suggests that our experiments achieved Fe-Mg exchange equilibrium. This conclusion is consistent with the observed homogeneity of the mineral grains.

3.4.8. Geothermobarometry:

As a second independent test for equilibrium, temperatures and pressures were calculated using a range of glass-only and mineral-liquid geothermometers and a mineral-liquid geobarometer. Putirka et al. (2007) and Putirka (2008) have a detailed explanation of the empirical fitting, statistics, sample calculations, and review of the glass-only and mineral-liquid geothermometers and geobarometers used in this study.

The glass-only geothermometer, equation 15 from Putirka (2008), was used to calculate temperatures of experiments with appreciable quantities of liquid present. Equation 15 is applicable for any liquid saturated with olivine. The range of pressures, temperatures, and compositions of experimental glasses used in the calibration of this expression makes it appropriate for our system. The uncertainty for temperatures calculated with equation 15 is ±60°C (Putirka 2008). Within the uncertainty, equation 15 reproduces temperatures of our experiments accurately (**Table 3.10**).

In the same experiments with large volumes of glass, the olivine-liquid thermometer of Putirka et al. (2007; their equations 2 and 4), was also used to calculate temperatures. Putirka et al. reported an uncertainty of ±52°C for their expression. When these equations are coupled, the calculated temperatures for our mafic alkali-rich system are systematically lower by ~20 - 40°C than the measured temperatures of the experiments (**Table 3.10**). They do agree, however, within the stated uncertainty.

Along with the above thermometers, a clinopyroxene-liquid geothermometer and geobarometer were utilized (**Table 3.10**). Putirka et al. (1996), Putirka (1999) and Putirka et al. (2003) developed several clinopyroxene-liquid barometers and thermometers, using a variety of experimental data from several pressures and temperatures to calibrate their equations. The geobarometer, equation 31 from Putirka (2008), was chosen because the equation was empirically fitted with data excluding 1 atm and $P \geq 4.0$ GPa experiments, but still accounted for the presence of alkalis and water in the glass. The geothermometer, equation 33 from Putirka (2008), was chosen because the equation accounts for the effect of water and alkalis in the melt on temperature, within an uncertainty of ±60°C. Within the geobarometer's uncertainty of ±0.29 GPa (Putirka 2008), this equation reproduced our experimental run pressures well (**Table 3.10**). The calculated temperatures for our experiments fell within the range of uncertainty of equation 33.

The results of these geothermometers and geobarometers, along with mineral-liquid Fe-Mg exchange coefficients, and the observed homogeneity of the mineral grains, are consistent with equilibrium being achieved in our system.

3.4.9. Iron Loss:

The loss of iron by alloying with the outer Pt capsule was a concern for our experiments. To mitigate this problem, we enclosed our sample in a graphite capsule, as has been done in previous experimental studies. Nevertheless, we detected iron when analysing the Pt capsule on the electron microprobe. Assessing the exact magnitude of iron loss is difficult. Using the modal abundances for each phase (given in **Table 3.2**), assuming all Fe-bearing phases were analysed, we reconstructed the bulk composition of our experiments. A comparison of the reconstructed

composition with the original starting material yields an estimate on the percentage of iron loss (general expression given in **Table 3.11**). Using the same methodology, we also estimated the percentage of iron loss in other experimental papers (Barton and Hamilton 1979; Lloyd et al. 1985; Esperanca and Holloway 1987; Sweeney et al. 1993; Righter and Carmichael 1996; Holbig and Grove 2008) with similar compositions and capsule designs. We obtain a range for iron loss for our experiments that is similar to those estimated by the previous authors (~1-20%), lending credence to our calculations.

The calculations show that our experiments had ~7-25% iron loss (**Table 3.11**). Sweeney et al. (1993) argued that ~14-18% iron loss is not significant enough to affect phase relations or the relative appearance of phases. However, we have three experiments with > 20% iron loss. To see how much the phase boundaries would shift with 25% iron loss, we used pMELTS (Ghiorso et al. 2002) to calculate ideal phase diagrams. Unfortunately, pMELTS was unable to calculate the phase diagram for DAT4-5, likely due to the presence of CO_2, F and Cl in our system. Instead, we calculated phase diagrams for a mantle peridotite (MM3) and mantle pyroxenite (G2) (**Table 3.12**). These compositions were chosen because they are well characterized in pMELTS, and are mineralogically similar to our system. The calculations from pMELTS show that a 25% loss in FeO shifts phase boundaries up by ~20-30°C in MM3 and <10°C in G2. However, the relative order of appearance of phases remains unchanged. Assuming that we can extrapolate to our composition, a phase boundary shift of 20-30°C is less than the 50°C spacing of our experiments, and is unlikely to significantly change our phase diagram.

3.5. Discussion:

3.5.1. Milk River alkali magmatism:

Buhlmann et al. (2000) hypothesized that the minettes in southern Alberta were derived from partial melting of a source containing phlogopite and clinopyroxene at pressures ≥ 1.7 GPa. This is consistent with many previous studies, both experimental (Edgar et al. 1976, 1980; Barton and Hamilton 1978, 1979; Edgar and Condliffe 1978; Nicholls and Whitford 1983; Lloyd et al. 1985; Esperanca and Holloway 1987; Mitchell 1995; Righter and Carmichael 1996; Sato 1997; Elkins-Tanton and Grove 2003) and geochemical (Lloyd and Bailey 1975; Van Kooten 1980; Wallace and Carmichael 1989; Conticelli and Peccerillo 1992; Foley 1992a, 1992b; Macdonald et al. 1992; Carlier and Lorand 1997; Carlson and Nowell 2001), on related mafic alkali-rich rocks. Buhlmann et al. (2000) predicted that if liquidus experiments were performed on the most primitive minette, a multiple saturation point where clinopyroxene, phlogopite and possibly olivine would co-crystallize at pressures ≥ 1.7 GPa.

Funk and Luth (ms. submitted) conducted liquidus experiments on the most primitive minette from Milk River (RAB90 Au24-1; see Buhlmann et al. 2000 for composition), and found a multiple saturation point at 1.77 GPa and 1350°C, where olivine and orthopyroxene coexisted with a liquid. Neither clinopyroxene nor phlogopite were liquidus phases. This multiple saturation point is inconsistent with Buhlmann et al.'s hypothesis. Funk and Luth argued that the high concentrations of CaO and K_2O of the minette is still best explained by the partial melting of a mica-clinopyroxenite. Based on the work of Navon and Stolper (1987) and Foley (1992b), they proposed that the primary minette magma had re-equilibrated with a harzburgite wall-rock

during ascent. The dissolution of wall-rock minerals, proposed by Foley (1992b), is believed to be the dominant mechanism for re-equilibration for the Milk River minettes.

To determine the mineralogy of the source region of the RAB90 Au24-1 minette and to test the wall-rock re-equilibration hypothesis of Funk and Luth (ms. submitted), we compared the compositions of our melts with those of the Milk River minettes. Based on the multiple saturation point found by Funk and Luth, we restricted the compositions of melts to those ≥ 1.77 GPa. The lowest-degree partial melts from 1.77 GPa (52X; ~37.6% at 1250°C) and 2.21 GPa (49X; ~37.1% at 1300°C) were chosen as "representative primary melts" (**Table 3.4**). We plotted our representative melts along with the RAB90 Au24-1 minette and populations of mantle orthopyroxene and olivine (representative plots for SPF52X melts shown; **Figures 3.5a-f**).

Because our primary melts are in equilibrium with olivine, we would not expect to see a reaction trend toward the mantle olivine population. From Funk and Luth (ms. submitted), orthopyroxene is the other phase that could plausibly interact with our primary melt. Therefore, we explored a binary mixing model to our system (shown as a black arrow in **Figures 3.5a-f**), assuming that the primary (experimental) liquid is only dissolving orthopyroxene. Within the uncertainty of the endmember compositions, we observed that the RAB90 Au24-1 minette lies on a linear trajectory between the 52X melt and mantle orthopyroxene (**Figures 3.5a-f**). Similar results were found for the 49X melt. Because the minette lies between our primary (experimental) melt and mantle orthopyroxene, the composition of the minette can be explained with dissolution of orthopyroxene into the original melt, consistent with the wall-rock dissolution model proposed by Foley (1992b). The Na_2O and P_2O_5 content in our primary melts is too low (0.76 wt% and 0.66 wt%, respectively, for SPF52X) to explain their concentrations in the minette (1.3 wt% and 1.02 wt%, respectively; Buhlmann et al. 2000). This compositional

discrepancy may be a result of either the high melt fraction (~37%) of the representative experimental melts, which would dilute these oxides, or the low concentrations of these oxides in the DAT4-5 starting material (e.g. low modal abundance of apatite; low Na_2O concentrations in phlogopite and clinopyroxene).

Pilet et al. (2008) investigated the effect of wall-rock mineral dissolution on the composition of hornblendite-derived partial melts at 1.5 GPa. They conducted sandwich experiments between 1225 and 1325°C, where the hornblendite vein was packed between a moderately depleted peridotite. At temperatures below the peridotite solidus, they observed that the dissolution of orthopyroxene was the main reaction between the partial melt and the surrounding peridotite, consistent with Foley (1992b) and our model above. Glasses from the sandwich experiments increased in SiO_2, Al_2O_3 and MgO, and decreased in TiO_2, FeO*, CaO, Na_2O and K_2O as dissolution progressed (Pilet et al. 2008). Albeit a different compositional system, Pilet et al.'s observations are consistent with our analysis for the Milk River minettes (**Figures 3.5a-f**).

We conclude that, within the constraints of Buhlmann et al. (2000) and Funk and Luth (ms. submitted), the RAB90 Au24-1 minette could be derived from a mica-clinopyroxenite source at pressures ≥ 1.7 GPa, but re-equilibrated with mantle orthopyroxene via dissolution.

3.5.2. Global alkali magmatism:

The melting of vein assemblages has been invoked to explain the origin of many alkaline rocks (e.g. Italy: Conticelli et al. 2009; Boari et al. 2009; Nikogosian and van Bergen 2010; Tibet: Jiang et al. 2006). Unfortunately, there have been few experimental studies on the melting

behaviour of realistic vein compositions. In the FeO*- and P_2O_5-free KCMAS-H_2O system, Modreski and Boettcher (1973) observed the peritectic melting reaction:

$$\text{phlogopite} + \text{diopside} \rightarrow \text{forsterite} + \text{melt} \qquad (3)$$

at ~1175°C, ~1200°C and ~1275°C at 1.5 GPa, 2.0 GPa and 2.5 GPa, respectively. Their melting reaction is similar to the solidus reaction observed in our study. Compared to our system, the addition of iron and sodium in clinopyroxene and phlogopite should shift melting reaction (3) to lower temperatures, whereas fluorine and titanium in phlogopite may shift it to higher temperatures. Modreski and Boettcher (1973) also found that phlogopite, diopside, forsterite and liquid coexisted for ~75°C above the solidus at 1.5 GPa, similar to our findings.

Lloyd et al. (1985) performed melting experiments on a natural phlogopite clinopyroxenite nodule from south-west Uganda, at 2.0 and 3.0 GPa and between 1175-1300°C. The composition of the glasses are similar to K-rich lavas from the region, and they argued that these magmas were derived from source rocks similar to the phlogopite clinopyroxenite nodule. The glasses produced in our experiments are generally similar to those analyzed by Lloyd et al. (see that paper for details), but differ greatly (> 50% difference in compositions) in TiO_2, FeO*, Na_2O and P_2O_5. These deviations can be explained by differences in the accessory minerals (4% titanite, 6.5% magnetite, 0.5% jadeite in Lloyd et al.'s starting material), mineral chemistry, and modal abundances for each phase (2% apatite in Lloyd et al.'s study).

Sweeney et al. (1993) conducted melting experiments on a natural mica-amphibole-rutile-ilmenite-diopside (MARID) at 2.0-3.5 GPa and between 800 and 1450°C. They found that the "dry" (no additional water added to bulk composition) solidus was greater than a cratonic mantle geotherm (40 mW m^{-2}; Chapman and Pollack 1977), and the addition of 10 wt% H_2O

depressed the solidus by ~250°C. Sweeney et al. noted that it was unclear if water saturation was achieved, and the addition of more water could depress the solidus further. We found that the solidus for DAT4-5 is above a normal cratonic geotherm, and therefore, our mica-clinopyroxenite composition would be stable in cratonic mantle in the investigated pressure range unless the surrounding wall-rocks were heated (e.g. mantle plume) or hydrous fluids were introduced. Because our system does not contain amphibole, direct comparison of our experiments and those conducted by Sweeney et al. is difficult. The addition of water to DAT4-5 would be required in future experiments to quantify the depression of the solidus for our mica-clinopyroxenite.

Foley et al. (1999) investigated the melting behaviour of various model clinopyroxene + phlogopite + K-richterite vein assemblages at 1.5 and 5.0 GPa. They found that the addition of K-richterite to the clinopyroxene-mica assemblage reduced the solidus temperatures by ~50°C, and that amphibole was the main factor in controlling the composition of the melt. Foley et al. also found that the solidus for their vein assemblage was steep relative to the normal cratonic geotherm, and that it approaches the geotherm with increasing pressure. They argued that at pressures >5.0 GPa, minimal heating would be required to induce partial melting. This conclusion likely applies to our experiments as well. The inferred solidus for DAT4-5 is steep and intersects at 40 mW m^{-2} geotherm at ~7.5 GPa (**Figure 3.6**). To test this, higher pressure experiments would need to be performed for the purpose of comparing the solidus of DAT4-5 to a cratonic geotherm.

The high-degree partial melts produced in our study are similar to some mafic alkali-rich magmas studied by other authors (Carmichael 1967; Barton and Hamilton 1978, 1979; Holbig and Grove 2008; Prelevic et al. 2008) (**Table 3.13**). Carmichael (1967) characterized several

volcanic rocks from the Leucite Hills, Wyoming, one of which was a madupitic lamproite (**Table 3.13**). Later, Barton and Hamilton (1978, 1979) conducted a series of high-pressure experiments on this madupitic lamproite. They found that the dominant liquidus phases were clinopyroxene and olivine between 0.5-0.7 GPa, solely clinopyroxene between 0.7-1.25 GPa, clinopyroxene and spinel between 1.25-1.75 GPa, and solely clinopyroxene >1.75 GPa. Phlogopite appears ~50°C below the liquidus. Barton and Hamilton (1979) proposed that the madupitic magmas could be produced by the partial melting of an olivine-mica-pyroxenite or a mica-pyroxenite. Comparing our glasses with the madupitic lamproite, we find similarities (**Table 3.13**). Of the major and minor oxides, TiO_2 and P_2O_5 are the only oxides that are outside the given range of concentrations. This is likely a reflection of a higher titanium content in phlogopite and a slightly higher modal percentage of apatite in the source region. Therefore, we concur with Barton and Hamilton that a mica-clinopyroxenite (similar to DAT4-5) could be the protolith for the madupitic lamproites seen at Leucite Hills, Wyoming.

3.6. Summary and Conclusions:

Melting experiments were conducted on the most Mg-rich mica-clinopyroxenite xenolith from southern Alberta, Canada, near the Milk River area. These xenoliths were brought up in minette dykes (Buhlmann et al. 2000). Buhlmann et al. hypothesized that the minettes were derived from a source containing clinopyroxene + phlogopite ± olivine at pressures $\geq$ 1.7 GPa. Funk and Luth (ms. submitted) conducted liquidus experiments on the most primitive minette and found a multiple saturation point where olivine and orthopyroxene coexisted with a liquid at 1.77 GPa and 1350°C. They suggested that the primary minette magma may have been derived from a mica-clinopyroxenite source, and then re-equilibrated with a harzburgite during ascent. The goals of this study were to determine the phase relations of a mica-clinopyroxenite,

characterize the melt compositions, and test the hypotheses proposed by Buhlmann et al. (2000) and Funk and Luth (ms. submitted).

The solidus for DAT4-5 was found to be steep, and located at temperatures above a normal cratonic geotherm. Therefore, mica-clinopyroxenite lithologies in cratons are stable in the investigated pressure range, and melting must be induced by raising the temperature of the surrounding rocks, and/or by introducing hydrous fluids in order to lower the solidus. Because the solidus is steep, melting could also occur at greater depths than the pressures investigated in this study. Comparing our study with the similar study conducted by Lloyd et al. (1985), we found that the presence of accessory minerals in the starting material can change the compositional evolution of the melts with respect to either temperature or pressure. The composition of the glasses analyzed in our experiments are similar to madupitic lamproite magmas from the Leucite Hills, Wyoming craton, studied by Carmichael (1967), and Barton and Hamilton (1978, 1979). Barton and Hamilton proposed that the madupite magmas could have been derived from a source containing phlogopite + pyroxene ± olivine. The results of our study are consistent with Barton and Hamilton's hypothesis.

The composition of our lowest-degree partial melt (~37%) at 1.77 and 2.21 GPa were compared with the compositions for the RAB90 Au24-1 minette and representative populations of mantle orthopyroxene and olivine. We found that the minette lies on a linear trajectory between our experimental melt and mantle orthopyroxene. This supports Buhlmann et al.'s and Funk and Luth's hypotheses.

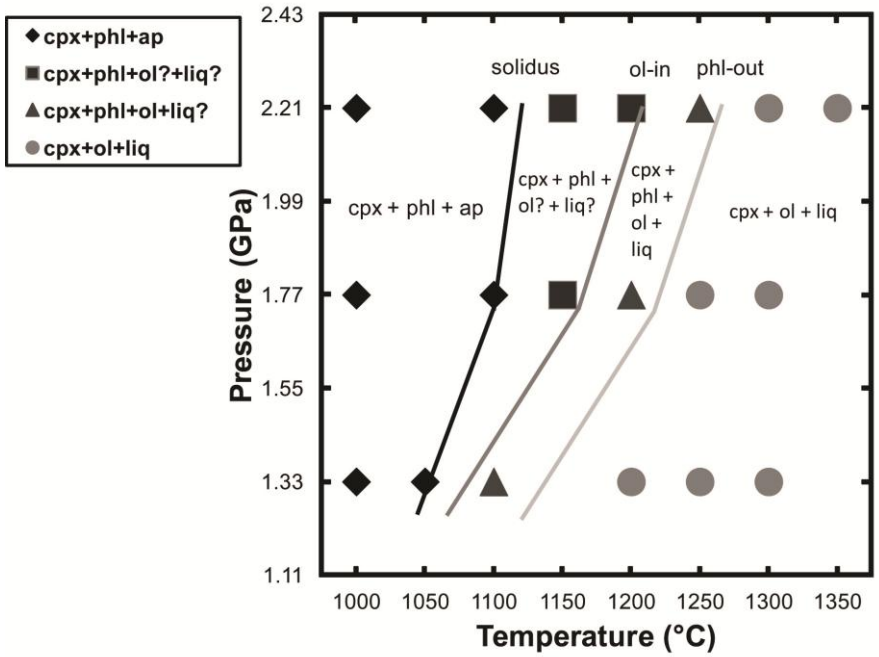

Figure 3.1: Phase relationships for DAT4-5. The black solid line marks the inferred solidus and the apatite-out reaction. The dark grey line marks the boundary where olivine is observed and is an upper bound for the solidus. The light grey solid line marks the upper limit of phlogopite stability. ol? = unobserved olivine in capsule; liq? = the liquid phase was unable to be quantified

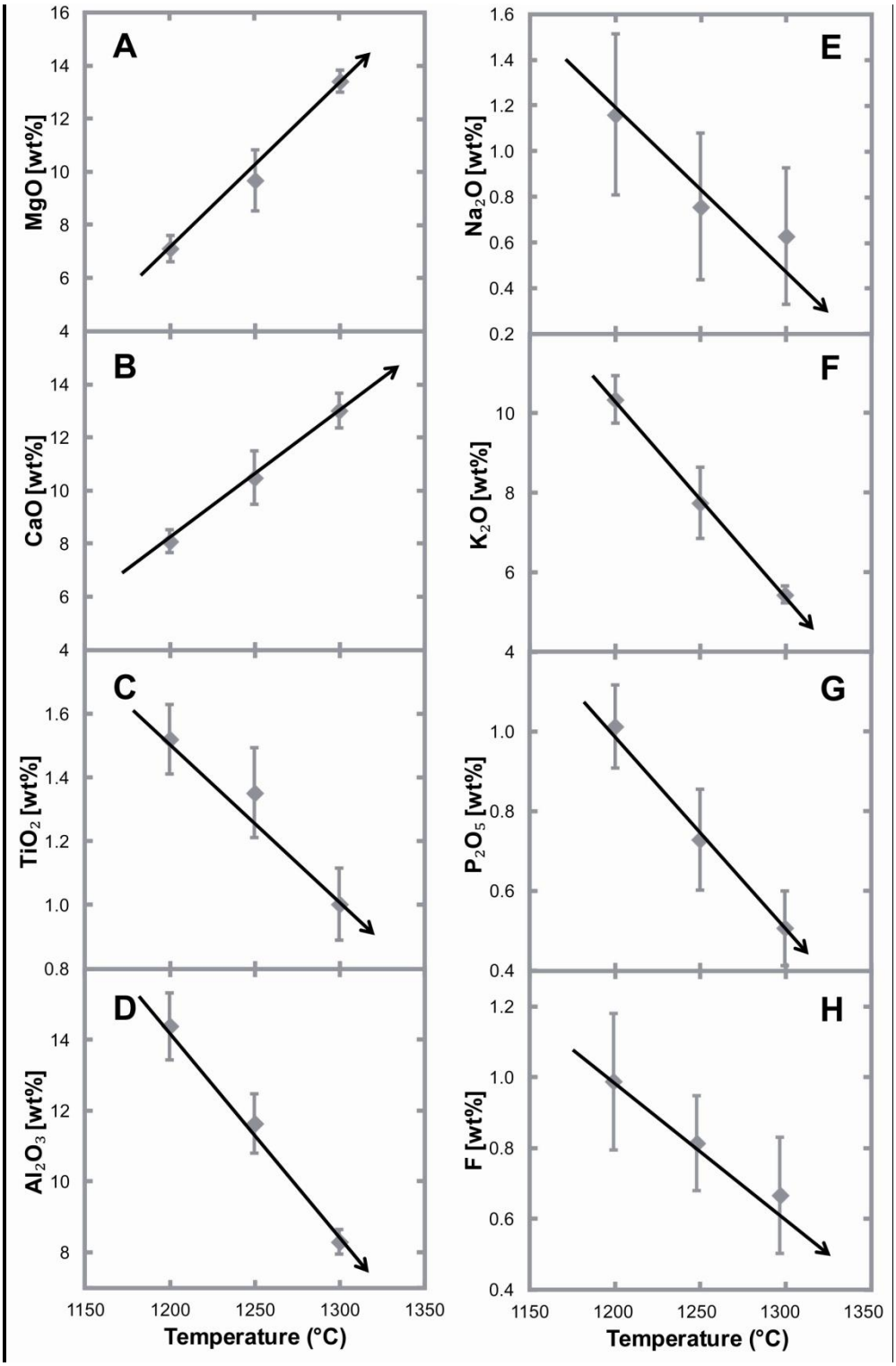

Figures 3.2a-h: Compositional evolution of melt as a function of temperature at 1.33 GPa. Black arrows show the best-fit melting trend. Errors plotted are 2σ

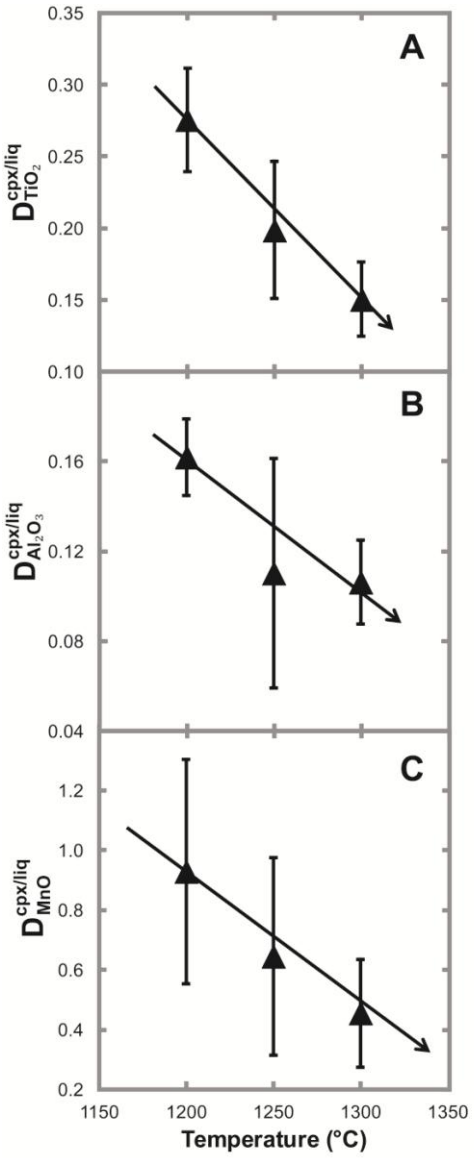

Figure 3.3a-c: Partitioning coefficients of cpx/liq for TiO_2, Al_2O_2 and MnO as a function of temperature at 1.33 GPa. Errors plotted are 2σ

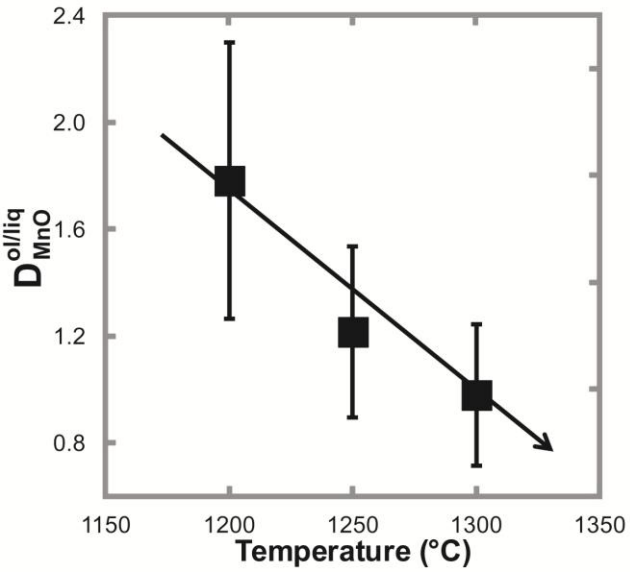

Figure 3.4: Partitioning coefficient for ol/liq for MnO as a function of temperature at 1.33 GPa.

Errors plotted are 2σ

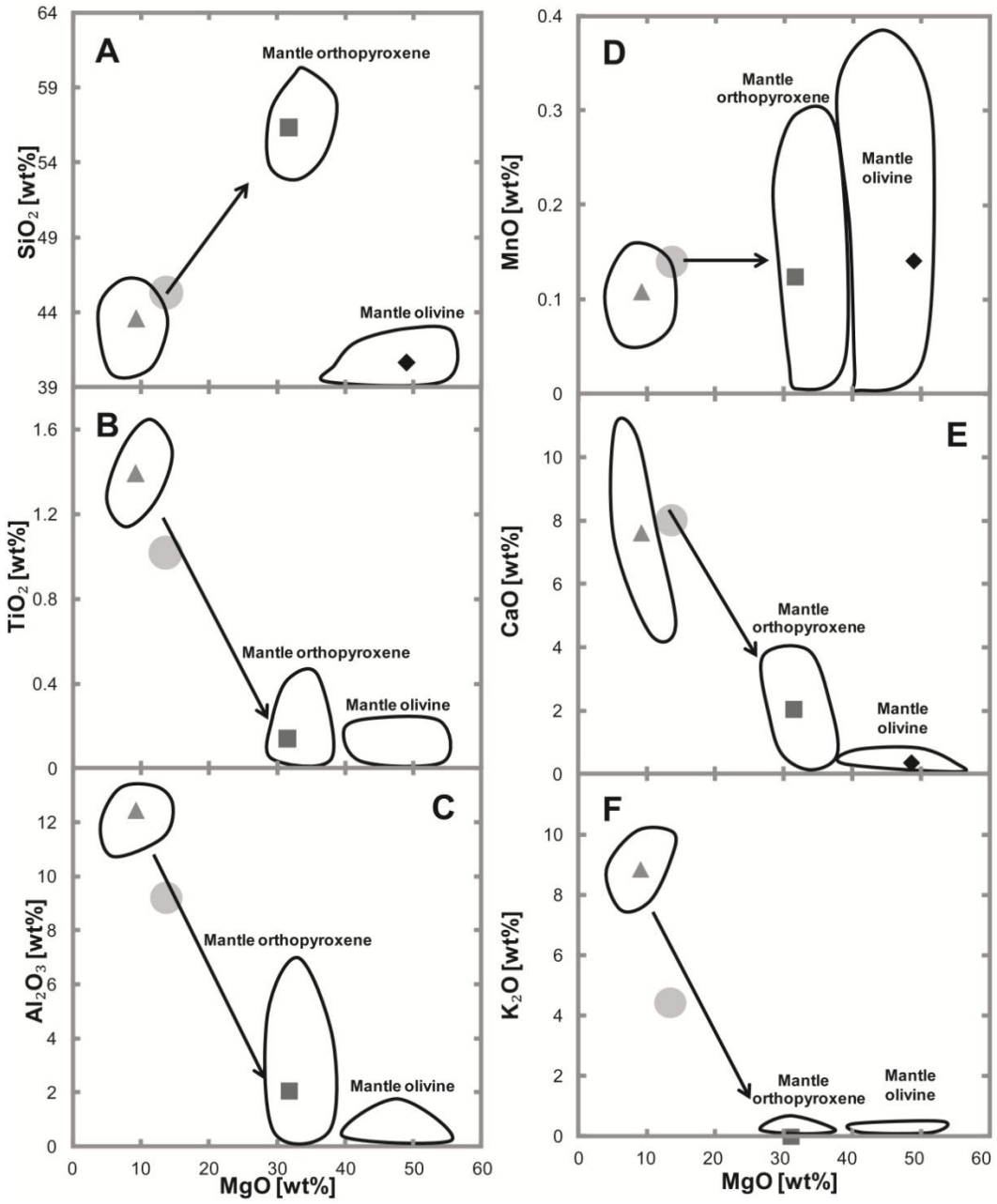

Figures 3.5a-f: Variation diagrams of SPF52X melt (dark grey triangle), RAB90 Au24-1 minette (light grey circle), and mantle orthopyroxene (dark grey square) and olivine (black diamond) compositions. Black ovals denote the compositional variation of each population. Arrows are drawn from the 52X melt population toward orthopyroxene. Oxides <d.l. for olivine not shown

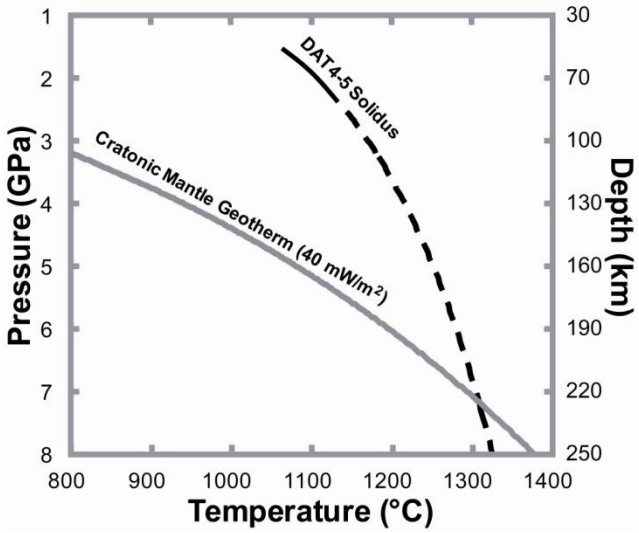

Figure 3.6: Comparison of the solidus of DAT4-5 (black curve) with a cratonic mantle geotherm (dark grey curve; Chapman and Pollack 1977). The solidus was extrapolated (black dashed curve) in accordanace to the Clapeyron equation ($dP/dT = \Delta S/\Delta V$) and constrained using the experimental study of Luth (1997). The extrapolated solidus approaches the cratonic geotherm at higher pressures. See text for discussion

Table 3.1 Composition of starting material

Sample	DAT4-5	Volatile-Free
SiO_2	47.67	48.77
TiO_2	0.72	0.74
Al_2O_3	5.48	5.61
FeO*	5.85	5.98
MnO	0.10	0.10
MgO	19.36	19.81
CaO	14.09	14.41
Na_2O	0.34	0.35
K_2O	3.74	3.83
P_2O_5	0.40	0.41
LOI	0.89	---
Total	99.3	100
Mg#	85.5	85.5

Mg# = Mg/(Mg + Fe^*); FeO* = total iron normalized to Fe^{2+}; LOI = loss on ignition

Table 3.2 Experimental run conditions

Run Name	Pressure (GPa)	Temperature (°C)	Time (hrs)	Phase relations
SPF54X	1.33	1000	70	(59.4)Cpx, (39.2)phl, (1.4)ap; $\sum R^2$ = 1.346
SPF61X	1.33	1050	70	(57.1)Cpx, (41.6)phl, (1.3)ap; $\sum R^2$ = 1.492
SPF48X	1.33	1100	70	**[49.6]**Cpx, **[7.4]**phl, **[15.3]**ol, **[27.8]liq**; $\sum R^2$ = **0.699**
SPF87XX	1.33	1600/1200	143.5	(48.3)Cpx, (16.9)ol, (34.8)liq; $\sum R^2$ = 2.946
SPF53X	1.33	1250	71	(40.7)Cpx, (16.2)ol, (43.2)liq; $\sum R^2$ = 0.478
SPF50X	1.33	1300	47	(25.5)Cpx, (11.2)ol, (63.3)liq; $\sum R^2$ = 2.521
SPF30X	1.77	900	75	(57.8)Cpx, (41.3)phl, (0.9)ap; $\sum R^2$ = 1.111
SPF29X	1.77	1000	71	(58.0)Cpx, (41.1)phl, (0.9)ap; $\sum R^2$ = 1.073
SPF32X	1.77	1100	47	(59.5)Cpx, (39.4)phl, (1.0)ap; $\sum R^2$ = 1.560
SPF34X	1.77	1150	72.5	**[53.9]**Cpx, **[17.6]**phl, **[9.7]ol, [18.8]liq**; $\sum R^2$ = **0.556**
SPF36X	1.77	1200	46.5	**[51.7]**Cpx, **[8.8]**phl, **[12.4]**ol, **[27.0]liq**; $\sum R^2$ = **0.467**
SPF52X	1.77	1250	68	(47.5)Cpx, (14.9)ol, (37.6)liq; $\sum R^2$ = 0.909
SPF91X	1.77	1300	20	(33.5)Cpx, (12.1)ol, (54.4)liq; $\sum R^2$ = 1.169
SPF47X	2.21	1000	72	(56.9)Cpx, (41.9)phl, (1.2)ap; $\sum R^2$ = 1.347
SPF72X	2.21	1100	121.5	(58.8)Cpx, (40.0)phl, (1.2)ap; $\sum R^2$ = 1.808
SPF59X	2.21	1150	70	**[53.9]**Cpx, **[13.1]**phl, **[9.9]ol, [23.1]liq**; $\sum R^2$ = **0.698**
SPF63X	2.21	1200	70	**[53.5]**Cpx, **[11.6]**phl, **[9.1]ol, [25.7]liq**; $\sum R^2$ = **0.255**
SPF51X	2.21	1250	75	**[51.7]**Cpx, **[10.3]**phl, **[10.8]**ol, **[27.2]liq**; $\sum R^2$ = **0.225**
SPF49X	2.21	1300	49	(50.3)Cpx, (12.2)ol, (37.4)liq; $\sum R^2$ = 1.697
SPF65X	2.21	1350	72.5	(43.2)Cpx, (9.6)ol, (47.3)liq; $\sum R^2$ = 2.591

Experiments at 1.33 GPa are precise to ±0.1 GPa; higher pressures are precise to ±0.05 GPa. Temperatures are precise to ±15°C. "X" denotes single-stage experiments, "XX" denotes double-stage experiments. Calculated modal abundances of mineral phases are given in parentheses (#); sum of residual squares ($\sum R^2$) given on the right. Inferred modal abundances are in square brackets **[#]**; phases inferred to exist, but with no microprobe data, are in bold. Proxy compositions for olivine and melt were used in order to calculate model abundances of those phases in experiments where they were inferred to occur. Abbreviations: cpx = clinopyroxene, phl = phlogopite, ap = apatite, ol = olivine, liq = liquid

Table 3.3 List of standards

Standard	Element
Albite	Na
Apatite	P, F
Diopside	Ca, Si
Hematite	Fe
Pyrope	Al
Rutile	Ti
Willemite	Mn
Fo93	Mg
Orthoclase	K
Tugtupite	Cl

Table 3.4 Average compositions of melt

Run SPF-	**87XX**	**53X**	**50X**	**52X**	**91X**	**49X**	**65X**
P (GPa)	1.33	1.33	1.33	1.77	1.77	2.21	2.21
T (°C)	1200	1250	1300	1250	1300	1300	1350
time (hrs)	143.5	71	47	68	20	49	72.5
n	33	47	112	21	46	30	35
SiO_2	45.4(25)	45.1(18)	46.8(17)	43.6(28)	45.6(10)	43.5(15)	44.41(96)
TiO_2	1.52 (11)	1.35(14)	1.00(11)	1.39(21)	1.13(13)	1.50(14)	1.34(10)
Al_2O_3	14.39(95)	11.64(83)	8.29(35)	12.45(91)	9.39(33)	11.51(55)	10.45(56)
FeO*	4.50(39)	6.12(42)	5.37(18)	6.95(55)	6.22(51)	6.08(31)	5.35(15)
MnO	0.09(5)	0.11(5)	0.11(5)	0.11(4)	0.11(4)	0.11(5)	0.11(5)
MgO	7.11(49)	9.7(11)	13.41(41)	9.2(28)	12.9(12)	11.0(25)	12.74(28)
CaO	8.08(43)	10.5(10)	13.01(66)	7.6(25)	11.8(13)	8.0(28)	9.74(56)
Na_2O	1.16(35)	0.76(32)	0.63(30)	0.76(26)	0.58(26)	0.67(44)	0.69(34)
K_2O	10.35(60)	7.75(89)	5.44(21)	8.86(85)	6.0(12)	8.80(97)	7.65(21)
P_2O_5	1.01(11)	0.73(13)	0.51(9)	0.66(17)	0.54(10)	0.8(2)	0.64(8)
F	0.99(19)	0.81(13)	0.67(18)	1.08(11)	0.66(14)	1.05(23)	0.75(10)
Cl	0.05(3)	0.03(3)	<d.l.	0.04(4)	<d.l.	0.04(2)	<d.l.
Mg#	73.8	73.6	81.6	73.1	78.7	76.1	80.9
Total	94.65	94.60	95.24	92.70	94.93	93.06	93.87

Standard deviations in the last digit(s) given in parentheses (2σ). n = number of analyses. <d.l. = below detection limits. Detection limits for all elements are ≤150 ppm, except for Ti (~250 ppm), Fe (~200 ppm), and F (~300 ppm). Mg# defined in **Table 1**. FeO***** = Total iron

Table 3.5 Average compositions of clinopyroxene

Run SPF-	**54X**	**61X**	**48X**	**87XX**	**53X**	**50X**
P (GPa)	1.33	1.33	1.33	1.33	1.33	1.33
T (°C)	1000	1050	1100	1200	1250	1300
time (hrs)	70	70	70	143.5	71	47
n	8	10	10	25	11	17
SiO_2	54.22(72)	54.8(13)	54.0(16)	53.23(11)	53.9(10)	54.32(67)
TiO_2	0.22(5)	0.22(5)	0.19(6)	0.42(11)	0.27(13)	0.15(5)
Al_2O_3	0.85(53)	0.76(70)	1.02(83)	2.33(47)	1.3(12)	0.93(32)
FeO*	4.48(49)	4.41(75)	4.13(65)	2.53(23)	3.0(19)	1.89(9)
MnO	0.12(7)	0.13(6)	0.12(7)	0.08(5)	0.07(7)	0.05(3)
MgO	16.53(40)	16.46(53)	16.76(73)	17.86(44)	17.7(18)	19.57(80)
CaO	22.9(17)	22.6(13)	22.8(11)	22.37(37)	22.98(95)	21.89(74)
Na_2O	0.34(20)	0.28(14)	0.28(11)	0.19(9)	0.14(14)	0.13(7)
K_2O	<d.l.	<d.l.	0.06(5)	<d.l.	0.04(4)	<d.l.
Total	99.66	99.66	99.36	99.01	99.40	98.93
On the basis of 6 oxygens						
Si	1.99(1)	2.00(2)	1.98(2)	1.95(2)	1.97(4)	1.98(2)
Ti	0.006(1)	0.006(1)	0.005(2)	0.012(3)	0.007(3)	0.004(1)
Al	0.04(2)	0.03(3)	0.04(4)	0.10(2)	0.06(5)	0.04(1)
Fe*	0.14(2)	0.13(2)	0.13(2)	0.077(7)	0.09(6)	0.057(3)
Mn	0.004(2)	0.004(2)	0.004(2)	0.003(2)	0.002(2)	0.002(1)
Mg	0.90(2)	0.90(3)	0.92(4)	0.97(3)	0.97(9)	1.06(4)
Ca	0.90(7)	0.89(5)	0.90(4)	0.87(3)	0.90(4)	0.85(2)
Na	0.02(1)	0.02(1)	0.020(8)	0.014(6)	0.01(1)	0.009(5)
K	---	---	0.003(2)	---	0.002(2)	---
Mg#	86.5	87.4	87.6	92.6	91.5	94.9

Table 3.5 ***continued*** Average compositions of clinopyroxene

Run SPF-	**30X**	**29X**	**32X**	**34X**	**36X**	**52X**	**91X**
P (GPa)	1.77	1.77	1.77	1.77	1.77	1.77	1.77
T (°C)	900	1000	1100	1150	1200	1250	1300
time (hrs)	75	71	47	72.5	46.5	68	20
n	10	10	10	10	10	8	29
SiO_2	54.1(18)	53.2(25)	53.8(22)	53.9(12)	54.2(13)	53.7(10)	54.0(9)
TiO_2	0.28(17)	0.23(10)	0.26(11)	0.22(10)	0.24(8)	0.28(5)	0.21(10)
Al_2O_3	0.8(12)	0.65(74)	1.3(21)	1.21(79)	1.5(13)	1.6(12)	1.15(59)
FeO*	4.4(16)	4.32(97)	4.47(90)	4.52(40)	3.83(50)	2.9(12)	2.9(16)
MnO	0.13(7)	0.13(6)	0.14(5)	0.14(6)	0.10(3)	0.08(4)	0.08(6)
MgO	16.6(13)	17.0(13)	16.86(77)	16.63(80)	17.4(11)	17.8(12)	18.4(16)
CaO	23.5(7)	23.50(60)	22.5(32)	22.7(18)	22.2(15)	22.6(11)	22.3(9)
Na_2O	0.31(19)	0.29(16)	0.36(17)	0.29(18)	0.26(14)	0.17(11)	0.15(10)
K_2O	0.02(2)	<d.l.	<d.l.	<d.l.	<d.l.	0.08(8)	<d.l.
Total	100.14	99.32	99.69	99.61	99.73	99.21	99.19
On the basis of 6 oxygens							
Si	1.98(5)	1.96(4)	1.97(5)	1.98(2)	1.98(3)	1.96(3)	1.97(2)
Ti	0.008(5)	0.006(3)	0.007(3)	0.006(3)	0.006(2)	0.008(1)	0.006(3)
Al	0.04(5)	0.03(3)	0.06(9)	0.05(4)	0.06(5)	0.07(5)	0.05(3)
Fe*	0.14(5)	0.13(3)	0.14(3)	0.14(1)	0.12(2)	0.09(4)	0.09(5)
Mn	0.004(2)	0.004(2)	0.004(2)	0.004(2)	0.003(1)	0.002(1)	0.002(2)
Mg	0.90(6)	0.93(6)	0.92(4)	0.91(4)	0.94(5)	0.97(6)	1.00(6)
Ca	0.92(2)	0.93(3)	0.88(12)	0.89(6)	0.87(7)	0.89(4)	0.87(4)
Na	0.02(1)	0.02(1)	0.02(1)	0.02(1)	0.02(1)	0.012(8)	0.010(6)
K	0.001(1)	---	---	---	---	0.004(4)	---
Mg#	86.5	87.7	86.7	86.7	88.7	91.5	91.7

Table 3.5 ***continued*** Average compositions of clinopyroxene

Run SPF-	**47X**	**72X**	**59X**	**63X**	**51X**	**49X**	**65X**
P (GPa)	2.21	2.21	2.21	2.21	2.21	2.21	2.21
T (°C)	1000	1100	1150	1200	1250	1300	1350
time (hrs)	72	121.5	70	70	75	49	72.5
n	10	10	10	34	10	10	20
SiO_2	54.12(86)	54.1(12)	54.7(12)	53.6(13)	54.0(14)	54.0(11)	53.99(94)
TiO_2	0.22(6)	0.23(6)	0.21(8)	0.20(9)	0.25(15)	0.22(8)	0.19(5)
Al_2O_3	0.65(48)	1.05(82)	1.19(68)	1.2(13)	1.4(13)	2.22(68)	2.01(96)
FeO*	4.24(71)	4.54(74)	4.65(31)	4.33(62)	4.3(13)	2.77(49)	2.57(63)
MnO	0.12(5)	0.12(3)	0.14(5)	0.12(3)	0.12(6)	0.09(5)	0.08(3)
MgO	16.64(65)	16.51(69)	16.69(83)	17.6(15)	17.0(19)	18.3(11)	19.4(10)
CaO	23.28(65)	22.5(19)	22.0(19)	21.9(25)	22.3(20)	21.55(89)	20.9(18)
Na_2O	0.29(13)	0.43(34)	0.38(18)	0.35(25)	0.27(13)	0.22(19)	0.20(13)
K_2O	0.05(6)	0.05(3)	0.06(8)	<d.l.	<d.l.	0.05(5)	0.04(3)
Total	99.61	99.53	100.02	99.30	99.64	99.42	99.38
On the basis of 6 oxygens							
Si	1.99(1)	1.99(1)	1.99(2)	1.97(4)	1.97(3)	1.96(3)	1.96(2)
Ti	0.006(2)	0.006(2)	0.006(2)	0.006(2)	0.007(4)	0.006(2)	0.005(1)
Al	0.03(2)	0.05(4)	0.05(3)	0.05(6)	0.06(6)	0.10(3)	0.08(4)
Fe*	0.13(2)	0.14(2)	0.14(1)	0.13(2)	0.13(4)	0.08(2)	0.08(2)
Mn	0.004(2)	0.004(1)	0.004(2)	0.004(1)	0.004(2)	0.003(2)	0.002(1)
Mg	0.91(4)	0.90(3)	0.91(4)	0.96(7)	0.9(1)	0.99(5)	1.05(5)
Ca	0.92(3)	0.88(7)	0.86(7)	0.86(11)	0.88(8)	0.84(4)	0.81(7)
Na	0.020(9)	0.03(2)	0.03(1)	0.03(2)	0.019(9)	0.02(1)	0.014(9)
K	0.002(3)	0.002(1)	0.003(4)	0.004(14)	0.004(15)	0.002(2)	0.002(2)
Mg#	87.5	86.5	86.7	88.1	87.4	92.5	92.9

Standard deviations in the last digit(s) are given in parentheses (2σ). n = number of analyses. <d.l. = below detection limit. Detection limits for all elements are ≤100 ppm, except for Ti (~150 ppm) and Fe (~150 ppm). Mg# defined in **Table 1**. FeO***** = Total iron

Table 3.6 Average compositions of phlogopite

Run SPF-	54X	61X	48X	30X	29X	32X	34X	36X	47X	72X	59X	63X	51X
P (GPa)	1.33	1.33	1.33	1.77	1.77	1.77	1.77	1.77	2.21	2.21	2.21	2.21	2.21
T (°C)	1000	1050	1100	900	1000	1100	1150	1200	1000	1100	1150	1200	1250
time (hrs)	70	70	70	75	71	47	72.5	46.5	72	121.5	70	70	75
n	20	21	18	49	39	18	20	18	22	18	25	29	17
SiO_2	39.8(15)	40.1(10)	39.6(18)	40.0(11)	40.2(13)	40.08(15)	39.9(13)	39.8(10)	40.5(11)	40.0(17)	39.9(14)	39.7(9)	40.04(77)
TiO_2	1.47(13)	1.49(16)	2.3(9)	1.49(39)	1.47(19)	1.45(10)	1.49(16)	1.95(47)	1.43(10)	1.49(22)	1.49(15)	1.55(14)	1.83(29)
Al_2O_3	13.31(64)	13.1(10)	14.7(12)	13.19(80)	13.4(11)	13.8(16)	13.95(94)	14.8(14)	13.44(84)	14.12(96)	14.12(57)	14.23(67)	14.73(78)
FeO*	6.79(41)	6.90(82)	4.57(47)	7.12(60)	6.96(64)	6.50(49)	6.16(19)	4.87(59)	6.61(51)	6.26(38)	5.97(16)	5.65(16)	4.46(24)
MnO	0.05(5)	0.05(4)	0.04(4)	0.06(4)	0.05(4)	0.06(3)	<d.l.	<d.l.	0.05(3)	<d.l.	0.05(4)	0.04(3)	<d.l.
MgO	22.17(61)	22.0(12)	22.0(30)	22.37(89)	22.6(11)	22.39(96)	22.16(66)	22.5(13)	22.5(10)	22.0(10)	21.97(52)	22.44(93)	22.98(83)
CaO	<d.l.	<d.l.	<d.l.	<d.l.	<d.l.	<d.l.	<d.l.	<d.l.	<d.l.	<d.l.	<d.l.	<d.l.	<d.l.
Na_2O	0.42(8)	0.39(13)	0.08(7)	0.42(13)	0.40(14)	0.23(11)	0.17(9)	0.08(7)	0.34(13)	0.14(13)	0.15(6)	0.12(9)	0.05(4)
K_2O	9.62(37)	9.50(84)	9.7(9)	9.70(55)	9.62(93)	9.86(74)	10.04(53)	10.40(86)	9.72(52)	10.07(39)	9.86(78)	10.0(12)	10.05(10)
F	0.80(7)	0.76(8)	1.45(38)	0.80(12)	0.76(12)	0.88(13)	0.81(9)	1.14(11)	0.78(9)	0.86(7)	0.83(10)	0.91(10)	1.17(12)
Cl	0.04(2)	0.02(2)	<d.l.	0.03(2)	0.02(2)	<d.l.	<d.l.	<d.l.	0.02(2)	0.02(2)	<d.l.	<d.l.	<d.l.
Total	94.47	94.31	94.44	95.18	95.48	95.25	94.68	95.54	95.39	94.96	94.34	94.64	95.31
On the basis of 22 oxygens													
Si	5.81(14)	5.83(11)	5.74(22)	5.81(12)	5.80(13)	5.80(23)	5.80(16)	5.73(12)	5.83(11)	5.80(14)	5.80(13)	5.76(13)	5.75(9)
Ti	0.16(1)	0.16(2)	0.25(12)	0.16(4)	0.16(2)	0.16(1)	0.16(2)	0.21(5)	0.16(1)	0.16(2)	0.16(2)	0.17(1)	0.20(3)
Al	2.29(12)	2.25(16)	2.52(24)	2.26(13)	2.28(16)	2.35(27)	2.39(15)	2.50(20)	2.28(13)	2.41(15)	2.42(12)	2.43(10)	2.49(11)
Fe	0.83(5)	0.84(10)	0.56(6)	0.86(7)	0.84(9)	0.79(6)	0.75(2)	0.59(8)	0.80(7)	0.76(6)	0.73(2)	0.69(2)	0.54(3)
Mn	0.01(1)	0.01(1)	0.01(1)	0.01(1)	0.01(1)	0.01(1)	---	---	0.01(1)	---	0.01(1)	0.01(1)	---
Mg	4.82(13)	4.79(23)	4.75(63)	4.84(16)	4.86(14)	4.83(19)	4.80(12)	4.82(29)	4.84(18)	4.76(16)	4.77(10)	4.86(16)	4.92(18)
Na	0.12(2)	0.11(4)	0.02(2)	0.12(4)	0.11(4)	0.07(3)	0.05(3)	0.02(2)	0.10(4)	0.04(4)	0.04(2)	0.03(4)	0.01(1)
K	1.79(6)	1.77(15)	1.79(18)	1.80(9)	1.77(16)	1.82(14)	1.86(8)	1.91(13)	1.79(8)	1.86(10)	1.83(13)	1.85(21)	1.84(19)
F	0.37(3)	0.35(4)	0.67(17)	0.37(5)	0.35(5)	0.40(5)	0.38(3)	0.52(6)	0.36(4)	0.40(4)	0.38(4)	0.42(4)	0.53(5)
Cl	0.01(1)	0.01(1)	---	0.01(1)	0.01(1)	---	---	---	0.01(1)	0.01(1)	---	---	---
Mg#	85.3	85.0	89.5	84.8	85.3	86.0	86.5	89.2	85.9	86.2	86.8	87.6	90.2

Standard deviations in the last digit(s) are given in parentheses (2σ). n = number of analyses. <d.l. = below detection limits. Detection limits for all elements are ≤150 ppm, except for Ti (~200 ppm) and F (~250 ppm). Mg# defined in **Table 1**. FeO* = Total iron

Table 3.7 Average compositions of apatite

Run SPF-	**54X**	**61X**	**30X**	**29X**	**32X**	**47X**	**72X**
P (GPa)	1.33	1.33	1.77	1.77	1.77	2.21	2.21
T (°C)	1000	1050	900	1000	1100	1000	1100
time (hrs)	70	70	75	71	47	72	121.5
n	7	9	13	9	6	11	7
SiO_2	0.46(12)	0.57(34)	0.37(24)	0.34(8)	0.45(22)	0.6(6)	0.67(60)
FeO*	0.72(38)	0.67(17)	0.59(22)	0.40(9)	0.65(23)	0.74(61)	0.81(5)
MnO	0.05(2)	0.06(3)	<d.l.	0.05(5)	0.06(3)	0.06(4)	0.07(4)
MgO	0.43(8)	0.51(16)	0.36(18)	0.35(12)	0.74(35)	0.63(33)	1.13(19)
CaO	52.6(16)	52.27(66)	53.0(15)	53.1(14)	53.2(31)	52.6(23)	51.50(70)
Na_2O	<d.l.	<d.l.	<d.l.	<d.l.	0.04(4)	<d.l.	<d.l.
K_2O	0.18(10)	<d.l.	<d.l.	0.06(4)	0.22(17)	0.16(10)	0.16(10)
P_2O_5	40.4(13)	39.9(24)	40.9(19)	41.11(68)	40.6(18)	40.5(17)	40.0(15)
F	1.60(21)	1.50(22)	1.79(32)	1.89(47)	1.85(31)	1.74(56)	1.57(43)
Cl	0.46(16)	0.20(6)	0.13(10)	0.18(17)	0.09(4)	0.09(4)	0.14(3)
Total	96.9	95.68	97.14	97.48	97.9	97.12	96.05
On the basis of 12 oxygens							
Si	0.04(1)	0.05(3)	0.03(2)	0.03(1)	0.04(2)	0.05(5)	0.06(5)
Fe	0.05(3)	0.05(1)	0.04(1)	0.01(1)	0.04(2)	0.05(4)	0.06(1)
Mg	0.05(1)	0.06(2)	0.04(3)	0.04(1)	0.09(4)	0.08(4)	0.14(2)
Ca	4.69(3)	4.71(16)	4.69(9)	4.69(7)	4.70(24)	4.66(23)	4.61(13)
K	0.02(1)	---	---	0.01(1)	0.02(2)	0.02(1)	0.02(1)
P	2.85(1)	2.83(6)	2.87(4)	2.87(2)	2.84(10)	2.84(8)	2.83(3)
F	0.42(6)	0.39(6)	0.47(9)	0.49(12)	0.48(9)	0.45(14)	0.41(11)
Cl	0.06(2)	0.03(1)	0.02(1)	0.03(3)	0.01(1)	0.01(1)	0.02(1)

Standard deviations in the last digit(s) are given in parentheses (2σ). n = number of analyses. <d.l. = below detection limits. Detection limits for all elements are ≤150 ppm, except for F (~200 ppm) and P (~190 ppm). Mg# defined in **Table 1**. FeO* = Total iron

Table 3.8 Average compositions of olivine

Run SPF-	**48X**	**87XX**	**53X**	**50X**	**36X**	**52X**	**91X**	**51X**	**49X**	**65X**
P (GPa)	1.33	1.33	1.33	1.33	1.77	1.77	1.77	2.21	2.21	2.21
T (°C)	1100	1200	1250	1300	1200	1250	1300	1250	1300	1350
time (hrs)	70	143.5	71	47	46.5	68	20	75	49	72.5
n	10	30	8	20	10	7	29	10	17	22
SiO_2	40.0(12)	40.5(11)	40.51(50)	40.96(73)	40.2(13)	40.68(22)	40.7(7)	40.2(10)	41.0(10)	40.9(12)
TiO_2	<d.l.	<d.l.	<d.l.	<d.l.	<d.l.	<d.l.	<d.l.	<d.l.	<d.l.	<d.l.
Al_2O_3	<d.l.	<d.l.	<d.l.	<d.l.	<d.l.	<d.l.	<d.l.	<d.l.	<d.l.	<d.l.
FeO*	13.15(34)	9.47(19)	9.77(23)	6.55(16)	13.35(30)	10.33(19)	7.87(27)	12.27(42)	9.40(35)	7.30(18)
MnO	0.19(4)	0.16(4)	0.14(4)	0.11(3)	0.18(4)	0.14(4)	0.11(3)	0.16(4)	0.12(4)	0.10(3)
MgO	46.0(13)	49.27(90)	49.5(16)	51.6(12)	45.4(14)	48.9(19)	50.9(8)	47.4(15)	49.1(24)	51.3(12)
CaO	0.46(13)	0.41(19)	0.45(9)	0.49(6)	0.38(10)	0.36(5)	0.49(17)	0.32(6)	0.33(13)	0.36(9)
Na_2O	<d.l.	<d.l.	<d.l.	<d.l.	<d.l.	<d.l.	<d.l.	<d.l.	<d.l.	<d.l.
K_2O	<d.l.	<d.l.	<d.l.	<d.l.	<d.l.	<d.l.	<d.l.	<d.l.	<d.l.	<d.l.
Total	99.80	99.81	100.37	99.71	99.51	100.41	100.07	100.35	99.95	99.96
On the basis 4 oxygens										
Si	1.0(1)	0.99(2)	0.99(2)	0.99(1)	1.01(2)	0.99(2)	0.99(1)	1.00(3)	1.00(4)	0.99(2)
Fe*	0.275(8)	0.20(3)	0.199(4)	0.14(3)	0.27(9)	0.22(5)	0.16(3)	0.24(6)	0.20(3)	0.15(2)
Mn	0.004(1)	0.003(1)	0.003(0)	0.002(1)	0.004(1)	0.003(2)	0.002(1)	0.003(1)	0.003(1)	0.002(1)
Mg	1.71(3)	1.80(4)	1.81(3)	1.86(5)	1.7(1)	1.78(6)	1.85(2)	1.76(7)	1.79(7)	1.85(5)
Ca	0.012(4)	0.011(5)	0.012(3)	0.013(2)	0.011(3)	0.009(1)	0.013(3)	0.007(7)	0.007(7)	0.010(3)
Mg#	86.1	90.0	90.1	93.0	86.3	89.0	92.0	88.0	89.9	92.5

Standard deviations are given in parentheses (2σ). n = number of analyses. <d.l. = below detection limits. Detection limits for all elements are ≤100 ppm, except for Ti (~150 ppm) and Fe (~150 ppm). Mg# defined in **Table 1**. FeO* = Total iron

Table 3.9 Fe-Mg exchange coefficients for olivine-liquid and clinopyroxene-liquid

Sample	$K_D(Fe\text{-}Mg)^{ol\text{-}liq}$	$K_D(Fe\text{-}Mg)^{cpx\text{-}liq}$
SPF87XX	0.30	0.22
SPF53X	0.31	0.26
SPF50X	0.32	0.24
SPF52X	0.33	0.26
SPF91X	0.32	0.33
SPF49X	0.33	0.27
SPF65X	0.33	0.33

Calculations for the exchange coefficient are based on the reaction Mg (mineral) + Fe^{2+} (melt) ↔ Mg (melt) + Fe^{2+} (mineral). General formula: $K_D(Fe-Mg)^{\min-melt} = (X_{FeO}^{\min} X_{MgO}^{melt})/(X_{FeO}^{melt} X_{MgO}^{\min})$, where X_z^y = mole fraction of oxide z in phase y

Table 3.10 Calculated temperatures and pressure using geothermometers and geobarometer from Putirka et al. (2007) and Putirka (2008)

			Glass-only	Ol-Liq	Cpx-Liq	Cpx-Liq
	Run Conditions		Putirka (2008)	Putirka et al. (2007)	Putirka (2008)	Putirka (2008)
Sample SPF-	T (°C)	P (GPa)	T (°C)	T (°C)	P (GPa)	T (°C)
87XX	1200	1.33	1220	1173	1.61	1258
53X	1250	1.33	1241	1207	1.52	1240
50X	1300	1.33	1316	1259	1.24	1318
52X	1250	1.77	1253	1221	1.83	1223
91X	1300	1.77	1324	1273	1.68	1330
49X	1300	2.21	1304	1269	2.40	1299
65X	1350	2.21	1345	1312	2.07	1355

Run conditions are provided for comparison with the calculated values for temperature and pressure

Table 3.11 Estimated percentage of iron loss in our experiments

Sample SPF-	% Fe Loss
87XX	24.6
53X	6.9
50X	20.8
52X	10.4
91X	9.2
49X	17.3
65X	24.4

% Fe Loss = $(FeO^*_{DAT\,4-5} - \sum X_i \times FeO^*_i) / FeO^*_{DAT\,4-5} \times 100\%$, where FeO^*_{DAT4-5} = the total iron in DAT4-5 (5.85 wt%), X_i = the modal percent of phase i, FeO^*_i = the average FeO* in phase i from the experiment

Table 3.12 Compositions used in pMELTS calculation

	MM3	G2
SiO_2	45.47	50.05
TiO_2	0.11	1.97
Al_2O_3	4.0	15.76
Fe_2O_3	0.585	1.518
Cr_2O_3	0.68	0
FeO	6.696	7.983
MnO	0	0.17
MgO	38.53	7.9
CaO	3.59	11.74
Na_2O	0.31	3.04
K_2O	0	0.03
Total	99.971	100.161
Mg#	90.5	60.1

Table 3.13 Comparison of the compositions of select mafic alkali-rich magmas

	Carmichael (1967)	**Holbig and Grove (2008)**	**Prelevic et al. (2008)**	**SPF53X**	**SPF50X**	**SPF91X**
	n = 13	---	---	n = 47	n = 112	n = 46
SiO_2	45.5(12)	46.8(1)	44.80	45.1(18)	46.8(17)	45.6(10)
TiO_2	2.3(3)	1.18(7)	1.22	1.35(14)	1.00(11)	1.13(13)
Al_2O_3	8.9(7)	12.27(1)	7.38	11.64(83)	8.29(35)	9.39(33)
FeO*	6.0(3)	9.04(20)	6.40	6.12(42)	5.37(18)	6.22(51)
MnO	0.15(2)	0.17(2)	0.11	0.11(5)	0.11(5)	0.11(4)
MgO	11.1(10)	10.45(1)	12.19	9.7(11)	13.41(41)	12.9(12)
CaO	11.8(18)	11.97(11)	11.90	10.5(10)	13.01(66)	11.8(13)
Na_2O	0.8(2)	3.32(15)	1.73	0.76(32)	0.63(30)	0.58(26)
K_2O	7.8(15)	3.56(2)	4.74	7.75(89)	5.44(21)	6.0(12)
P_2O_5	2.1(7)	1.30(8)	1.65	0.73(13)	0.51(9)	0.54(10)
F	---	0.10	---	0.81(13)	0.67(18)	0.66(14)
Cl	---	0.01	---	0.03(3)	<d.l.	<d.l.
H_2O+	3.5(12)	---	6.71	---	---	---
Total	99.83	100.06	99.05	94.60	95.24	94.93

Madupitic lamproite from the Leucite Hills, Wyoming (Carmichael 1967) with errors of 2σ; Tibetan shoshonite (Holbig and Grove 2008) with errors of 1σ; Mediterranean lamproite (Prelevic et al. 2008). The compositions of SPF53X, 50X and 91X are reported with errors of 2σ. n = number of analyses. <d.l. = below detection limits

References:

Barton M, Hamilton DL (1978) Water-saturated melting relationships to 5 kilobars of three Leucite Hills lavas. Contrib Mineral Petrol **66:** 41 - 49

Barton M, Hamilton DL (1979) The melting relationships of a madupite from the Leucite Hills, Wyoming, to 30 Kb. Contrib Mineral Petrol **69:** 133 - 142

Boari E, Tommasini S, Laurenzi MA, Conticelli S (2009) Transition from ultrapotassic kamafugitic to sub-alkaline magmas: Sr, Nd and Pb isotope, trace element and 40Ar/39Ar age data from the Middle latin Valley volcanic field, Roman Magmatic Province, Central Italy. J Petrol **50:** 1327 - 1357

Boyd FR, England JL (1960) Apparatus for phase equilibrium measurements at pressures up to 50 kilobars and temperatures to 1750°C. J Geophys Res **65:** 741 - 748

Buhlmann AL, Cavell P, Burwash RA, Creaser RA, Luth RW (2000) Minette bodies and cognate mica-clinopyroxenite xenoliths from the Milk River area, southern Alberta: records of a complex history of the northernmost part of the Archean Wyoming craton. Can J Earth Sci **37:** 1629 - 1650

Carlier G, Lorand JP (1997) First occurrence of diopside sanidine phlogopite lamproite in the Andean Cordillera: the Huacancha and Morojarja dikes, southern Peru. Can J Earth Sci **34:** 1118 - 1127

Carlson RW, Nowell GM (2001) Olivine-poor sources for mantle-derived magmas: Os and Hf isotopic evidence from potassic magmas of the Colorado Plateau. Geochem Geophys Geosyst **2:** 2000GC000128

Carman JH (1974) Synthetic sodium phlogopite and its two hydrates: Stabilities, properties, and mineralogic implications. Am Mineral **59:** 261 - 273

Carmichael ISE (1967) The Mineralogy and Petrology of the Volcanic Rocks from the Leucite Hills, Wyoming. Contrib Mineral Petrol **15:** 24 – 66

Chapman DS, Pollack HN (1977) Regional geotherms and lithospheric thickness. Geology **5:** 265 - 268

Conticelli S, Marchionni S, Rosa D, Giordano G, Boari E, Avanzinelli R (2009) Shoshonite and sub-alkaline magmas from an ultrapotassic volcano: Sr-Nd-Pb isotope data on the Roccamonfina volcanic rocks, Roman Magmatic Province, Southern Italy. Contrib Mineral Petrol **157:** 41 - 63

Conticelli S, Peccerillo A (1992) Petrology and geochemistry of potassic and ultrapotassic volcanism in central Italy: Petrogenesis and inferences on the evolution of mantle sources. Lithos **28:** 221 - 240

Edgar AD, Charbonneau HE (1991) Fluorine-bearing phases in lamproites. Mineral Petrol **44:** 125 - 149

Edgar AD, Condliffe E (1978) Derivation of K-rich ultramafic magmas from a peridotitic mantle source. Nature **275:** 639 - 640

Edgar AD, Condliffe E, Barnett RL, Shirran GJ (1980) An experimental study of an olivine ugandite magma and mechanisms for the formation of its K-enriched derivatives. J Petrol **21:** 475 - 497

Edgar AD, Green DH, Hibberson WO (1976) Experimental petrology of a highly potassic magma. J Petrol **17:** 339 - 356

Edgar AD, Pizzolato LA (1995) An experimental study of partitioning of fluorine between K-richterite, apatite, phlogopite and melt at 20 kbar. Contrib Mineral Petrol **121:** 247 - 257

Elkins-Tanton LT, Grove TL (2003) Evidence for deep melting of hydrous metasomatized mantle: Pliocene high-potassium magmas from the Sierra Nevadas. J Geophys Res **108:** 1 - 19

Esperanca S, Holloway JR (1987) On the origin of some mica-lamprophyres: experimental evidence from a mafic minette. Contrib Mineral Petrol **95:** 207 - 216

Foley SF (1992a) Petrological characterization of the source components of potassic magmas: Geochemical and experimental constraints. Lithos **28:** 187 - 204

Foley SF (1992b) Vein-plus-wall-rock melting mechanisms in the lithosphere and the origin of potassic alkaline magmas. Lithos **28:** 435 - 453

Foley SF, Musselwhite DS, Van Der Laan SR (1999) Melt compositions from ultramafic vein assemblages in the lithospheric mantle: a comparison of cratonic and non-cratonic settings. In: The JB Dawson volume, Proceedings of the VIIth International Kimberlite Conference **1:** 238 - 246

Foley SF, Taylor WR, Green DH (1986a) The effect of fluorine on phase relationships in the system $KAlSiO_4$-Mg_2SiO_4-SiO_2 at 28 kbar and the solution mechanism of fluorine in silicate melts. Contrib Mineral Petrol **93:** 46 - 55

Funk SP, Luth RW (ms. submitted) An experimental study of minettes from the Milk River area, southern Alberta, Canada. Contrib Mineral Petrol

Gee LL, Sack RO (1988) Experimental petrology of Melilite Nephelinites. J Petrol **29:** 1233 - 1255

Ghiorso MS, Hirschmann MM, Reiners PW, Kress VC III (2002) The pMELTS: A revision of MELTS for improved calculation of phase relations and major element partitioning related to partial melting of the mantle to 3 GPa. Geochem Geophys Geosyst **3**: 10.1029/2001GC000217.

Holbig ES, Grove TL (2008) Mantle melting beneath the Tibetan Plateau: Experimental constraints on ultrapotassic magmatism. J Geophys Res **113:** B04210

Jiang YH, Jiang SY, Ling HF, Dai BZ (2006) Low-degree melting of a metasomatized lithospheric mantle for the origin of Cenozoic Yulong monzogranite-porphyry, east Tibet: Geochemical and Sr-Nd-Pb-Hf isotopic constraints. Earth Planet Sci Lett **241:** 617 - 633

Lloyd FE, Bailey DK (1975) Light element metasomatism of the continental mantle: evidence and the consequences. Phys Chem Earth **9:** 389 - 415

Lloyd FE, Arima M, Edgar AD (1985) Partial melting of a phlogopite-clinopyroxenite nodule from south-west Uganda: an experimental study bearing on the origin of highly potassic continental rift volcanics. Contrib Mineral Petrol **91:** 321 – 329

Luth RW (1997) Experimental study of the system phlogopite-diopside from 3.5 to 17 GPa. Am Mineral **82:** 1198 - 1209

Macdonald R, Upton BGJ, Collerson KD, Hearn Jr BC, James D (1992) Potassic mafic lavas of the Bearpaw Mountains, Montana: mineralogy, chemistry, and origin. J Petrol **33:** 305 - 346

Melzer S, Foley SF (2000) Phase relations and fractionation sequence in potassic magma series modelled in the system $CaMgSi_2O_6$-$KAlSiO_4$-Mg_2SiO_4-SiO_2-F_2O_{-1} at 1 bar to 18 kbar. Contrib Mineral Petrol **138:** 186 - 197

Mitchell RH (1995) Melting experiments on a sanidine phlogopite lamproite at 4 - 7 GPa and their bearing on the sources of lamproite magma. J Petrol **36:** 1455 - 1474

Modreski PJ, Boettcher AL (1973) Phase relationships of phlogopite in the system K_2O-MgO-CaO-Al_2O_3-SiO_2-H_2O to 35 kilobars: A better model for micas in the interior of the Earth. Am J Sci **273:** 385 - 414

Navon O, Stolper E (1987) Geochemical consequences of melt percolation: the upper mantle as a chromatographic column. J Geol **95:** 285 - 307

Nicholls IA, Whitford DJ (1983) Potassium-rich volcanic rocks of the Muriah complex, Java, Indonesia: Products of multiple magma sources? J Volcanol Geotherm Res **18:** 337 - 359

Nikogosian IK, van Bergen MJ (2010) Heterogeneous mantle sources of potassium-rich magmas in central-southern Italy: Melt inclusion evidence from Roccamonfina and Ernici (Mid Latina Valley). J Volcano Geothermal Res **197:** 279 - 302

Patino Douce AE (1993) Titanium substitution in biotite: An empirical model with applications to thermometry, O_2 and H_2O barometries and consequences for biotite stability. Chem Geol **108:** 133 - 162

Pilet S, Baker MB, Stolper EM (2008) Metasomatized lithosphere and the origin of alkaline lavas. Science **320:** 916 - 919

Prelevic D, Foley SF, Romer R, Conticelli S (2008) Mediterranean Tertiary lamproites derived from multiple source components in postcollisional geodynamics. Geochim Cosmochim Acta **72:** 2125 - 2156

Putirka K (1999) Clinopyroxene + liquid equilibria to 100 kbar and 2450 K. Contrib Mineral Petrol **135:** 151 - 163

Putirka K (2008) Thermometers and Barometers for Volcanic Systems. In: Putirka K and Tepley F (eds) Rev Mineral Geochem, vol 69, pp 61 - 120

Putirka K, Johnson M, Kinzler R, Walker D (1996) Thermobarometry of mafic igneous rocks based on clinopyroxene-liquid equilbria, 0 - 30 kbar. Contrib Mineral Petrol **123:** 92 - 108

Putirka K, Perfit M, Ryerson FJ, Jackson MG (2007) Ambient and excess mantle temperatures, olivine thermometry, and active vs. passive upwelling. Chem Geol **241:** 177 - 206

Putirka KD, Mikaelian H, Ryerson F, Shaw H (2003) New clinopyroxene-liquid thermobarometers for mafic, evolved, and volatile-bearing lava compositions, with applications to lavas from Tibet and the Snake River Plain, Idaho. Am Mineral **88:** 1542 - 1554

Righter K, Carmichael ISE (1996) Phase equilibria of phlogopite lamprophyres from western Mexico: Biotite-liquid equilibria and P-T estimates for biotite-bearing igneous rocks. Contrib Mineral Petrol **123:** 1 - 21

Roeder PL, Emslie RF (1970) Olivine-liquid equilibrium. Contrib Mineral Petrol **29:** 275 - 289

Sack RO, Walker D, Carmichael ISE (1987) Experimental petrology of alkalic lavas: constraints on cotectics of multiple saturation in natural basic liquids. Contrib Mineral Petrol **96:** 1 - 23

Sato K (1997) Melting experiments on a synthetic olivine lamproite composition up to 8 GPa: Implications to its petrogenesis. J Geophys Res **102:** 14,751 - 14,764

Snyder DA, Carmichael ISE (1992) Olivine-liquid equilibria and the chemical activities of FeO, NiO, Fe_2O_3 and MgO in natural basic melts. Geochim Cosmochim Acta **56:** 303 - 318

Sweeney RJ, Rhompson AB, Ulmer P (1993) Phase relations of a natural MARID composition and implications for MARID genesis, lithospheric melting and mantle metasomatism. Contrib Mineral Petrol **115:** 225 - 241

Tronnes RG, Edgar AD, Arima M (1985) A high pressure-high temperature study of TiO_2 solubility in Mg-rich phlogopite: Implication to phlogopite chemistry. Geochim Cosmochim Acta **49:** 2323 - 2329.

Van Kooten GK (1980) Mineralogy, petrology, and geochemistry of an ultra-potassic basaltic suite, central Sierra Nevada, California, USA. J Petrol **21:** 651 - 684

Vukadinovic D, Edgar AD (1993) Phase relations in the phlogopite-apatite system at 20 kbar; implications for the role of fluorine in mantle melting. Contrib Mineral Petrol **114:** 247 - 254

Wallace P, Carmichael ISE (1989) Minette lavas and associated leucitites from the Western Front of the Mexican Volcanic Belt: petrology, chemistry and origin. Contrib Mineral Petrol **103:** 470 - 492

Yoder, Jr HS, Kushiro, I (1969) Melting of a hydrous phase: phlogopite. Am J Sci **267-A:** 558 - 582

Chapter 4: Geotectonic Model and Future Research:

The kimberlite corridor (KC) (**Figure 1.1**), as defined by Heaman et al. (2003; 2004) and Currie and Beaumont (2011), stretches southward from the Slave craton in the Northwest Territories, Canada, through the Wyoming craton and Colorado Plateau in the United States, approximately 1000 km inland from the west coast of North America. The main emplacement ages for these alkali-rich magmas occurred from ca. 110 Ma to ca. 45 Ma, trailing to ca. 25 Ma in some locations (see Currie and Beaumont 2011 for a review). Many authors who have studied the Montana and Wyoming high-potassium magmas suggest that an ancient lithospheric cratonic mantle, an asthenospheric mantle (mantle wedge), and a younger component (usually interpreted to be subducted oceanic crust) are involved in the generation of these magmas (Fraser et al. 1985; Dudas et al. 1987; Eggler et al. 1987; Meen and Eggler 1987; Mitchell et al. 1987; Hyndman et al. 1988; Scambos and Farmer 1988; Irving 1990; Dudas 1991; O'Brien et al. 1991, 1995; Macdonald et al. 1992; Buhlmann et al. 2000; Downes et al. 2004; Facer et al 2009; Smith 2010). Many of these authors, to varying extents, invoke the dehydration of the subducting Farallon plate in the genesis of the alkaline magmas in western North America.

In Chapter 2, I report the results of liquidus experiments on the most primitive minette from Milk River (RAB90 Au24-1), which found that this composition was in equilibrium with orthopyroxene and olivine at 1.77 GPa and 1350°C. Notwithstanding, I argue that the composition of the minettes (e.g. 8.02 wt% CaO; 4.44 wt% K_2O; 1.02 wt% P_2O_5 for RAB90 Au24-1) is best explained by partial melting of a vein assemblage comprising phlogopite + clinopyroxene + apatite. Based on the work of Navon and Stolper (1987) and Foley (1992), I suggested that the primary minette magma re-equilibrated with the wall-rock during ascent via dissolution of orthopyroxene and olivine. The multiple saturation point is at a high temperature

for cratonic mantle (~600-700°C), and it is unlikely that the craton rose by >500°C to induce partial melting. Rather, I propose that melting likely occurred at greater depths (base of craton?), possibly requiring the introduction of hydrous fluids. The trace element (HFSE-depleted and LILE-enriched) composition of the minettes supports a subduction-related origin, and therefore it is likely that hydrous fluids derived from the subducting slab were involved in triggering partial melting (Buhlmann et al. 2000).

For any numerical model to be realistic, it must support the known geochemical and geochronological constraints. Recently, geodynamical simulations (Liu et al. 2008; Currie and Beaumont 2011) have tested the possibility that the Farallon plate was involved in the genesis of the alkaline magmas in western North America. In Currie and Beaumont's numerical model, the hydrated Farallon plate subducts underneath a thick, cool Archean craton, already embedded with metasomatic veins (in this discussion we will assume mica-clinopyroxenite veins) (**Figure 4.1a**). The subduction of the Farallon plate during the Cretaceous period (~100 Ma) was originally steep, resulting in typical arc magmatism (Currie and Beaumont 2011). Currie and Beaumont demonstrated that rapid subduction of the Farallon plate coupled with westward motion of the North American plate resulted in a progressive decrease in subduction angle (**Figure 4.1b**). A consequence of shallowing subduction is the landward movement of the asthenospheric mantle wedge (Currie and Beaumont 2011). Sixty million years after the onset of low-angle subduction (~40 Ma), the Farallon plate would be sub-parallel to the lithosphere. The shallow-angled, old oceanic slab would remain cool, allowing hydrous minerals (e.g. phlogopite, amphibole, serpentine, chlorite) to persist ≥1000-1500 km away from the trench. This placed the "wet" region of the Farallon plate underneath the Wyoming craton (Currie and Beaumont 2011).

Currie and Beaumont argued that the devolatilization of the Farallon plate triggered alkali magmatism in the region (**Figures 4.1c, d**).

Facer et al. (2009) studied the spinel dunite xenoliths from the Bearpaw Mountains, Montana, USA, and found that the xenoliths were serpentinized and had high B, Cl and H_2O contents. They argued that the presence of serpentine and the concentrations of B and Cl in the xenoliths were consistent with metasomatism by hydrous fluids derived from a subducting slab, likely the Farallon plate. Smith (2010) conducted a similar study on antigorite peridotite, Cr-magnetite dunite, chlorite harzburgite, and other ultramafic rock fragments from the Colorado Plateau, United States. He argued that the serpentinization of these rocks was consistent with hydrous fluids acting as metasomatic agents infiltrating the mantle underneath the Colorado Plateau. Smith also suggested that these fluids were likely derived from the Farallon plate.

The presence of xenoliths in the minettes at Milk River are consistent with the hypothesis that these magmas rose to the surface rapidly, likely through pre-existing cracks and fissures in the lithosphere (**Figure 4.1e**) (Sparks et al. 1977; Spera 1984). A consequence of rapid ascent rates, coupled with slow cooling rates, is that the primary melt derived from partial melting of the vein assemblage would preserve the high (near-liquidus) temperatures of melting (Sparks et al. 1977; Spera 1984). Based on the multiple saturation point found in Chapter 2, the primary melt likely stalled at ~58 km (~1.77 GPa) (**Figure 4.1f**), where it re-equilibrated with the surrounding harzburgite wall-rock via dissolution of orthopyroxene (**Figures 4.1g, h**).

Assuming the composition of the metasomatic veins at the base of the craton is appropriate, Currie and Beaumont's model accounts for the major- and trace-element, and isotopic composition of our minettes and accurately predicts the age of formation. However, a

key feature of Currie and Beaumont's model is that melting was induced by fluid fluxing, directly implicating the Farallon plate in the genesis of the alkaline rocks. To test this key feature of their model, experiments would need to be conducted where 1) water is added to our mica-clinopyroxenite xenolith, and the depression of the solidus is characterized; and 2) the pressures are extended to depths approaching the base of the craton (~150 - 250 km). By comparing the water-saturated, depressed solidus with a cratonic mantle geotherm, we could see if melting could be induced simply by introducing hydrous fluids or if external heating is also required.

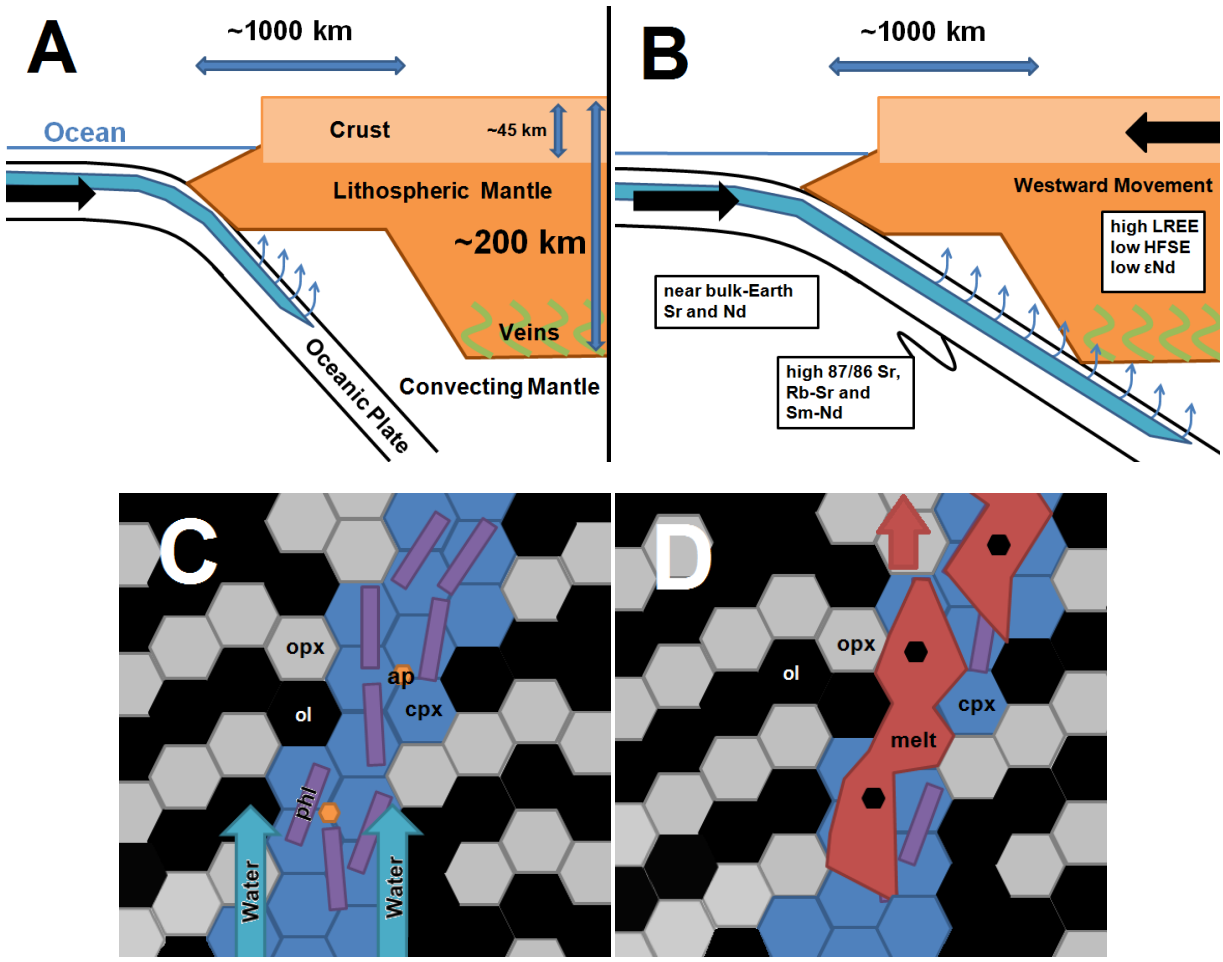

Figures 4.1a-d Tectonic and petrogenetic model for the minettes at Milk River, southern Alberta. **a**) the basic geometry of the Farallon plate (oceanic plate) and the North American plate (crust plus lithospheric mantle and veins) at ca. 100 Ma. **b**) westward movement of the North American continent, coupled with rapid subduction of the Farallon plate, causes the oceanic slab to shallow, ca. 50 Ma (Buhlmann et al. 2000). The "wet" region of the slab now extends >1000 km inland, allowing hydrous fluids to infiltrate the base of the cratonic lithospheric mantle. Also shown are the isotopic and some trace-element characteristics of the three components needed in the petrogenesis of the minettes (O'Brien et al. 1991, 1995). **c**) close-up of the harzburgite wall-rock imbedded with an apatite-bearing mica-clinopyroxenite vein. The vein assemblage is assumed to be at or close to the base of the craton (~200 km depth) and at an ambient temperature (based on a 40 mW m^{-2} geotherm) of ~1400°C. Hydrous fluids derived from the dehydration of the Farallon plate are assumed to be the trigger for partial melting. **d**) partial melting is focused on the vein because it has a lower solidus temperature relative to the surrounding refractory harzburgite. Based on the studies of Yoder and Kushiro (1969) and Modreski and Boettcher (1973), olivine is produced during the melting of phlogopite. The red arrow indicates that once the primary melt reaches a critical buoyancy, it will rise through pre-existing fractures in the lithospheric mantle

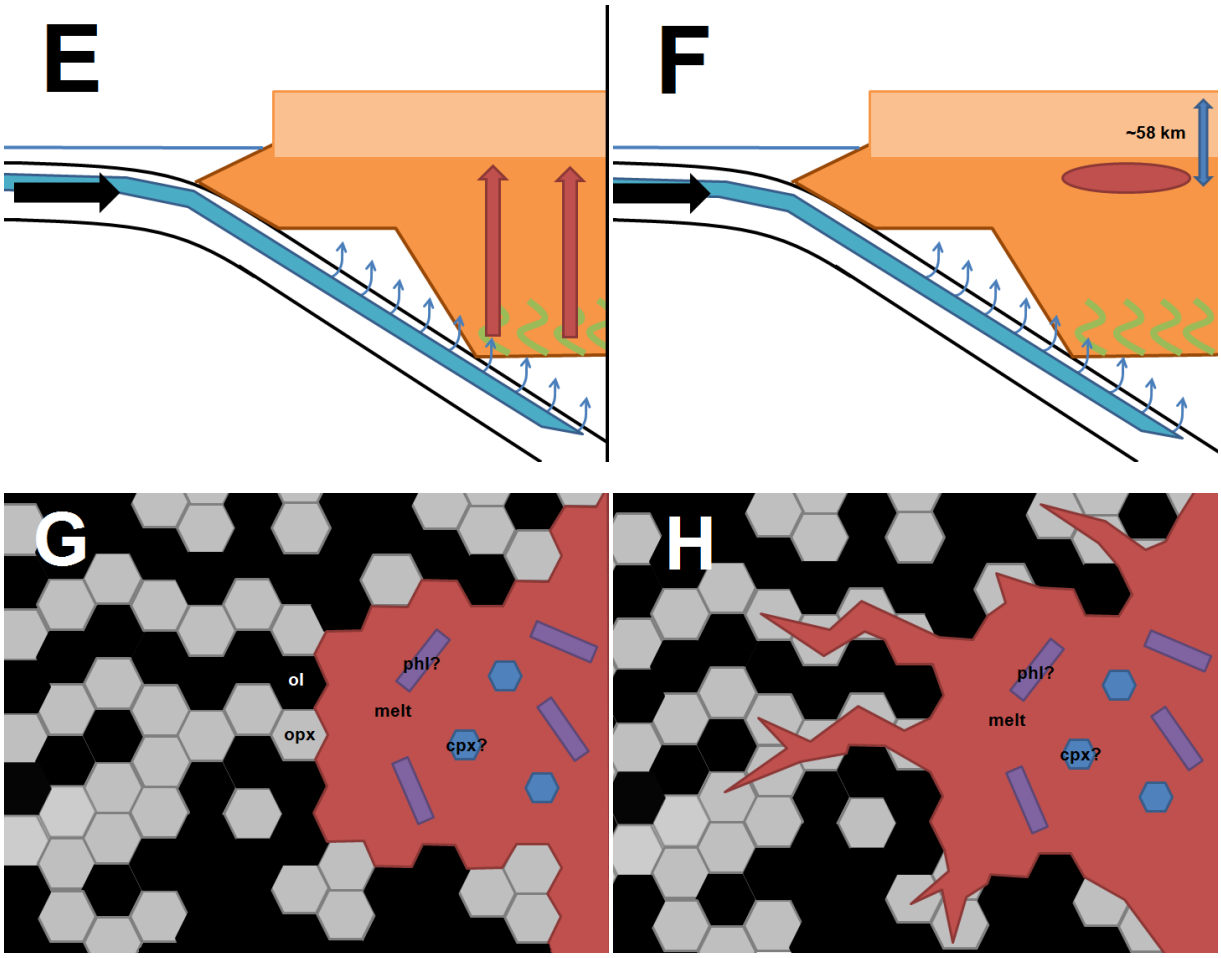

Figures 4.1e-h *continued* Tectonic and petrogenetic model for the minettes at Milk River, southern Alberta. **e**) the primary melt rises rapidly through the cratonic lithospheric mantle, preserving a near-liquidus temperature of ~1350°C (based on the multiple saturaiton point found in Chapter 2) (Sparks et al. 1977; Spear 1984). **f**) based on the multiple saturation point found in Chapter 2, the primary melt likely stalls at a depth of 58 km (~1.77 GPa), where it forms a magma chamber. **g**) close-up of the magma chamber (possibly containing entrained clinopyroxene and/or phlogopite) surrounded by a harzburgite wall-rock. **h**) the primary melt begins to dissolve the surrounding orthopyroxene in an attempt to establish equilibrium (Foley 1992).

References:

Buhlmann AL, Cavell P, Burwash RA, Creaser RA, Luth RW (2000) Minette bodies and cognate mica-clinopyroxenite xenoliths from the Milk River area, southern Alberta: records of a complex history of the northernmost part of the Archean Wyoming craton. Can J Earth Sci **37:** 1629 - 1650

Currie CA, Beaumont C (2011) Are diamond-bearing Cretaceous kimberlites related to low-angle subduction beneath western North America? Earth Planet Sci Let **303:** 59 - 70

Downes H, MacDonald R, Upton BGJ, Cox KG, Bodinier J-L, Mason PRD, James D, Hill PG, Hearn, Jr BC (2004) Ultramafic xenoliths from the Bearpaw Mountains, Montana, USA: Evidence formultiple metasomatic events in the lithospheric mantle beneath the Wyoming craton. J Petrol **45:** 1631 - 1662

Dudas FO (1991) Geochemistry of igneous rocks of the Crazy Mountains, Montana, and tectonic models for the Montana alkalic province. J Geophys Res **96:** 13261 - 13277

Dudas FO, Carlson RW, Eggler DH (1987) Regional Middle Proterozoic enrichment of the subcontinental mantle source of igneous rocks from central Montana. Geology, **15:** 22 - 25

Eggler DH, McCallum ME, Kirkley MB (1987) Kimberlite-transported nodules from Colorado-Wyoming; a record of enrichment of shallow portions of an infertile lithosphere. Geological Society of America, Special Papers, **215:** 77 - 90

Facer J, Downes H, Beard A (2009) *In situ* serpentinization and hydrous fluid metasomatism in spinel dunite xenoliths from the Bearpaw Mountains, Montana, USA. J Petrol **50:** 1443 - 1475

Foley SF (1992) Vein-plus-wall-rock melting mechanisms in the lithosphere and the origin of potassic alkaline magmas. Lithos, **28:** 435 - 453

Fraser KJ, Hawkenworth CJ, Erlank AJ, Mitchell RH, Scott-Smith BH (1985) Sr, Nd, and Pb isotope and minor-element geochemistry of lamproites and kimberlites. Earth Planet Sci Lett **76:** 57 - 70

Heaman LM, Kjarsgaard BA, Creaser RA (2003) The timing of kimberlite magmatism in North America: implications for global kimberlite genesis and diamond exploration. Lithos **71:** 153 – 184

Heaman LM, Kjarsgaard BA, Creaser RA (2004) The temporal evolution of North American kimberlites. Lithos **76:** 377 - 397

Hyndman DW, Tureck-Schwartz K, Foland KA (1988) Chemical and isotopic evidence for potassic mafic magmas from an old K-enriched mantle source and for Eocene crustal melting in the central Montana alkalic province. Geological Society of America, Abstracts with Programs, **20:** A195

Irving AJ (1990) Montana Archean lithospheric mantle: chemical constraints from Eu-anomalous ultramafic xenoliths in minette. EOS Transactions, American Geophysical Union, **71:** 1712

Liu L, Spasojevic S, Gurnis M (2008) Reconstructing Farallon Plate subduction beneath North America back to the Late Cretaceous. Science **322:** 934–938

Macdonald R, Upton BGJ, Collerson KD, Hearn Jr BC, James D (1992) Potassic mafic lavas of the Bearpaw Mountains, Montana: mineralogy, chemistry, and origin. J Petrol **33:** 305 - 346

Meen JK, Eggler DH (1987) Petrology and geochemistry of the Cretaceous Independence volcanic suite, Absoroka Mountains, Montana: clues to the composition of the Archean sub-Montana mantle. Geological Society of America Bulletin, **98:** 238 - 247

Mitchell RH, Platt RG, Downey M (1987) Petrology of lamproites from Smoky Butte, Montana. J Petrol **28:** 645 - 677

Modreski PJ, Boettcher AL (1973) Phase relationships of phlogopite in the system K_2O-MgO-CaO-Al_2O_3-SiO_2-H_2O to 35 kilobars: A better model for micas in the interior of the Earth. Am J Sci **273:** 385 - 414

Navon O, Stolper E (1987) Geochemical consequences of melt percolation: the upper mantle as a chromatographic column. J Geol **95:** 285 - 307

O'Brien HE, Irving AJ, McCallum IS (1991) Eocene potassic magmatism in the Highwood Mountains, Montana: petrology, geochemistry and tectonic implications. J Geophys Res **96:** 13237 - 13260

O'Brien HE, Irving AJ, McCallum IS, Thirlwall MF (1995) Strontium, neodymium, and lead isotopic evidence for the interaction of post-subduction asthenospheric potassic mafic magmas of the Highwood Mountains,

Montana, USA, with ancient Wyoming craton lithospheric mantle. Geochim Cosmochim Acta **59:** 4539 - 4556

Scambos TA, Farmer GL (1988) Multiple source components for alkalic igneous rocks in the Wyoming Province: isotopic and trace element evidence from central Montana. EOS Transactions, American Geophysical Union, **69:** 1510

Smith D (2010) Antigorite Peridotite, Metaserpentinite, and other Inclusions within Diatremes on the Colorado Plateau, SW USA: Implications for the Mantle Wedge during Low-angle Subduction. J Petrol **51:** 1355 - 1379

Sparks RSJ, Pinkerton H, MacDonald R (1977) The transport of xenoliths in magmas. Earth Planet Sci Lett **35:** 234 - 238

Spera FJ (1984) Carbon dioxide in petrogenesis III: role of volatiles in the ascent of alkaline magma with special reference to xenolith-bearing mafic lavas. Contrib Mineral Petrol **88:** 217 - 232

Yoder, Jr HS, Kushiro, I (1969) Melting of a hydrous phase: phlogopite. Am J Sci **267-A:** 558 - 582

Chapter 5: General Summary and Conclusions:

Minettes from southern Alberta, Canada, crop out as dykes near the Milk River area. Coarse-grained xenoliths composed of phlogopite, clinopyroxene and apatite were carried up in the minette dykes. Buhlmann et al. (2000) previously studied these rocks, and proposed that the minettes were formed from a source region composed of phlogopite and clinopyroxene, at depths $\geq$ 1.7 GPa. Their hypothesis is supported by many experimental (e.g.: Esperanca and Holloway 1987) and geochemical (e.g.: Macdonald et al. 1992) studies on similar mafic, alkali-rich magmas. We conducted our study to test Buhlmann et al.'s hypothesis experimentally.

Our first series of experiments involved locating a multiple saturation point along the liquidus of a primitive minette (RAB90 Au24-1). Experiments were conducted between 1.33-2.21 GPa, and 1300-1400°C. We found that olivine was the sole liquidus phase at 1.33 and 1.55 GPa, whereas orthopyroxene was the liquidus phase at 2.0 and 2.21 GPa. We discovered a multiple saturation point at 1350°C and 1.77 GPa where olivine and orthopyroxene coexists with liquid. Clinopyroxene and phlogopite are not liquidus phases. Our findings are not consistent with Buhlmann et al.'s hypothesis and the general consensus of previous studies. We argue that the whole-rock composition (e.g. 8.02 wt% CaO; 4.44 wt% K_2O) of the minette is best explained by partial melting of a source containing phlogopite and clinopyroxene. To reconcile our experiments with studies such as Esperanca and Holloway (1987), we turned to the models proposed by Navon and Stopler (1987) and Foley (1992), where our multiple saturation point is interpreted as the re-equilibration of the minette with the surrounding harzburgite wall-rock during ascent.

Our second series of experiments simulated possible melting processes that may have occurred in the cratonic mantle. We chose a mica-clinopyroxene xenolith that was "representative" of a mantle lithology, and conducted melting experiments between 1.33-2.21 GPa, and 900-1350°C. We found that the solidus was steep and at temperatures above a normal cratonic geotherm. Therefore, melting must be induced by either raising the temperature of the surrounding wall-rocks or by introducing hydrous fluids. We found that the composition of our melts were similar to other mafic alkali-rich magmas (e.g. madupitic lamproite from Carmichael 1967). Using variation diagrams and a binary mixing model, we plotted the composition of one of our experimental glasses (SPF52X shown) along with the RAB90 Au24-1 minette and representative populations of mantle orthopyroxene and olivine. We found that the minette was on a linear trajectory between the 52X melt and mantle orthopyroxene, consistent with the wall-rock dissolution model proposed by Foley (1992).

We conclude that the RAB90 Au24-1 minette likely formed by partial melting a source containing clinopyroxene, phlogopite and trace amounts of apatite at a pressures ≥1.7 GPa, and that the minette likely re-equilibrated with mantle orthopyroxene during ascent via dissolution.

References:

Buhlmann AL, Cavell P, Burwash RA, Creaser RA, Luth RW (2000) Minette bodies and cognate mica-clinopyroxenite xenoliths from the Milk River area, southern Alberta: records of a complex history of the northernmost part of the Archean Wyoming craton. Can J Earth Sci **37:** 1629 - 1650

Carmichael ISE (1967) The Mineralogy and Petrology of the Volcanic Rocks from the Leucite Hills, Wyoming. Contrib Mineral Petrol **15:** 24 - 66

Esperanca S, Holloway JR (1987) On the origin of some mica-lamprophyres: experimental evidence from a mafic minette. Contrib Mineral Petrol **95:** 207 - 216

Foley SF (1992) Vein-plus-wall-rock melting mechanisms in the lithosphere and the origin of potassic alkaline magmas. Lithos, **28:** 435 - 453

Macdonald R, Upton BGJ, Collerson KD, Hearn Jr BC, James D (1992) Potassic mafic lavas of the Bearpaw Mountains, Montana: mineralogy, chemistry, and origin. J Petrol **33:** 305 - 346

Navon O, Stolper E (1987) Geochemical consequences of melt percolation: the upper mantle as a chromatographic column. J Geol **95:** 285 - 307

Appendix A: MATLAB algorithm:

Table A1: Input data for SPF26

	Minette =	Olivine =	Orthopyroxene =	ExpMelt =	Quality
SiO2	45.3400	40.4700	56.3600	46.0643	99
TiO2	1.0200	0	0.1430	1.1023	99
Al2O3	9.2200	0	2.0700	10.1743	99
FeO*	9.0000	10.9300	6.8200	8.2600	90
MnO	0.1400	0.1020	0.1240	0.1437	99
MgO	13.6300	48.1800	31.6200	12.1643	99
CaO	8.0200	0.2430	2.0500	8.4286	99
Na2O	1.3000	0	0.0540	1.9561	99
K2O	4.4400	0	0	4.8857	99
P2O5	1.0200	0	0	1.1171	99

```
%This is a sample calculation for how to calculate modes, estimate the
percentage of iron loss, and assessing the general quality of the fit using a
MATLAB algorithm (data used is for SPF 26). This algorithm removes FeO* from
the calculations.
clear all;
SPF26data=xlsread('SPF26_Modes.xls'); %Load the data from the excel
spreadsheet
Minette=SPF26data(:,1); %Denotes the minette data in the form of a vector
Olivine=SPF26data(:,2); %Denotes the olivine data in the form of a vector
Orthopyroxene=SPF26data(:,3); %Denotes the orthopyroxene data in the form of
a vector
ExpMelt=SPF26data(:,4); %Denotes the experimental liquid data in the form of
a vector
Quality=SPF26data(:,5); %Arbitrary quality control where everything is 99
except for FeO* which is denoted as 90
%Remove FeO* from the data so that it does not affect the modal
%calculations
No_Iron=find(Quality==99); %Chooses everything except for FeO*
Minette_No_Iron=Minette(No_Iron); %Minette data with no FeO* present
Olivine_No_Iron=Olivine(No_Iron); %Olivine data with no FeO* present
Orthopyroxene_No_Iron=Orthopyroxene(No_Iron); %Orthopyroxene data with no
FeO* present
ExpMelt_No_Iron=ExpMelt(No_Iron); %Experimental liquid data with no FeO*
present
A=sum(Minette_No_Iron); %Finds the total for the minette
B=sum(Olivine_No_Iron); %Finds the total for the olivine
C=sum(Orthopyroxene_No_Iron); %Finds the total for the orthopyroxene
D=sum(ExpMelt_No_Iron); %Finds the total for the experimental liquid
```

Table A2: The data for SPF26 but with FeO* removed

	Minette_No_Iron =	Olivine_No_Iron =	Orthopyroxene_No_Iron =	ExpMelt_No_Iron =
SiO2	45.3400	40.4700	56.3600	46.0643
TiO2	1.0200	0	0.1430	1.1023
Al2O3	9.2200	0	2.0700	10.1743
MnO	0.1400	0.1020	0.1240	0.1437
MgO	13.6300	48.1800	31.6200	12.1643
CaO	8.0200	0.2430	2.0500	8.4286
Na2O	1.3000	0	0.0540	1.9561

K2O	4.4400	0	0	4.8857
P2O5	1.0200	0	0	1.1171
Sums	A = 84.1300	B = 88.9950	C = 92.4210	D = 86.0364

```
NormMinette=100*Minette_No_Iron/A; %Normalizes the minette so that the total
is 100%
NormOlivine=100*Olivine_No_Iron/B; %Normalizes the olivine so that the total
is 100%
NormOrthopyroxene=100*Orthopyroxene_No_Iron/C; %Normalizes the orthopyroxene
so that the total is 100%
NormExpMelt=100*ExpMelt_No_Iron/D; %Normalizes the experimental liquid so
that the total is 100%
%Now we must create our matrix. We will create the M matrix, which will
%contain the normalized compositions for all the phases present in our
%experiments without FeO*.
M(:,1)=NormOlivine; %Denotes the first column as the normalized olivine
composition
M(:,2)=NormOrthopyroxene; %Denotes the second column as the normalized
orthopyroxene composition
M(:,3)=NormExpMelt; %Denotes the third column as the normalized experimental
liquid composition
```

M =

45.4745	60.9818	53.5404
0	0.1547	1.2812
0	2.2398	11.8256
0.1146	0.1342	0.1670
54.1379	34.2130	14.1385
0.2730	2.2181	9.7965
0	0.0584	2.2736
0	0	5.6787
0	0	1.2985

```
%Recall that the normalized minette is what we will compare this matrix to.
%Now we must find the values of our modes. We do this by using the method of
%projections. Recall that in MATLAB M' is the transpose of the matrix M.
X=inv(M'*M)*M'*NormMinette;
%However, we must normalize the modal abundances so that they add up to
%100%.
XX=sum(X); % This is what the sum of the modal abundances just calculated add
up to.
Xnorm=100/XX*X; %This is the normalized modal abundances for olivine,
orthopyroxene and liquid that now add up to 100%.
```

Xnorm =

2.4463

5.0914

92.4624

```
%We can also use this program to estimate the percentage of iron loss;
FeO=find(Quality==90); %This seeks out only FeO*
Minette_FeO=Minette(FeO); %The FeO* content for the minette
Olivine_FeO=Olivine(FeO); %The FeO* content for olivine
Orthopyroxene_FeO=Orthopyroxene(FeO); %The FeO* content for orthopyroxene
ExpMelt_FeO=ExpMelt(FeO); %The FeO* content for the experimental liquid
X_ol=Xnorm(1); %The modal abundance for olivine in %
X_opx=Xnorm(2); %The modal abundance for orthopyroxene in %
X_liq=Xnorm(3); %The modal abundance for the experimental liquid in %
Fe_Loss=((Minette_FeO-(X_ol/100)*Olivine_FeO-(X_opx/100)*Orthopyroxene_FeO-
(X_liq/100)*ExpMelt_FeO)/Minette_FeO)*100; %The estimated percentage of iron
loss
```

Fe_Loss =

8.3111

```
%We can also assess the quality of the fit by assessing the sum of residual
%squares. Note that I have chosen to put less emphasis on SiO2 and Al2O3
%because these are the two oxides that are the hardest to fit. I have
%chosen values of 0.5 and 0.6 arbitrarily, but you may choose any value you
%see fit
Q1=0.5 %Devalue of SiO2. You may chose any value you want between [0,1]
Q2=0.6 %Devalue of Al2O3. You may chose any value you want between [0,1]
R_SiO2=(NormMinette(1)-(X_ol/100)*NormOlivine(1)-
(X_opx/100)*NormOrthopyroxene(1)-(X_liq/100)*NormExpMelt(1))*Q1; %This is the
residual for SiO2 with less emphasis
R_TiO2=(NormMinette(2)-(X_ol/100)*NormOlivine(2)-
(X_opx/100)*NormOrthopyroxene(2)-(X_liq/100)*NormExpMelt(2)); %This is the
residual for TiO2
R_Al2O3=(NormMinette(3)-(X_ol/100)*NormOlivine(3)-
(X_opx/100)*NormOrthopyroxene(3)-(X_liq/100)*NormExpMelt(3))*Q2; %This is the
residual for Al2O3 with less emphasis
R_MnO=(NormMinette(4)-(X_ol/100)*NormOlivine(4)-
(X_opx/100)*NormOrthopyroxene(4)-(X_liq/100)*NormExpMelt(4)); %This is the
residual for MnO
R_MgO=(NormMinette(5)-(X_ol/100)*NormOlivine(5)-
(X_opx/100)*NormOrthopyroxene(5)-(X_liq/100)*NormExpMelt(5)); %This is the
residual for MgO
R_CaO=(NormMinette(6)-(X_ol/100)*NormOlivine(6)-
(X_opx/100)*NormOrthopyroxene(6)-(X_liq/100)*NormExpMelt(6)); %This is the
residual for CaO
R_Na2O=(NormMinette(7)-(X_ol/100)*NormOlivine(7)-
(X_opx/100)*NormOrthopyroxene(7)-(X_liq/100)*NormExpMelt(7));%This is the
residual for Na2O
```

```
R_K2O=(NormMinette(8)-(X_ol/100)*NormOlivine(8)-
(X_opx/100)*NormOrthopyroxene(8)-(X_liq/100)*NormExpMelt(8)); %This is the
residual for K2O
R_P2O5=(NormMinette(9)-(X_ol/100)*NormOlivine(9)-
(X_opx/100)*NormOrthopyroxene(9)-(X_liq/100)*NormExpMelt(9)); %This is the
residual for P2O5
R2=(R_SiO2)^2+(R_TiO2)^2+(R_Al2O3)^2+(R_MnO)^2+(R_MgO)^2+(R_CaO)^2+(R_Na2O)^2
+(R_K2O)^2+(R_P2O5)^2; %The sum of residual squares. The closer to zero this
value is, the better the fit.
```

R2 =

0.4550

Table A3: Input data for SPF48X

	DAT4-5	48X_melt	48X_ol	48X_cpx	48X_phl	Quality
SiO2	47.6700	42.41	40.008	54.22375	39.6400	99
TiO2	0.7200	1.41	0	0.222	2.3205	99
Al2O3	5.4800	12.35	0	0.8455	14.7072	99
FeO*	5.8500	5.90	13.148	4.47875	4.5728	90
MnO	0.1000	0.10	0.1881	0.119	0.0366	99
MgO	19.3600	6.86	45.963	16.52625	21.9672	99
CaO	14.0900	6.77	0.4622	22.8925	0.3559	99
Na2O	0.3400	0.76	0	0.3395	0.0780	99
K2O	3.7400	9.13	0	0.12575	9.6672	99
P2O5	0.4000	0.70	0	0	0.0473	99
H2O	2.4100	12.45	0	0	3.5000	99
F	0.2700	1.12	0	0	1.4547	99
Cl	0.0015	0.05	0	0	0.0173	99

```
%This is a sample calculation for how to calculate modes, estimate the
percentage of iron loss, and assessing the general quality of the fit using a
MATLAB algorithm (data used is for SPF48X). FeO* remains in the calculations
in this algorithm.
clear all;
SPF48Xdata=xlsread('SPF48X_Modes.xls'); %Load the data from the excel
spreadsheet
Xenolith=SPF48Xdata(:,1); %Denotes DAT4-5 xenolith data in the form of a
vector
Melt=SPF48Xdata(:,2); %Denotes the experimental melt data in the form of a
vector
Olivine=SPF48Xdata(:,3); %Denotes the olivine data in the form of a vector
Clinopyroxene=SPF48Xdata(:,4); %Denotes the clinopyroxene data in the form of
a vector
Phlogopite=SPF48Xdata(:,5); %Denotes the phlogopite data in the form of a
vector
Quality=SPF48Xdata(:,6); %Arbitrary quality control where everything is 99
except for FeO* which is denoted as 90
%We must construct our matrix. We will create the M matrix, which will
%contain the normalized compositions for all the phases present in our
M(:,1)=Melt; %Denotes the first column as the experimental melt composition
M(:,2)=Olivine; %Denotes the second column as the olivine composition
```

```
M(:,3)=Clinopyroxene; %Denotes the third column as the clinopyroxene
composition
M(:,4)=Phlogopite; %Denotes the fourth column as the phlogopite composition
%Recall that the xenolith is what we will compare this matrix to.
%Now we must find the values of our modes. We do this by using the method of
%projections.
X=inv(M'*M)*M'*Xenolith;
%However, we must normalize the modal abundances so that they add up to
%100%.
XX=sum(X); % This is what the sum of the modal abundances just calculated add
up to.
Xnorm=100/XX*X; %This is the normalized modal abundances for olivine,
orthopyroxene and liquid that now add up to 100%.
%We can also use this program to estimate the percentage of iron loss;
FeO=find(Quality==90); %This seeks out only FeO*
Xenolith_FeO=Xenolith(FeO); %The FeO* content for the xenolith DAT4-5
Melt_FeO=Melt(FeO); %The FeO* content for the experimental melt
Olivine_FeO=Olivine(FeO); %The FeO* content for olivine
Clinopyroxene_FeO=Clinopyroxene(FeO); %The FeO* content for clinopyroxene
Phlogopite_FeO=Phlogopite(FeO); %The FeO* content for phlogopite
X_melt=Xnorm(1); %The modal abundance for experimental melt
X_olivine=Xnorm(2); %The modal abundance for olivine
X_clinopyroxene=Xnorm(3); %The modal abundance for clinopyroxene
X_phlogopite=Xnorm(4); %The modal abundance for phlogopite
Fe_Loss=((Xenolith_FeO-(X_melt/100)*Melt_FeO-(X_olivine/100)*Olivine_FeO-
(X_clinopyroxene/100)*Clinopyroxene_FeO-
(X_phlogopite/100)*Phlogopite_FeO)/Xenolith_FeO)*100; %The estimated
percentage of iron loss
%We can also assess the quality of the fit by assessing the sum of residual
%squares. Note that I have chosen to put less emphasis on SiO2 and Al2O3
%because these are the two oxides that are the hardest to fit. I have
%chosen values of 0.5 and 0.6 arbitrarily, but you may choose any value you
%see fit
Q1=0.5; %Devalue of SiO2. You may chose any value you want between [0,1]
Q2=0.6; %Devalue of Al2O3. You may chose any value you want between [0,1]
R_SiO2=(Xenolith(1)-(X_melt/100)*Melt(1)-(X_olivine/100)*Olivine(1)-
(X_clinopyroxene/100)*Clinopyroxene(1)-(X_phlogopite/100)*Phlogopite(1))*Q1;
%This is the residual for SiO2 with less emphasis
R_TiO2=(Xenolith(2)-(X_melt/100)*Melt(2)-(X_olivine/100)*Olivine(2)-
(X_clinopyroxene/100)*Clinopyroxene(2)-(X_phlogopite/100)*Phlogopite(2));
%This is the residual for TiO2
R_Al2O3=(Xenolith(3)-(X_melt/100)*Melt(3)-(X_olivine/100)*Olivine(3)-
(X_clinopyroxene/100)*Clinopyroxene(3)-(X_phlogopite/100)*Phlogopite(3))*Q2;
%This is the residual for Al2O3 with less emphasis
R_MnO=(Xenolith(4)-(X_melt/100)*Melt(4)-(X_olivine/100)*Olivine(4)-
(X_clinopyroxene/100)*Clinopyroxene(4)-(X_phlogopite/100)*Phlogopite(4));
%This is the residual for MnO
R_MgO=(Xenolith(5)-(X_melt/100)*Melt(5)-(X_olivine/100)*Olivine(5)-
(X_clinopyroxene/100)*Clinopyroxene(5)-(X_phlogopite/100)*Phlogopite(5));
%This is the residual for MgO
R_CaO=(Xenolith(6)-(X_melt/100)*Melt(6)-(X_olivine/100)*Olivine(6)-
(X_clinopyroxene/100)*Clinopyroxene(6)-(X_phlogopite/100)*Phlogopite(6));
%This is the residual for CaO
R_Na2O=(Xenolith(7)-(X_melt/100)*Melt(7)-(X_olivine/100)*Olivine(7)-
(X_clinopyroxene/100)*Clinopyroxene(7)-
(X_phlogopite/100)*Phlogopite(7));%This is the residual for Na2O
```

```
R_K2O=(Xenolith(8)-(X_melt/100)*Melt(8)-(X_olivine/100)*Olivine(8)-
(X_clinopyroxene/100)*Clinopyroxene(8)-(X_phlogopite/100)*Phlogopite(8));
%This is the residual for K2O
R_P2O5=(Xenolith(9)-(X_melt/100)*Melt(9)-(X_olivine/100)*Olivine(9)-
(X_clinopyroxene/100)*Clinopyroxene(9)-(X_phlogopite/100)*Phlogopite(9));
%This is the residual for P2O5
R_H2O=(Xenolith(10)-(X_melt/100)*Melt(10)-(X_olivine/100)*Olivine(10)-
(X_clinopyroxene/100)*Clinopyroxene(10)-(X_phlogopite/100)*Phlogopite(10));
%This is the residual for H2O
R_F=(Xenolith(11)-(X_melt/100)*Melt(11)-(X_olivine/100)*Olivine(11)-
(X_clinopyroxene/100)*Clinopyroxene(11)-(X_phlogopite/100)*Phlogopite(11));
%This is the residual for F
R_Cl=(Xenolith(12)-(X_melt/100)*Melt(12)-(X_olivine/100)*Olivine(12)-
(X_clinopyroxene/100)*Clinopyroxene(12)-
(X_phlogopite/100)*Phlogopite(12));%This is the residual for Cl
R2=(R_SiO2)^2+(R_TiO2)^2+(R_Al2O3)^2+(R_MnO)^2+(R_MgO)^2+(R_CaO)^2+(R_Na2O)^2
+(R_K2O)^2+(R_P2O5)^2+(R_H2O)^2+(R_F)^2+(R_Cl)^2; %The sum of residual
squares. The closer to zero this value is, the better the fit.
```

Appendix B: Additional Iron Loss Data:

To check for iron loss in our experiments we also analyzed the platinum capsule. Standards for both platinum metal and iron metal were used. The accelerating potential was 15 kV, with a current of 20 nA; the beam diameter was <1 μm. Line analyses were taken perpendicular to the Pt capsule at locations likely to experience iron loss. Totals <97 are attributed to analysing part of the graphite capsule. The data acquired from the electron microprobe were corrected using the PRZ program provided by JEOL.

Table B1: Line analyses along the bottom of the Pt capsule for SPF87XX

Line	Pt	Fe	Total
1	41.6	0.407	42.007
2	55.95	0.84	56.79
3	35.09	0.371	35.461
4	36.99	0.206	37.196
5	65.06	0.567	65.627
6	0.08	0	0.08
7	7.34	0.041	7.381
8	60.44	0.297	60.737
9	96.59	0.402	96.992
10	94.13	0.403	94.533
11	97.79	0.328	98.118
12	96.78	0.369	97.149
13	97.06	0.332	97.392
14	97.91	0.321	98.231
15	97.97	0.339	98.309
16	97.71	0.286	97.996
17	98.09	0.288	98.378
18	98.26	0.269	98.53
19	97.39	0.302	97.692
20	98.39	0.235	98.625
21	98.3	0.241	98.541
22	98.69	0.206	98.896
23	99.13	0.202	99.332
24	96.74	0.232	96.972
25	97.83	0.181	98.011
26	98.65	0.177	98.828
27	97.81	0.172	97.982
28	98.27	0.139	98.409
29	97.81	0.164	97.974
30	97.44	0.178	97.618
31	97.57	0.126	97.696

32	98.03	0.118	98.148
33	98.06	0.134	98.194
34	96.39	0.117	96.507
35	97.2	0.087	97.287
36	97.84	0.097	97.937
37	97.96	0.084	98.044
38	97.98	0.105	98.085
39	98.12	0.092	98.212
40	98.56	0.045	98.605
41	98.87	0.078	98.948
42	99.25	0.049	99.299
43	98.89	0.069	98.959
44	98.97	0.07	99.04
45	98.12	0.04	98.16
46	98.47	0.063	98.533
47	98.21	0.059	98.269
48	98.56	0.059	98.619
49	97.73	0.039	97.769
50	98.96	0.024	98.984
51	98.35	0.084	98.434
52	99.22	0.052	99.272
53	98.98	0.049	99.029
54	97.83	0.037	97.867
55	99.01	0.054	99.064
56	97.75	0.06	97.81
57	99.12	0.037	99.157
58	98.04	0.023	98.063
59	98.31	0.047	98.358
60	98.4	0.005	98.405
61	98.44	0	98.44
62	98.64	0	98.64
63	98.39	0.024	98.414
64	98.17	0.04	98.21
65	98	0.018	98.018
66	98.5	0.015	98.515
67	97.79	0.014	97.804
68	99.47	0.035	99.505
69	98.96	0	98.96
70	98	0	98
71	97.57	0.034	97.604
72	97.62	0.014	97.634
73	98.87	0	98.87
74	99.98	0.005	99.985
75	98.73	0	98.73
76	99.98	0.021	100.001
77	98.53	0.026	98.556
78	96.9	0	96.9
79	98.35	0.016	98.366
80	99.62	0	99.62
81	99.5	0	99.5
82	98.42	0	98.42
83	97.88	0	97.88
84	97.9	0	97.9

85	99.15	0.017	99.167
86	98.8	0.033	98.833
87	98.78	0.006	98.786
88	98.8	0	98.8

Table B2: Line analyses along the top of the Pt capsule for SPF87XX

Line	Pt	Fe	Total
1	64.47	0.61	65.08
2	78.28	0.823	79.103
3	9.34	0.083	9.423
4	5.19	0.032	5.223
5	0.404	0	0.404
6	8.34	0.051	8.391
7	87.85	1	88.85
8	98.42	1.08	99.5
9	98.33	1.07	99.4
10	98	1.05	99.05
11	98.3	1.02	99.32
12	97.61	1.03	98.64
13	97.5	1.01	98.51
14	97.05	0.966	98.016
15	98.31	0.891	99.201
16	97.49	0.923	98.413
17	98.11	0.875	98.985
18	97.82	0.846	98.666
19	97.56	0.827	98.387
20	96.51	0.85	97.36
21	97.82	0.798	98.618
22	97.32	0.742	98.062
23	97.61	0.682	98.292
24	95.9	0.71	96.61
25	98.34	0.709	99.049
26	97.4	0.622	98.022
27	93.95	0.703	94.653
28	98.38	0.639	99.019
29	98.45	0.653	99.103
30	99.16	0.598	99.758
31	98.91	0.571	99.481
32	98.6	0.572	99.172
33	98.07	0.529	98.599
34	98.25	0.52	98.77
35	97.92	0.519	98.439
36	97.01	0.521	97.531
37	98.89	0.523	99.413

Table B3: Line analyses along the top of the Pt capsule for SPF53X

Line	Pt	Fe	Total
1	96.02	3.42	99.44
2	86.82	2.92	89.74
3	14.06	0.503	14.563
4	0	0.009	0.009
5	0	0.014	0.014

6	0.05	0.007	0.057
7	0.095	0	0.095
8	41.58	0.797	42.377
9	98.35	0.887	99.238
10	99.1	0.815	99.915
11	99.8	0.747	100.547
12	99.38	0.666	100.046
13	99	0.622	99.622
14	100.52	0.592	101.112
15	100.84	0.466	101.306
16	100.49	0.439	100.929
17	100.94	0.396	101.336
18	100.65	0.4	101.05
19	101.75	0.311	102.061
20	100.74	0.252	100.992
21	100.57	0.246	100.816
22	101.37	0.217	101.587
23	101.52	0.201	101.721
24	101.43	0.139	101.569
25	101.15	0.174	101.323
26	101.07	0.15	101.22
27	100.87	0.093	100.963
28	99.85	0.054	99.904
29	99.4	0.022	99.422
30	100.9	0.066	100.966
31	102.29	0.059	102.349
32	101.11	0.034	101.144
33	101.37	0.029	101.399
34	100.5	0.011	100.511
35	99.58	0	99.58
36	99.78	0	99.78
37	101.61	0.03	101.64
38	101.16	0	101.16
39	99.54	0.028	99.568
40	100.44	0.016	100.456
41	99.71	0.009	99.719
42	100.7	0	100.7
43	100.04	0.04	100.08
44	100.41	0.044	100.454
45	100.66	0.007	100.667
46	100.38	0.015	100.395
47	98.5	0	98.5
48	103.46	0	103.46
49	102.72	0	102.72
50	101.13	0.006	101.136
51	67.95	0	67.95
52	3.91	0	3.91
53	102.54	0	102.54
54	100.86	0	100.86
55	100.92	0.03	100.95
56	100.36	0	100.36
57	101.47	0	101.47
58	101.89	0	101.89

59	101.34	0	101.34
60	101.63	0	101.63
61	96.25	0.016	96.266
62	99.67	0.008	99.678
63	100.92	0	100.92
64	100.62	0	100.62
65	101.01	0	101.01
66	101.22	0.015	101.235
67	101.81	0.025	101.835
68	100.78	0	100.78

Table B4: Line analyses along the bottom of the Pt capsule for SPF50X

Line	Pt	Fe	Total
1	81.93	3.9	85.83
2	92.69	4.23	96.92
3	92.14	3.84	95.98
4	88.44	3.28	91.72
5	18.22	0.54	18.76
6	10.05	0.308	10.358
7	96.13	2.63	98.76
8	96.67	2.31	98.98
9	96.35	2.18	98.53
10	96.69	1.97	98.66
11	96.87	1.91	98.78
12	98.18	1.67	99.85
13	96.91	1.62	98.53
14	96.56	1.53	98.09
15	98.19	1.41	99.6
16	98.01	1.28	99.29
17	97.22	1.24	98.46
18	96.46	1.15	97.61
19	95.49	1.06	96.55
20	90.24	0.975	91.215
21	80.23	0.903	81.133
22	65.11	0.817	65.928
23	47.58	0.829	48.409
24	98.21	0.723	98.933
25	98.09	0.623	98.713
26	99.45	0.627	100.077
27	99.92	0.57	100.49
28	99.84	0.536	100.376
29	100.69	0.449	101.138
30	100.41	0.381	100.791
31	100.65	0.431	101.081
32	101.19	0.34	101.53
33	99.93	0.376	100.306
34	100.12	0.361	100.481
35	99.13	0.248	99.378
36	98.72	0.235	98.955
37	98.68	0.239	98.919
38	98.87	0.199	99.069
39	101.3	0.198	101.498

40	100.84	0.159	100.998
41	100.69	0.153	100.843
42	101.57	0.128	101.698
43	101.06	0.104	101.164
44	100.92	0.091	101.011
45	100.94	0.092	101.032
46	100.32	0.071	100.391
47	102.15	0.049	102.198
48	102.27	0.101	102.371
49	102.55	0.076	102.626
50	102.08	0.06	102.14
51	102.15	0.076	102.226
52	102.53	0.058	102.588
53	101.9	0.031	101.931
54	102.5	0.053	102.553
55	102.13	0	102.13
56	95.65	0.012	95.662
57	99.86	0.012	99.872
58	101.05	0.028	101.078
59	101.32	0	101.32
60	100.4	0.02	100.42
61	102.65	0	102.65
62	101.57	0.022	101.591
63	100.26	0.023	100.283
64	101.99	0	101.99
65	101.06	0.013	101.072
66	100.56	0.025	100.585
67	100.84	0.014	100.854
68	99.41	0.045	99.455
69	100.02	0.03	100.05
70	99.52	0	99.52
71	100.08	0	100.08
72	102.43	0	102.43
73	101.58	0	101.58
74	101.92	0.006	101.926

Table B5: Line analyses along the top of the Pt capsule for SPF49X

Line	Pt	Fe	Total
1	95.63	2.62	98.25
2	97.45	2.37	99.82
3	99.76	2.06	101.82
4	98.15	2.04	100.19
5	98.54	1.8	100.34
6	91.61	1.69	93.3
7	89.96	1.52	91.48
8	101.25	1.37	102.62
9	99.73	1.28	101.01
10	95.64	1.07	96.71
11	84.44	1	85.44
12	96.03	0.836	96.866
13	100.16	0.814	100.974
14	97.33	0.66	97.99

15	96.62	0.645	97.265
16	100.49	0.502	100.992
17	102.58	0.43	103.01
18	100.2	0.433	100.632
19	99.89	0.382	100.272
20	94.56	0.335	94.895
21	101.54	0.26	101.8
22	100.06	0.195	100.255
23	99.2	0.581	99.781
24	100.68	0.211	100.891
25	102.14	0.097	102.237
26	100.1	0.128	100.228
27	98.54	0.14	98.68
28	98.99	0.12	99.11
29	100.55	0.073	100.623
30	101.1	0.09	101.19
31	97.91	0.038	97.948
32	101.03	0.02	101.05
33	101.29	0.055	101.345
34	78.99	0.026	79.016
35	3.71	0.007	3.718
36	0.087	0	0.087
37	0.126	0.005	0.131
38	0.126	0	0.126
39	0.157	0	0.157
40	0	0	0
41	0	0	0
42	0.189	0.007	0.196
43	12.52	0.026	12.546
44	40.67	0	40.67
45	98.56	0.014	98.574
46	101.2	0	101.2
47	100.94	0.013	100.953
48	96.96	0	96.96
49	96.09	0	96.09
50	99.51	0	99.51
51	98.01	0.019	98.029

Table B6: Line analyses along the bottom of the Pt capsule for SPF65X

Line	Pt	Fe	Total	Comments
1	98.13	2.45	100.58	Line 1 SPF65X_bottom_capsule
2	98.59	2.2	100.79	Line 2 SPF65X_bottom_capsule
3	98.65	2.13	100.78	Line 3 SPF65X_bottom_capsule
4	98.74	1.9	100.64	Line 4 SPF65X_bottom_capsule
5	97.95	1.69	99.64	Line 5 SPF65X_bottom_capsule
6	100.07	1.58	101.65	Line 6 SPF65X_bottom_capsule
7	98.96	1.44	100.4	Line 7 SPF65X_bottom_capsule
8	99.02	1.34	100.36	Line 8 SPF65X_bottom_capsule
9	100.08	1.22	101.3	Line 9 SPF65X_bottom_capsule
10	100.45	1.14	101.59	Line 10 SPF65X_bottom_capsule
11	99.97	1.03	101	Line 11 SPF65X_bottom_capsule
12	100.19	0.909	101.099	Line 12 SPF65X_bottom_capsule

13	100.01	0.842	100.852	Line 13 SPF65X_bottom_capsule
14	100.38	0.755	101.135	Line 14 SPF65X_bottom_capsule
15	100.43	0.772	101.202	Line 15 SPF65X_bottom_capsule
16	100.73	0.681	101.411	Line 16 SPF65X_bottom_capsule
17	101.3	0.625	101.925	Line 17 SPF65X_bottom_capsule
18	100.62	0.577	101.197	Line 18 SPF65X_bottom_capsule
19	101.36	0.543	101.902	Line 19 SPF65X_bottom_capsule
20	100.8	0.437	101.237	Line 20 SPF65X_bottom_capsule
21	101.81	0.391	102.201	Line 21 SPF65X_bottom_capsule
22	102	0.403	102.403	Line 22 SPF65X_bottom_capsule
23	101.14	0.396	101.536	Line 23 SPF65X_bottom_capsule
24	101.43	0.307	101.737	Line 24 SPF65X_bottom_capsule
25	102.04	0.322	102.362	Line 25 SPF65X_bottom_capsule
26	100.45	0.268	100.718	Line 26 SPF65X_bottom_capsule
27	100.38	0.201	100.581	Line 27 SPF65X_bottom_capsule
28	101.67	0.178	101.848	Line 28 SPF65X_bottom_capsule
29	101.22	0.176	101.396	Line 29 SPF65X_bottom_capsule
30	102.73	0.177	102.907	Line 30 SPF65X_bottom_capsule
31	101.94	0.169	102.109	Line 31 SPF65X_bottom_capsule
32	100.94	0.141	101.081	Line 32 SPF65X_bottom_capsule
33	101.63	0.127	101.757	Line 33 SPF65X_bottom_capsule
34	102.78	0.105	102.885	Line 34 SPF65X_bottom_capsule
35	101.34	0.057	101.397	Line 35 SPF65X_bottom_capsule
36	101.8	0.121	101.921	Line 36 SPF65X_bottom_capsule
37	98.71	0.086	98.796	Line 37 SPF65X_bottom_capsule
38	99.35	0.072	99.422	Line 38 SPF65X_bottom_capsule
39	100.62	0.029	100.649	Line 39 SPF65X_bottom_capsule
40	100.91	0.059	100.969	Line 40 SPF65X_bottom_capsule
41	100.6	0.054	100.654	Line 41 SPF65X_bottom_capsule
42	100.51	0.036	100.545	Line 42 SPF65X_bottom_capsule
43	100.64	0.013	100.653	Line 43 SPF65X_bottom_capsule
44	101.21	0.041	101.251	Line 44 SPF65X_bottom_capsule
45	101.5	0.023	101.523	Line 45 SPF65X_bottom_capsule
46	100.94	0.034	100.974	Line 46 SPF65X_bottom_capsule
47	101.07	0.053	101.123	Line 47 SPF65X_bottom_capsule
48	101.32	0.04	101.36	Line 48 SPF65X_bottom_capsule
49	101.05	0.031	101.081	Line 49 SPF65X_bottom_capsule
50	100.8	0.031	100.831	Line 50 SPF65X_bottom_capsule
51	100.74	0	100.74	Line 51 SPF65X_bottom_capsule

Appendix C: Alkali Migration:

Alkali migration is the physical diffusion of alkali elements (typically sodium and potassium) in a hydrous glass away from the electron beam because of heating (Vassamillet and Caldwell 1969). This phenomena has been a previously studied (Varshyneya et al. 1966; Borom and Hanneman 1967; Goodhews and Gulley 1974; Goodhews 1975; Jercinovic and Keil 1988; Nielsen et al. 1995; Spray and Rae 1995; Morgan and London 1996, 2005; Borisov 2009) and is known to affect the resultant signal of Na or K to the spectrometers. Resultant X-ray signals from other elements, notably Si, Al, and possibly Ca, artificially increase (Morgan and London 2005). Vassamillet and Caldwell (1969) noted that the rate of alkali migration under the electron beam increases with decreasing accelerating voltage, at a constant beam current, because the excitation volume decreases with decreasing accelerating voltages. Therefore, the resulting thermal energy per unit volume is greater at lower accelerating voltages, leading to faster alkali migration.

Morgan and London (2005) performed a detailed analysis on a hydrous and anhydrous haplogranitic glass, and systematically detailed the effect of beam diameter, beam current, and the resultant beam current density (in units of nA μm^{-2}) on sodium migration. All analyses performed in their study were with a 20 kV accelerating voltage, using beam currents varying from 2 - 50 nA, and fixed beam diameters ranging from 2 - 20 μm. Morgan and London (2005) found that for current densities <0.006 nA μm^{-2}, there is very little (<2.7% relative) loss of sodium signal. In general, sodium loss increases with increasing current densities. With a current density up to 0.1 nA μm^{-2}, minor (7 - 9% relative) sodium loss is observed, while becoming severe at current densities >0.5 nA μm^{-2} (Morgan and London 2005). They also found that

sodium loss is far more pronounced in hydrous glasses relative to anhydrous glasses (Morgan and London 2005).

Borisov (2009) also performed a systematic study on alkali loss, this time including Rb and K with Na, as a function of beam diameter on the electron microprobe. He noted that the effects were dramatic when the beam diameter was <1μm, and less so as beam diameter increased, consistent with Morgan and London's findings. At 20 μm, the alkali signal was nearly constant, indicating that the alkali elements were stable.

Morgan and London (1996) suggested that in complex multi-component systems, use two separate beam conditions and an accelerating voltage of 20 kV, in order to properly analyse hydrous glasses; first: a beam current of 2 nA and a beam diameter of 20 μm be used to analyse alkalis and aluminosilicate components, and; second: a 20 nA and 20 μm beam for all other components. These conditions should reduce the effect of alkali migration induced by heating from the beam, and minimize gains in Si and Al, while providing consistent measurements for all other components. However, these conditions were unusable in our analyses because we have both solid phases and melt. Instead, we used a beam diameter of 10 μm, and a current of 10 nA, with an accelerating voltage of 15 kV. This was chosen in order to help mitigate alkali loss in the hydrous glasses, as well as to keep the oxidation volume of my analysis roughly the same as the mineral analyses.

Time-dependant analyses were performed on our hydrous glasses in order to quantify the relative proportion of alkali loss due to heating from the incident beam. Eighty to one hundred analyses were performed on a single spot on the glass. An accelerating voltage of 15 kV, with a current of 10 nA, and a beam diameter of 10 μm, was used (current density: ~0.12 nA μm^{-2}).

Because we counted only the peak and not the background, the absolute counts are useful only to monitor changes with time. **Figure C1** shows the percentage of K_2O loss with respect to temperature, while **Figure C2** shows this effect with respect to pressure. The extent of potassium migration, at constant pressure, in these glasses decreases with increasing temperature of the experiment (**Figure C1**), similar to the findings of Morgan and London (2005). The extant of isothermal potassium migration increases with increasing pressure (**Figure C2**). We conclude that both trends reflect the relative proportions of water in the melt. In experiments with relatively low fractions of partial melt (~37%), there seems to be a "grace period" lasting ~20-30 seconds, where the signal of potassium appears nearly constant (1200°C and 1250°C at 1.33 GPa, **Figure C1**; 1300°C and 2.21 GPa, **Figure C2**), after which, heat from the beam decreases the resultant potassium signal (i.e. increases the % K_2O loss). This is consistent with the findings of Vassamillet and Caldwell (1969), who argued that a critical temperature exists, after which alkali migration proceeds. This was also seen in Morgan and London (1996) and Borisov (2009).

We found it difficult to properly assess the extent of Na loss in our glasses. This is likely due to the low concentrations of Na_2O in the glass, relative to K_2O, and the short spot-time during our time-dependant analyses. In general, we found that Na loss does increase with increasing time (**Figure C3**), consistent with the studies of Hanson et al. (1996) and Borisov (2009), but the scatter in the data is larger than what was observed in the K loss.

If alkali migration did occur, it would be more prominent in experiments with low melt fractions. However, because K and Na (along with Si and Al) were analysed first, and the time of each analysis takes place during the "grace period", we argue that alkali migration was not a significant factor that affected the concentrations of these elements.

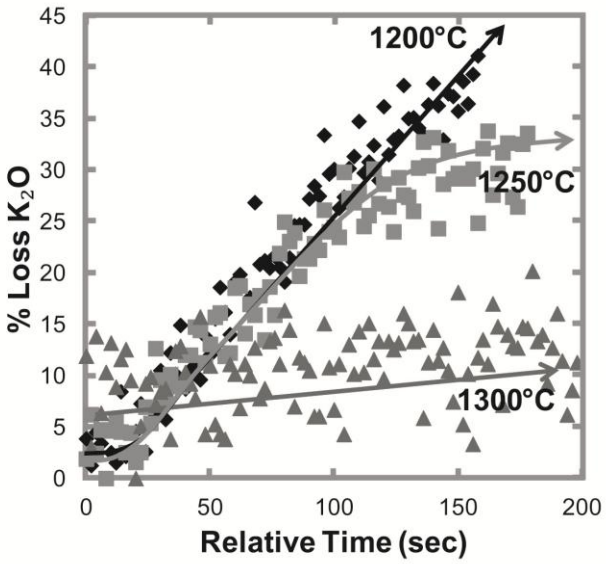

Figure C1: % Loss of K_2O versus time of analysis at constant pressure (1.33 GPa). Curves with arrows show approximate trends. Symbols: black diamond = 1200°C; grey square = 1250°C; grey triangle = 1300°C.

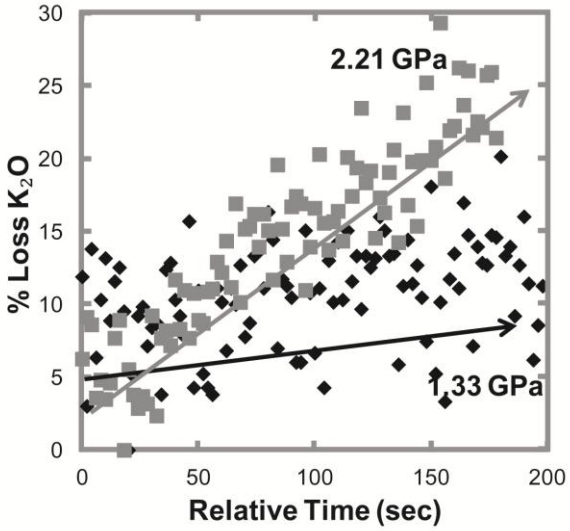

Figure C2: % Loss of K_2O versus time of analysis at constant temperature (1300°C). Curves with arrows show approximate trends. Symbols: black diamond = 1.33 GPa; grey square = 2.21 GPa.

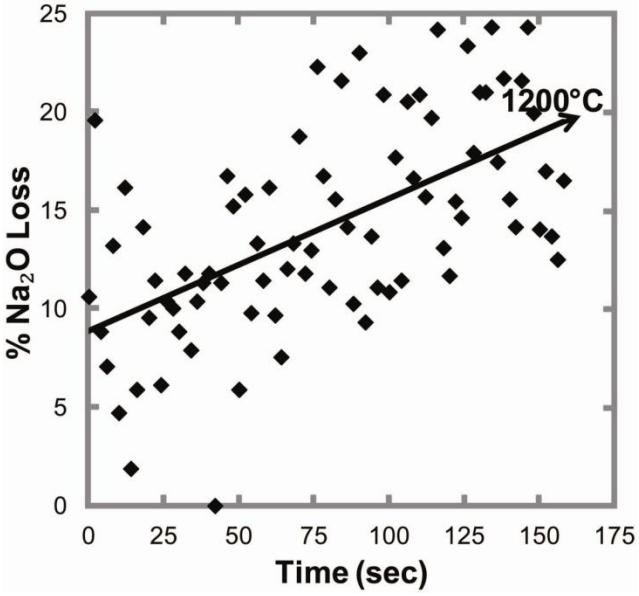

Figure C3: % Loss of Na_2O versus time of analyses at 1.33 GPa and 1200°C. The black arrow indicates the trend of the sodium loss.

References:

Boriso AA (2009) Influence of SiO_2 and Al_2O_3 on the activity coefficients of alkalis in melts: An experimental study. Petrology **17:** 623 - 635

Borom MP, Hanneman RE (1967) Local compositional changes in alkali silicate glasses during electron microprobe analysis. Journal of Applied Physics **38:** 2406 - 2408

Goodhew, P.J. (1975). Electron probe microanalysis of glass containing alkali metals. Microstructural Science, **3:** 631 - 641.

Goodhew, P.J. & Gulley, J.E.C. (1974). The determination of alkali metals in glass by electron microprobe analysis. Glass Technology, **15:** 123 - 126.

Jercinovic, M.J. & Keil, K. (1988). Electron microprobe analysis of basaltic glasses and associated alteration products. *In* D.E. Newberry Ed., Microbeam Analysis, pg. 495 - 497. San Francisco Press, California.

Morgan, G.B. & London, D. (1996). Optimizing the electron microprobe analysis of hydrous alkali aluminosilicate glasses. American Mineralogist, **81:** 1176 - 1185.

Morgan, G.B. & London, D. (2005). Effect of current density on the electron microprobe analysis of alkali aluminosilicate glasses. American Mineralogist, **90:** 1131 - 1138.

Nielsen, R.L., Christie, D.M., & Spretel, F.M. (1995). Anomalously low sodium in MORB magmas: evidence for depleted MORB or analytical artifact? Geochimica et Cosmochimica Acta, **59:** 5023 - 5026.

Spray, J.G. & Rae, D.A. (1995). Quantitative electron-microprobe analysis of alkali silicate glasses: A review and user guide. Canadian Mineralogist, **33:** 323 - 332.

Varshneya, A.K., Cooper, A.R., & Cable, M. (1966). Changes in composition during electron microprobe analysis of K_2O-SrO-SiO_2 glass. Journal of Applied Physics, **37:** 2199 - 2202.

Vassamillet, L.F. & Caldwell, V.E. (1969). Electron-probe microanalysis of alkali metals in glasses. Journal of Applied Physics, **40:** 1637 - 1640.

Appendix D: Substitution mechanisms in phlogopite

Determining the substitution mechanism of Ti in phlogopite was more involved. Two possible substitution mechanisms for Ti in phlogopite have been proposed, one by Forbes and Flower (1974; reaction 4), and the other by Robert (1976; reaction 5):

$$2Mg^{[VI]} \leftrightarrow Ti^{[VI]}\square^{[VI]} \quad (4)$$

$$Mg^{[VI]}2Si^{[IV]} \leftrightarrow Ti^{[VI]}2Al^{[IV]} \quad (5)$$

where $Mg^{[VI]}$, $Ti^{[VI]}$ and $\square^{[VI]}$ represents magnesium, titanium and vacancy on the octahedral sites, respectively, and $Si^{[IV]}$ and $Al^{[IV]}$ represent silicon and aluminum in the tetrahedral sites, respectively. Using the graphical methodology outlined in Arima and Edgar (1981), both substitution mechanisms occur in the phlogopite in these experiments (**Figure D1**). This conclusion is supported by the cation totals in the octahedral sites <6 (**Table 3.6**), interpreted as vacancies, and Al in the tetrahedral sites >2 (**Table 3.6**), consistent with reaction 5.

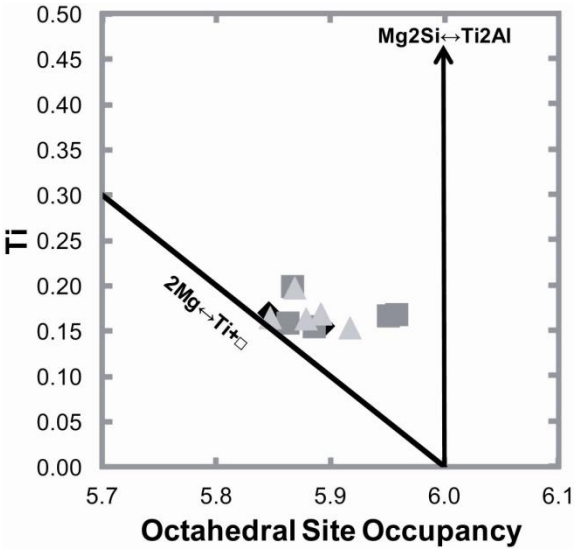

Figure D1: Ti in phlogopite vs. Octahedral site occupancy. The black lines indicate the substitution reactions. Symbols: black diamond = 1.33 GPa, dark grey squares = 1.77 GPa, light grey triangles = 2.21 GPa.

References:

Arima M, Edgar AD (1981) Substitution mechanisms and solubility of titanium in phlogopites from rocks of probable mantle origin. Contrib Mineral Petrol **77:** 288 - 295

Forbes WC, Flower MFJ (1974) Phase relations of titan-phlogopite, $K_2Mg_4TiAl_2Si_6O_{20}(OH)_2$: a refractory phase in the upper mantle? Earth Planet Sci Lettt **22:** 60 - 66

Robert JL (1976) Titanium solubility in synthetic phlogopite solid solutions. Chem Geol **17:** 213 - 227

Appendix E: Unused or extra compositional data:

Note: All pressures reported in this section are nominal pressures (before -13% correction was applied)

Table E1: Composition of other experiments using the minette RAB90 Au24-1.

Sample SPF-	**1**	**1**	**1**	**1**	**1**	**27**	**14**	**14**	**14**	**19**	**19**
Phase	ap	phl	cpx	ol	melt	melt	melt	opx	cpx	melt	opx
P (GPa)	1.5	1.5	1.5	1.5	1.5	2.0	2.5	2.5	2.5	2.5	2.5
T (°C)	1200	1200	1200	1200	1200	1400	1300	1300	1300	1350	1350
Time (hrs)	72	72	72	72	72	23	24	24	24	48	48
n	3	2	5	4	9	21	12	8	8	23	8
SiO_2	0.64	39.65	52.7(20)	38.5(8)	50.7(6)	48.08	44.75	56.1(10)	53.7(12)	46.5(8)	56.4(8)
TiO_2	<d.l.	4.55	0.4(2)	<d.l.	0.60(9)	1.09	1.23	0.11(4)	0.17(4)	1.21(9)	0.11(3)
Al_2O_3	0.12	16.12	2.3(10)	<d.l.	15.4(3)	9.50	11.19	2.1(3)	2.7(4)	10.6(3)	2.2(3)
FeO*	1.03	7	5.3(3)	24.6(5)	7.4(2)	6.58	8.63	7.6(1)	5.5(7)	7.4(1)	6.7(2)
MnO	0.11	<d.l.	0.14(2)	0.29(4)	0.13(4)	0.13	0.13	0.14(3)	0.14(4)	0.14(6)	0.14(4)
MgO	0.89	20.04	17.4(9)	37.1(18)	3.5(2)	14.27	10.61	31.6(10)	20.7(12)	11.1(4)	32.4(11)
CaO	52.71	<d.l.	20.3(20)	0.3(2)	4.7(3)	8.13	8.12	2.1(2)	15.3(20)	8.8(2)	2.2(2)
Na_2O	0.13	0.22	0.4(2)	<d.l.	2.9(2)	1.23	1.62	0.1(2)	0.5(3)	1.4(3)	0.11(7)
K_2O	0.14	9.99	<d.l.	<d.l.	7.1(2)	4.59	5.60	<d.l.	<d.l.	5.4(2)	<d.l.
P_2O_5	40.37	<d.l.	<d.l.	<d.l.	1.7(2)	1.14	1.27	<d.l.	<d.l.	1.3(1)	<d.l.
F	??	??	??	??	??	??	??	??	??	??	??
Cl	??	??	??	??	??	??	??	??	??	??	??
Total	96.14	97.57	98.94	100.79	94.13	94.74	93.14	99.85	98.71	93.85	100.26

Fluorine and chlorine were not analyzed

Table E2:Average melt compositions from DAT4-5 experiments with either extensive Fe loss or not at equilibrium:

Run SPF-	**64X**	**83XX**	**76X**	**85XX**	**75X**	**73X**	**82XX**	**41X**	**62X**	**84XX**	**88XX**	**89XX**
P (GPa)	1.5	1.5	1.5	2	2	2	2	2	2	2	2	2.5
T (°C)	1200	1250	1400	1225	1250	1275	1275	1300	1300	1300	1325	1400
time (hrs)	69.5	119	144	191	118	95.5	118	47	95.5	167.5	166.5	168
% Fe Loss		24.9		64.8	52.6		25.4	29.6			47.7	54.8
SiO_2	45.51	47.41	48.6(5)	47.52	45.18	44.96	45.90	45.1(14)	44.23	45.04	45.82	47.12
TiO_2	1.29	1.45	0.77(7)	1.36	1.35	1.42	1.22	1.3(1)	1.34	1.29	1.19	0.86
Al_2O_3	10.73	12.42	6.3(2)	14.13	11.08	11.49	9.90	10.5(4)	11.09	10.46	10.26	7.39
FeO*	6.26	3.71	3.1(1)	1.89	2.98	5.34	5.28	5.0(2)	4.79	4.99	3.39	2.71
MnO	0.11	0.09	0.08(4)	0.07	0.10	0.11	0.11	0.11(5)	0.12	0.11	0.09	0.08
MgO	10.44	9.50	19.4(3)	8.80	11.61	10.16	12.18	11.5(3)	11.18	11.64	12.91	17.53
CaO	11.27	9.51	12.7(7)	7.69	9.55	9.41	10.59	10.1(4)	9.97	10.02	11.17	12.70
Na_2O	0.71	0.91	0.6(4)	0.95	0.78	0.78	0.78	0.7(4)	0.73	0.88	0.62	0.46
K_2O	7.24	8.71	4.0(1)	10.26	8.23	8.48	6.80	7.5(4)	7.99	7.47	6.76	4.56
P_2O_5	0.67	0.83	0.4(1)	1.09	0.73	0.76	0.66	0.6(1)	0.75	0.73	0.60	0.45
Cr_2O_3	0.02	0.02		0.00	0.02	0.03	0.03	---	0.02	0.02	0.02	0.06
Total	94.26	94.56		93.75	91.63	92.94	93.44	92.41	92.20	92.64	92.83	93.92

Table E3: Average olivine compositions from DAT4-5 experiments with either extensive Fe loss or not at equilibrium:

Run SPF-	**64X**	**83XX**	**85XX**	**75X**	**73X**	**82XX**	**41X**	**62X**	**84XX**	**88XX**	**89XX**
P (GPa)	1.5	1.5	2	2	2	2	2	2	2	2	2.5
T (ºC)	1200	1250	1225	1250	1275	1275	1300	1300	1300	1325	1400
time (hrs)	69.5	119	191	118	95.5	118	47	95.5	167.5	166.5	168
SiO_2	40.39	41.75	41.56	42.27	41.39	41.33	41.2(12)	40.93	41.35	41.78	42.54
TiO_2	0.02	0.03	0.02	0.01	0.02	0	<d.l.	0.01	0.01	0	0.01
Al_2O_3	0.10	0.03	0.11	0.06	0.19	0.05	<d.l.	0.05	0.04	0.06	0.05
FeO*	9.18	6.3	4.18	4.62	8.43	7.14	7.2(4)	7.43	7.28	4.85	2.85
MnO	0.13	0.12	0.09	0.12	0.12	0.1	0.13(5)	0.12	0.11	0.09	0.06
MgO	49.70	51.62	53.41	53.27	48.09	50.95	49.8(7)	50.97	51.03	53.15	54.31
CaO	0.52	0.38	0.28	0.45	1.12	0.34	0.38(8)	0.35	0.33	0.34	0.4
Na_2O	0.02	0.14	0.14	0.08	0.09	0.23	<d.l.	0.02	0.03	0.04	0.01
K_2O	0.06	0.01	0.05	0.01	0.04	0	<d.l.	0.02	0.00	0	0
P_2O_5	0.04	0.05	0.12	0.04	0.04	0.04	<d.l.	0.03	0.02	0.02	0.03
Cr_2O_3	0.01	0.02	0.02	0.04	0.04	0.02	---		0.03	0.03	0.03
Total	100.16	100.46	99.98	100.95	99.57	100.19	98.71	99.93	100.24	100.37	100.28

Table E4: Average clinopyroxene compositions from DAT4-5 experiments with either extensive Fe loss or not at equilibrium:

Run SPF-	**64X**	**83XX**	**85XX**	**75X**	**73X**	**82XX**	**41X**	**62X**	**84XX**	**88XX**	**89XX**
P (GPa)	1.5	1.5	2	2	2	2	2	2	2	2	2.5
T (°C)	1200	1250	1225	1250	1275	1275	1300	1300	1300	1325	1400
time (hrs)	69.5	119	191	118	95.5	118	47	95.5	167.5	166.5	168
SiO_2	53.73	54.69	53.73	54.65	53.98	54.48	54.0(12)	54.44	54.91	54.21	54.88
TiO_2	0.24	0.31	0.47	0.23	0.23	0.19	0.2(1)	0.25	0.22	0.2	0.13
Al_2O_3	1.16	1.77	3.37	1.61	1.70	1.78	1.7(9)	1.81	1.81	1.89	1.47
FeO*	2.90	1.8	1.75	1.92	2.48	2.09	2.3(7)	2.35	2.12	1.83	1.46
MnO	0.08	0.08	0.08	0.06	0.07	0.05	0.06(5)	0.08	0.05	0.08	0.06
MgO	18.06	18.75	19.36	18.97	17.98	19.13	18.6(12)	18.79	19.06	19.71	21.2
CaO	23.01	21.85	19.87	21.95	21.95	20.49	21.1(17)	21.37	21.06	20.44	19.24
Na_2O	0.14	0.17	0.4	0.23	0.21	0.27	0.2(1)	0.18	0.25	0.19	0.19
K_2O	0.05	0.03	0.06	0.04	0.05	0.03	0.05(7)	0.06	0.02	0.04	0.03
P_2O_5	0.02	0.03	0.03	0.02	0.03	0.03	<d.l.	0.02	0.03	0.03	0.03
Cr_2O_3	0.20	0.18	0.15	0.21	0.21	0.19	---	0.18	0.21	0.2	0.19
Total	99.60	99.67	99.27	99.89	98.89	98.73	98.21	99.52	99.74	98.81	98.88